Important Notice

THE UNIVERSITY OF CALGARY

Techniques to enhance the accuracy and efficiency of finite-difference modelling for the propagation of elastic waves

by

Peter Malcolm Manning

A THESIS

SUBMITTED TO THE FACULTY OF GRADUATE STUDIES

IN PARTIAL FULFILLMENT OF THE REQUIREMENTS FOR THE DEGREE OF DOCTOR OF PHILOSOPHY

DEPARTMENT OF GEOSCIENCE

CALGARY, ALBERTA

November, 2007

THE UNIVERSITY OF CALGARY

FACULTY OF GRADUATE STUDIES

The undersigned certify that they have read, and recommend to the Faculty of Graduate Studies for acceptance, a thesis entitled "Techniques to enhance the accuracy and efficiency of finite-difference modelling for the propagation of elastic waves" submitted by Peter Malcolm Manning in partial fulfillment of the requirements for the degree of DOCTOR OF PHILOSOPHY.

Supervisor, Dr. G. J. Margrave
Department of Geoscience

Dr. Cristian Rios
Department of Mathematics and Statistics

Dr. L. R. Lines
Department of Geoscience

Dr. Phillip Bording
External examiner
Department of Earth Sciences
Memorial University St. John's

Dr. E. S. Krebes
Department of Geoscience

Date

Abstract

New techniques are described to enhance the accuracy and efficiency of finite-difference modelling for the propagation of elastic waves.

The most important technique involves the active adjustment of the frequency content of each finite modelling step. This contrasts with most current finite-difference modelling practise, which uses frequency analysis only to evaluate the utility of various other processes within a step. In order to adjust frequency content with spatial operators of limited size, procedures combining Fourier analysis and optimization are developed. This is done first for one spatial dimension, and then for two. Tests show obvious improvements by use of this technique.

A second technique develops a mathematical definition of a transmitting edge for finite-difference models, often called an absorbing boundary. Tests indicate that this is a valid concept, and show some encouraging results.

Three case studies are also included where finite-difference modelling sheds some light on elastic propagation problems. The first shows how Rayleigh (surface) waves are transmitted and reflected at simple velocity boundaries. The second shows how near surface conditions affect the character of body and surface waves. The third shows where finite-difference modelling may add to the realism of AVO interpretations.

Acknowledgements

Thanks for my original training in seismic methods are owed to Hans den Boer and Marco Meilink at Mobil Oil Canada. There the secrets of Fourier transforms, deconvolution, and many other mysteries were revealed.

Ed Krebes at the University of Calgary provided insights into 3D elasticity and other concepts from his advanced seismic courses.

Also thanks to Hugh Geiger for many helpful suggestions, and his discovery of the 'nonstandard' finite-difference schemes of Mickens and Cole.

My most important debt is to my supervisor Gary Margrave, who suggested this venture and provided all manner of support throughout its extended term. Always ready to entertain ideas no matter how different or difficult, analyze them and either support them or show their flaws, his flexibility has been an inspiration. His demands for more rigour and precedents have enhanced most of the ideas presented here. He has also been a most convenient source of Matlab wisdom.

Finally, a special thanks for the support of the CREWES group and the CREWES staff, including Henry Bland and Kevin Hall for technical support, and Pat Daley for ideas and proofreading.

Table of Contents

List of Tables

List of Figures

Chapter 1

Introduction

This thesis is concerned with the techniques of finite-difference modelling as applied to seismic waves that travel through regions with homogeneous properties. Most of the waves studied are pressure and shear waves, known as body waves, that travel inside the medium. Some work was also done on Rayleigh waves, which may travel on the surface of a model. An essential part of these studies is the way these waves interact with each other at boundaries within the models, and at the edges of the models.

The work here was stimulated by the successful models of previous authors who applied finite-difference methods in various areas, as shown in papers and presentations. A particular revelation was its use to simulate surface waves, as well as body waves. The debt owed these earlier investigators is acknowledged wherever it is known.

The object of this thesis is to introduce and apply some novel techniques and provide some new insights, so that even more of the subtle effects of seismic wave propagation may be demonstrated. These novel ideas generally arise with analysis of a problem from a slightly different viewpoint. The results are then sometimes compared with other approaches to a solution for the same known problem. In all cases, though, the novel techniques have been combined with known techniques for the final product.

1.1 Thesis organization

1. Chapter 1 gives the introduction, the content of the chapters, and the claims of novelty. It also gives a review of how frequency domain analysis is used in finite-difference modelling. This is compared with the use of frequency domain techniques in seismology, and suggests some approaches in the finite-difference world.

2. In chapter 2, frequency dependant corrections to the wave equation in one spatial dimension are investigated. The corrections are developed by comparing the operation of a continuous second derivative on a single frequency wave to the operation of the most simple finite-difference second derivative on the same wave. The beneficial effects of the corrections on dispersion, group velocity and phase are illustrated. Finally, stability is considered from the point of view of aliasing in the frequency domain.

3. Chapter 3 applies the same methods to derive finite-difference corrections for modelling in two spatial dimensions. Stability and frequency domain aliasing are also considered for these conditions.

4. In chapter 4, correction filters are designed for optimized spectral response from a two-dimensional spatial filter of limited size. Use of these filters is shown to be superior to a higher order Levander scheme. Finally, the effect of these filters on a model with two contrasting velocities is shown.

5. Chapter 5 explains the theory for a new transmitting boundary condition for the acoustic wave equation. This method is then adapted to the elastic wave

equation, and applied to two cases.

6. Chapter 6 consists of finite-difference case studies, most without corrections. They do demonstrate some novel methods, and simulate some subtle features on seismic records.

   (a) Rayleigh wave reflection and transmission properties are shown in section 6.1.

   (b) A realistic example of the relationship between first breaks and seismic polarity is demonstrated for several cases in section 6.2.

   (c) Models of several standard AVO reflections with realistic transmitted waves are displayed in section 6.3.

1.2 Claims of novelty

The more significant claims of novelty are summarized here:

1. Unique body wave corrections are derived for each term of the two-dimensional wave equation. This tends to eliminate effects which are dependant on the orientation of the spatial grid, like frequency content and propagation velocity.

2. A correction for integration in time is combined with the corrections for spatial derivatives before approximations are made. This is important because the two corrections tend to oppose one another, and correcting for only the net effect can be much more efficient.

3. Corrections in the form of a limited length spatial filter are optimized for their spectral content. This can be important because a correction that is optimized

is usually more effective than one that results from the truncation of an infinite series. Frequency content is a measure that is widely used, and so seems a logical target for optimization.

4. The Courant stability criterion is presented in terms of aliasing in the time domain. The basic conclusions of this presentation are no different from present knowledge. However, they show a different viewpoint that can be used in the design of correction filters that avoid instability problems.

5. An effective transmitting (non-reflecting) boundary condition is developed using the eikonal equation. This has found some application in case studies. The value is limited, probably because corrections have not yet been developed for it.

6. A technique for generating isolated Rayleigh waves is developed. The separation of these waves from the body waves that physically cause them allows their inherent properties to be studied more easily.

7. A colour coded displacement direction display is developed. This display is effective for body and surface waves in a two dimensional medium, and can sometimes make clear how the separate waves are coupled.

8. A colour coded display of separated pressure and shear wave energy is developed. This is a display that interprets displacements in a two dimensional medium as pressure or shear waves, or a combination of the two. It has proved to be very effective at demonstrating how shear waves are generated, and how prevalent they can be in a structured medium.

These innovations all enhance the utility of finite-difference wave-equation modelling. Some of the benefits are quite significant, while others may be considered marginal. Many of these claims involve novel perspectives, but in practical terms they just make the modelling process more efficient, or for the same amount of computational effort, more accurate. Most finite-difference modelling problems may be bypassed with more sample points over the same spatial and time ranges. However, this can often be a very costly solution, increasing to the power of the number of dimensions in the output space. Better results can often be attained with an improved understanding of where the errors originate, and where new techniques will lead to significant improvements. For these reasons, novel perspectives sometimes have major impacts.

1.3 The use of frequency domain analysis in finite-difference modelling

Many of the claims of novelty within this thesis involve the modification of the basic finite-difference operators by comparatively minor operators designed in the frequency domain. This has not been done in a theoretical or general way, but has focused on the particular second derivative equations used for seismic wave propagation.

A geophysicist accustomed to the methods of the seismic industry may take some time to become aware of the different approaches taken for finite-difference modelling. A common understanding would seem natural, since sampled data is the basic working material for both groups.

The variance seem to arise from the different position of sampling within the order of operations. The seismologist samples his data at the beginning of his project, and from there he must do as much as possible with it. A mathematician who uses finite-difference techniques to solve differential equations first sets up his methods, and then continues to refine the sampling of his curves until he can compute satisfactory results.

It is interesting to note that many of the concerns of the seismologist, as he acquires and processes his data, depend on its frequency content.

1. The rationale for acquiring new data is often to obtain higher frequencies, enough to delineate uniquely a particular geologic target.

2. At acquisition, a primary concern is the time sample rate. This is chosen to obtain a sufficiently high 'Nyquist' frequency, the highest frequency which can be unambiguously preserved at a given sample rate. This is always chosen with a generous margin of error. Data frequencies which exceed the Nyquist frequency are suppressed by analogue means before sampling takes place.

3. An important part of post acquisition processing involves selection of frequency content by filtering. High, or low, or particular frequencies are usually suppressed to enhance those remaining, those which have been identified with interesting targets.

4. A further part of seismic processing involves frequency balancing. This usually means enhancing the amplitude of the higher frequencies in the data compared with those at lower frequencies. This is one way of looking at the deconvolution process.

These processes are applied mainly in the time domain, but are designed for their response in the frequency domain. The Nyquist frequency dictates time acquisition sampling, and the time domain band-pass and deconvolution filters are designed for manipulation of the frequency content of the data. These last two processes involve some quite complex theory.

In contrast to the seismologist, the finite-difference mathematician will focus entirely on 'schemes'. A scheme amounts to the replacement of derivatives from a differential equation with some form of finite-difference analogue, along with a limited number of additional techniques (See Appendix A.4). These schemes, and the sample rates used within them, are evaluated by analysis and comparison with analytic results to arrive at an optimum scheme for the problem at hand.

It is interesting that, although no frequency domain processes are applied to the data, most of the quantitative analysis of schemes is done in the frequency domain. This is necessary because the effects being studied are often dependent on frequency or wavenumber.

The most widely used frequency domain analysis of finite-difference schemes is the von Neumann analysis. The result of this analysis is essentially the Fourier transform of a single time step, and is called the amplification factor. A quote from Strikwerda (2004) states "All the information about a scheme is contained in its amplification factor". He then goes on to say ".....and we show how to extract important information from it." (page 194). Conditions for stability are probably the most important of these, but also available are measures of accuracy, dispersion, and phase angle.

The proven validity and importance of Fourier domain concepts within finite-

difference theory seems to point directly to the utilization of frequency domain designed techniques to enhance the method, and some encouraging results have been achieved. A large part of this thesis takes this approach to enhance the accuracy and efficiency of wave equation modelling.

Chapter 2

Finite-difference modelling in one spatial dimension

The study of finite-difference modelling of waves in one dimension is a valuable introduction to the more physically meaningful problems in two or three dimensions. Aki and Richards (1980) used this approach to find modelling styles and parameters that provide stability, and to make estimates of numerical dispersion. Another example of stability analysis can be found in Press et al. (1992), where the notation is similar to that used in geophysics, and several different approaches are used. These problems of stability and numerical dispersion usually have solutions which are opposed to each other, and therefore tend to receive the most attention in finite-difference practise. Their definitions are given in Appendix C.2.

Ames (1992) investigates the one dimensional wave-equation in his book. He uses the usual formulation, but then to improve general stability, discusses an implicit scheme where the acceleration is approximated by 'the divided second backward difference'. After analysis he finds the results to be attenuated, and writes 'This improper attenuation renders the finite-difference approximation of little use in approximating the wave-equation' (page 283). This seems to be a general comment on finite-difference wave-equation solutions.

Finite-difference computations require a choice of spatial and temporal sample rates. Lines et al. (1999) quote earlier authors that "... spatial sampling is generally

chosen to avoid grid dispersion in solutions. Then, having chosen spatial sampling, the temporal sampling is chosen to avoid numerical instability". This direct approach will work, but may require fine sampling rates that result in long computation times. Here it will be shown that the temporal sample rate also affects the amount of dispersion.

The oversampling required to limit numerical dispersion is necessary when the derivatives of the analytic equation are replaced with their most simple finite-difference equivalents. Alternatively, numerical dispersion can be limited by improving the accuracy of finite-difference approximations, which usually amounts to extending their length, and thus moving errors to terms of higher order in their Taylor series approximations. An example is the finite-difference first derivative, which in the simplest case has two terms, and which can be extended to higher orders containing 3 or more terms by involving adjacent grid points. One example of how a higher order approximation is designed is given in Appendix A.6. Some of these methods were developed for early automatic computers and have had a rich history since. Abramowitz and Stegun (1965), for example, list a number of finite-difference formulae for partial derivatives, some accurate to fourth order.

Another method of improving finite-difference accuracy is to make use of the exact spatial differentiation possible in the wavenumber domain. This is known as the pseudospectral method, and Kreiss and Oliger (1972) were the first to publish it. Orszag (1972) and Fornberg (1975) also published early papers in mathematical journals. Gazdag (1981) and Kosloff and Baysal (1982) used the technique for two dimensional seismic modelling. There are two main difficulties with the pseudospectral method. First, the operators which are so simple and compact in the Fourier

domain, are effectively quite wide spread in the spatial domain, causing difficulties at the edges and at internal boundaries. Second, the high accuracy derivatives in the spatial domain do not have a natural integration equivalent in the time domain. This is because each time step of the finite-difference method adds a new sample to the end of a series, and a reliable Fourier transform of this time series cannot be made with these conditions. For this reason, the calculated acceleration is transformed back to the space domain, and usually finer time steps are used.

This thesis describes a new method for the time stepping of waves, and for analyzing the error and stability of the finite-difference method, by developing and using an exact relationship, valid for a single Fourier component, between the second-order, central, second finite-difference and the analytical second derivative. The relationship is exact because it is developed entirely in the Fourier transformed domain, whereas other methods operate within a space/time domain or a wavenumber/time (the pseudospectral) domain. In the classic finite-difference literature, this relationship is closely related to the 'amplification factor'. It is used there as a quality check for a particular scheme (see section 1.3 and Strikwerda (2004) page 194 for the wave equation).

The amplification factor allows the finite-difference error to be precisely characterized and a correction filter to be developed. The correction filter can be applied to second-order finite-difference results to remove grid dispersion and also to stabilize an apparently unstable scheme.

The following six sections develop the theory and practice of multiplicative corrections for the wave equation in one spatial dimension.

- Section 2.1 begins the correction theory by comparing the results of analytic second derivatives and their finite-difference analogues. It then shows how the finite-difference results must be modified in order to produce the exact($\pm$) analytic results.

- Section 2.2 develops the results from section 2.1 into a practical time stepping scheme. The scheme is demonstrated with some simple examples. Since the corrections were developed in the wavenumber domain, the data were transformed to the wavenumber domain for application of the corrections, and then transformed back to the spatial domain.

- Section 2.3 shows how the corrections act to eliminate numerical dispersion. This is not immediately obvious because the basic correction operations affect amplitudes. The effects on dispersion are shown with some narrow band limited wavelet examples.

- Section 2.4 shows a particular case where the corrections can eliminate finite-difference time-stepping instability.

- Section 2.5 uses the results from the previous section to present the instability problem in a slightly different way. Some may find they have a better understanding of stability requirements from this viewpoint.

- Section 2.6 develops the theory of correction filters for application in the spatial domain. The filters are optimized for their effect within the lower frequency part of the spectrum, with a constraint on the filter length. These filters save computer time spent on Fourier transforms, and are easier to use on a model

with more than one velocity. The filters are demonstrated on a model with two velocities.

2.1 The analytic second derivative simulated by finite-difference

This section will show how the a finite-difference second-order second derivative analogue may be modified to simulate an analytic second derivative. The general procedure is shown graphically in Figure 2.1. The primary concern is to ensure that a continuous operation is replicated as closely as possible by its discrete analogue. If this can be done with sufficient accuracy, the legacy of analytic successes can be claimed for their discrete equivalents. The comparison is made in the discrete (sampled) domain because there are a finite number of measurements to make, and because the conversion from the continuous to the discrete domain is well understood.

A similar philosophy is used by Mickens (2000) for his exact equations. In Mickens' book, the sampled points derived from the finite-difference equation must lie exactly on the continuous curve of the analytic equation solution. He expresses this condition in the form

$$u_k = u(t_k), \tag{2.1}$$

where u is the continuous function, t_k is a discrete time, and u_k is the finite-difference calculated value at that time. This appears on page 6 of his text.

The discrete operation which will be compared here to the continuous operation is the second derivative, which appears many times within the various wave equations. This would be a difficult task in general, but may be seen to be quite amenable in the Fourier transformed domain. The procedure, then, is to compare the output of

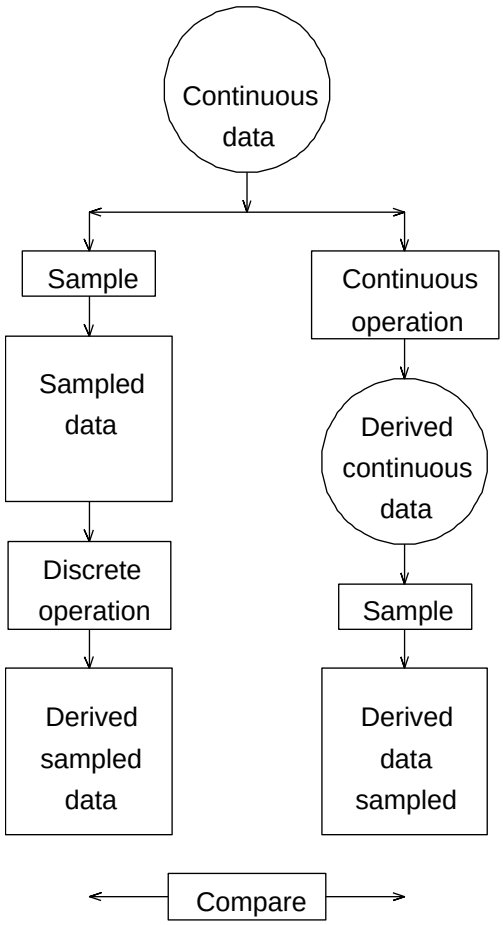

Figure 2.1: The means by which the continuous and discrete operations are compared. The continuous operation is used as a model, and the discrete operation is modified to obtain a result which is as similar as possible

the continuous and discrete operations on a single frequency and wavenumber wave. The results will then depend on the frequency and wavenumber of the wave chosen.

The solution of the analytic wave equation has been given many times, but is repeated here to ensure a consistent notation. First note that the one-dimensional (scalar) wave equation can be written in the form

$$\frac{\partial^2 \phi}{\partial x^2} = \frac{1}{v^2}\frac{\partial^2 \phi}{\partial t^2}, \tag{2.2}$$

where ϕ is the 1-D wavefield, x and t are the space and time coordinates, and v is the velocity, or acoustic wavespeed.

If the wavefield is limited to a particular wavenumber k and frequency ω, it can take the complex exponential form

$$\phi(x, t, k, \omega) = e^{i(kx-\omega t)}, \tag{2.3}$$

where the wave amplitude has been set to unity. The second partial derivatives of equation 2.3 are

$$\frac{\partial^2 \phi(x, t, k, \omega)}{\partial x^2} = -k^2 e^{i(kx-\omega t)} \tag{2.4}$$

$$\frac{\partial^2 \phi(x, t, k, \omega)}{\partial t^2} = -\omega^2 e^{i(kx-\omega t)}. \tag{2.5}$$

Substitution of 2.4 and 2.5 into 2.2 shows that k and ω must be related as

$$k = \pm\frac{1}{v}\omega. \tag{2.6}$$

For comparison, the finite-difference equivalent operator may be applied to a continuous wave field. The second order, central finite-difference of a function $f(\xi)$ is usually written as $D_\xi^2 f(\xi) = (\Delta\xi)^{-2}[f(\xi + \Delta\xi) - 2f(\xi) + f(\xi - \Delta\xi)]$ and is taken

as an approximation to the analytic second derivative. Applying this operator to the wavefield of equation 2.3 in the spatial coordinates gives

$$D_x^2\phi(x,t,k,\omega) = \frac{1}{(\Delta x)^2}\{e^{i(k(x+\Delta x)-\omega t)} - 2e^{i(kx-\omega t)} + e^{i(k(x-\Delta x)-\omega t)}\} \tag{2.7}$$

or

$$D_x^2\phi(x,t,k,\omega) = \frac{e^{i(kx-\omega t)}}{(\Delta x)^2}\{e^{ik\Delta x} - 2 + e^{-ik\Delta x}\}. \tag{2.8}$$

The terms in curly brackets may be written as

$$e^{ik\Delta x} - 2 + e^{-ik\Delta x} = \{e^{ik\Delta x/2} - e^{-ik\Delta x/2}\}^2 = -4sin^2(k\Delta x/2) \tag{2.9}$$

so that equation 2.8 becomes

$$D_x^2\phi(x,t,k,\omega) = -k^2(\frac{2}{k\Delta x})^2 sin^2(\frac{k\Delta x}{2})]e^{i(kx-\omega t)}, \tag{2.10}$$

or

$$D_x^2\phi(x,t,k,\omega) = -k^2 sinc^2(\frac{k\Delta x}{2})e^{i(kx-\omega t)}, \tag{2.11}$$

using $sinc(\xi) = sin\xi/\xi$. Comparing equations 2.4 and 2.11 leads to the conclusion that

$$D_x^2\phi(x,t,k,\omega) = sinc^2(\frac{k\Delta x}{2})\frac{\partial^2\phi(x,t,k,\omega)}{\partial x^2}, \tag{2.12}$$

or

$$\frac{\partial^2\phi(x,t,k,\omega)}{\partial x^2} = \frac{1}{sinc^2(\frac{k\Delta x}{2})}D_x^2\phi(x,t,k,\omega). \tag{2.13}$$

There are zeros of the sinc function in equation 2.13 but not for the normal range of the argument. The first zeros occur at $k_0 = \pm 2\pi\Delta x^{-1}$, which is twice the Nyquist wavenumber (see Figure 2.2).

By a similar process it follows that

$$\frac{\partial^2\phi(x,t,k,\omega)}{\partial t^2} = \frac{1}{sinc^2(\frac{\omega\Delta t}{2})} D_t^2\phi(x,t,k,\omega). \tag{2.14}$$

Substituting equations 2.13 and 2.14 into equation 2.2 provides an exact finite-difference equivalent for the 1-D scalar wave equation, which is

$$\frac{1}{sinc^2(\frac{k\Delta x}{2})} D_x^2\phi(x,t,k,\omega) = \frac{1}{sinc^2(\frac{\omega\Delta t}{2})} \frac{1}{v^2} D_t^2\phi(x,t,k,\omega) \tag{2.15}$$

where now finite-difference operators are used. It must now be emphasized that this result is only valid for a single Fourier component.

This equation was also developed by Cole (1998), and appears in Mickens (2000), the book on non-standard finite-differences.

If equation 2.15 is modified by replacing the sinc functions with unity and discarding the wavenumber and frequency dependence of ϕ, the conventional second-order finite-difference approximation results. This introduces frequency and wavenumber dependent errors that are precisely characterized by the sinc functions. The form of the sinc function is shown in Figure 2.2.

Division by zero is usually not a problem with these sinc functions. Consider, for example, the sinc function associated with the x derivative, and assume that the relevant wavenumbers are contained within ±Nyquist. Then the relevant values of k are contained within $[-\pi\Delta x^{-1}, \pi\Delta x^{-1}]$, and it follows that the sinc function arguments fall within $[-\pi/2, \pi/2]$ radians. Figure 2.2 shows that the sinc fuction is not near zero for this range.

Neglecting the multiplicative, sinc-function factors in equation 2.15 leads to the errors described in the Appendix C.2. The closer the factors are to 1 the smaller the

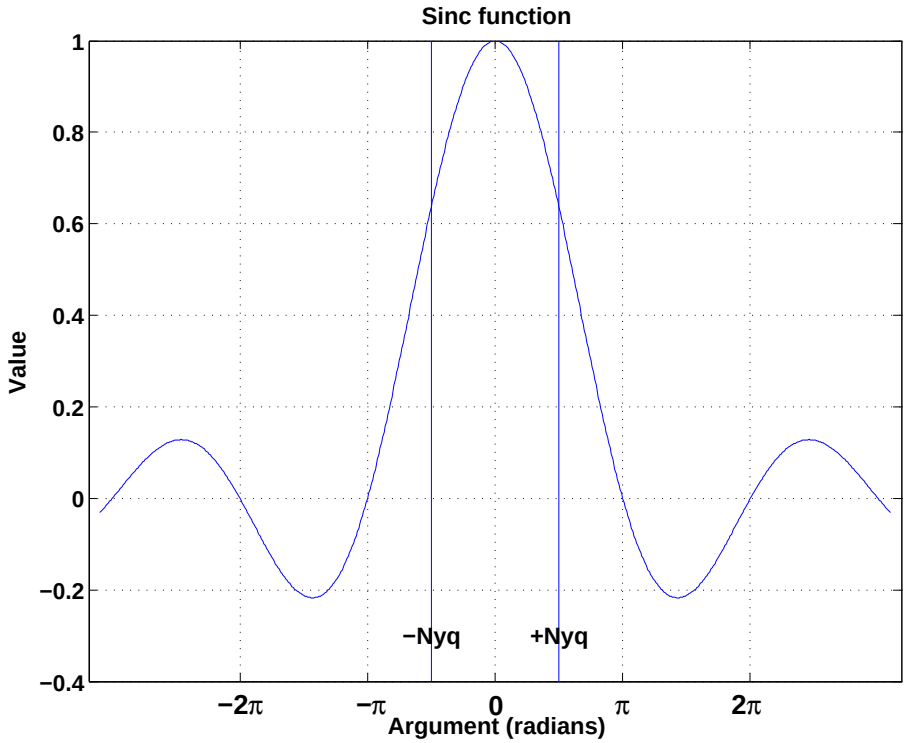

Figure 2.2: The sinc function, with the most relevant portion between the Nyquist wavenumbers marked.

errors, and the factors approach 1 as the sinc-function arguments approach 0. This means that the errors are reduced when the relevant sample interval is reduced, or the frequency and wavenumber are reduced.

The maximum error is usually at the highest wavenumber or frequency that is sufficiently sampled, or the Nyquist wavenumber. For example, the positive Nyquist wavenumber is $\pi/\Delta x$, so that $sinc(k\Delta x/2)$ becomes $sinc(\pi/2)$, or half way to the first zero of the function. The sinc function factor in this range, then, is always greater than zero. Equation 2.13 shows that the second-order finite-difference always underestimates the magnitude of the analytic derivative and the underestimate is given in Figure 2.3. This curve is the square of the sinc function, and it must be divided into the finite-difference derivative to get the exact derivative. The finite-difference result is most accurate where the sample interval is small, or where wavenumber or frequency are low. The curve does not go to zero within the usual range (within the Nyquist frequencies), so this curve also shows it is valid to divide by the sinc function and its square.

2.2 Finite-difference time stepping including a correction filter

This section will show how an extension of equation 2.15 can be developed for use in a time-stepping scheme. First, equation 2.15 may be solved for the finite-difference acceleration term to give

$$D_t^2\phi(x,t,k,\omega) = v^2 \frac{sinc^2(\frac{\omega\Delta t}{2})}{sinc^2(\frac{k\Delta x}{2})} D_x^2\phi(x,t,k,\omega). \tag{2.16}$$

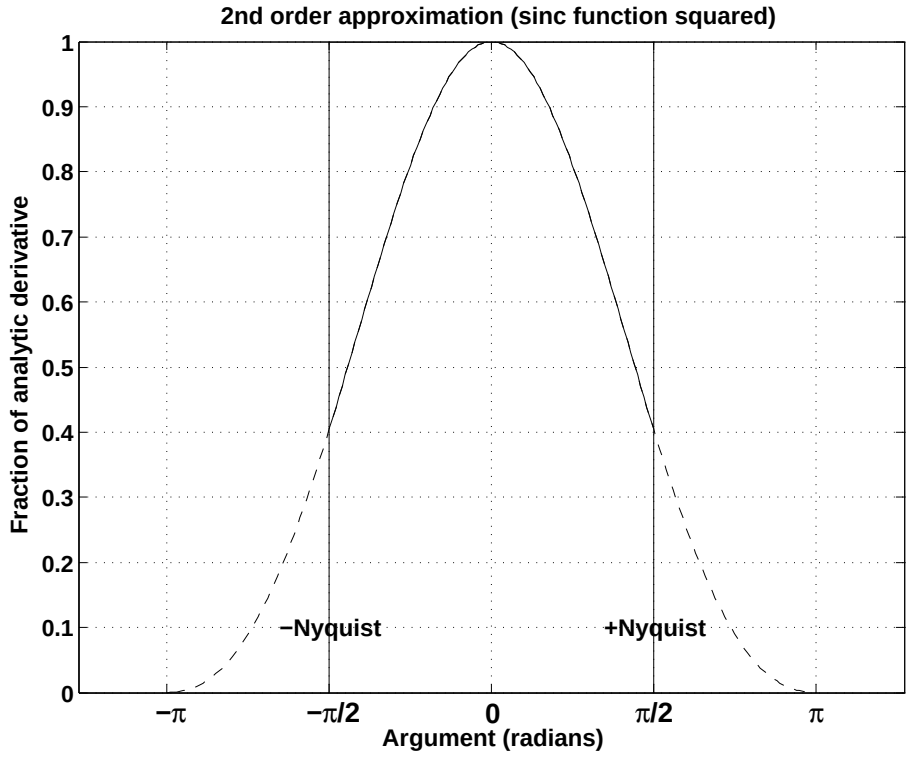

Figure 2.3: The finite-difference under estimate of a second derivative (a squared sinc function).

As it stands, the sinc function in the numerator on the right side of equation 2.16 is problematic because it requires knowledge of the temporal frequency ω, a quanity not readily known in time-stepping. Frequencies are not available from the incomplete time series being constructed, but the assumption of constant velocity makes the translation into wavenumbers obvious. Thus, equation 2.6 is used to substitute for ω, the explicit ω dependence is dropped from ϕ, and D_t^2 is expanded to obtain

$$\frac{\phi(x,t+\Delta t,k)-2\phi(x,t,k)+\phi(x,t-\Delta t,k)}{(\Delta t)^2}=v^2\frac{sinc^2(\frac{kv\Delta t}{2})}{sinc^2(\frac{k\Delta x}{2})}D_x^2\phi(x,t,k). \quad (2.17)$$

The solution for time-stepping is then

$$\phi(x,t+\Delta t,k)=\left[2+(\Delta t)^2v^2\frac{sinc^2(\frac{kv\Delta t}{2})}{sinc^2(\frac{k\Delta x}{2})}D_x^2\right]\phi(x,t,k)-\phi(x,t-\Delta t,k). \quad (2.18)$$

This finite-difference time-stepping equation has a form similar to the standard second-order equation, but in addition has a *correction multiplier* in the form of the squared sinc-function ratio. Since equation 2.18 is just a reformulation of equation 2.2, it is an exact prescription for a finite time step assuming a single Fourier component. When the correction multiplier is set to unity, exactness is lost and the standard time-stepping approximation results.

Equation 2.18 has been used by Cole (1998) to time step narrow band wavelets. In the literature seen to date, this equation has not been used for broad band frequency correction, or to design convolution operators to achieve similar results.

It is interesting to look at the correction filter from a frequency domain viewpoint. The phase spectrum of the finite-difference operation is untouched. The operation is fully corrected by a simple adjustment of the amplitude spectrum. Since most of the information in a signal is carried by the phase spectrum, it is encouraging to note that the correction operator is such a simple adjustment.

Equation 2.18 can be implemented in a practical scheme by applying the second spatial finite-difference followed by a wavenumber dependent correction filter before calculating the time step advance. The sequence of operations is shown in Figure 2.4.

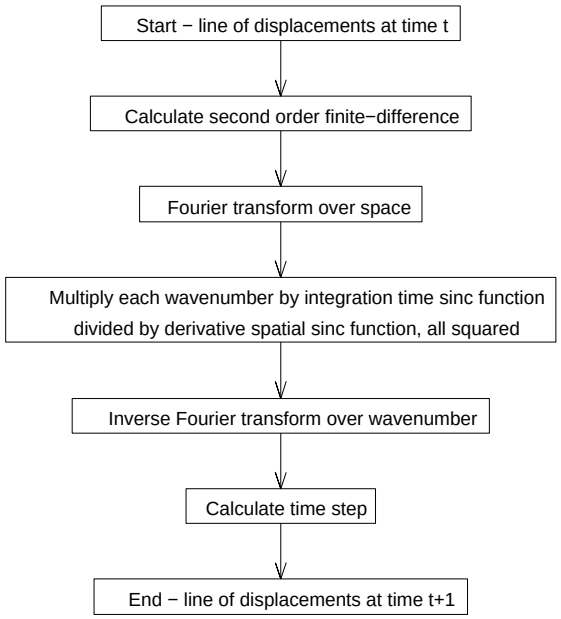

Figure 2.4: The flow chart for application of the correction multiplier to one dimensional finite-difference time-stepping. Note that the integration step is corrected as well as the spatial derivative.

An example of finite-difference modelling using the corrected equation is shown in Figure 2.5. The wavelet has remained quite consistent through the duration of the model. For comparison, the equivalent uncorrected equation 2.19 propagates an identical initial wavelet through the successive steps shown in Figure 2.6. The most obvious difference to be seen is the change in character of the propagated wavelet

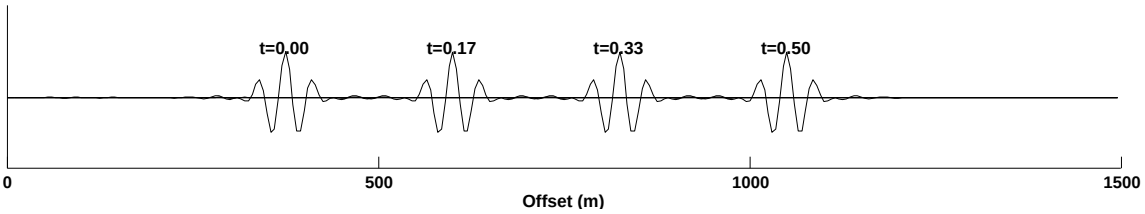

Figure 2.5: A zero phase wavelet that has started at t=0 and propagated to the right with the algorithm from equation 2.18.

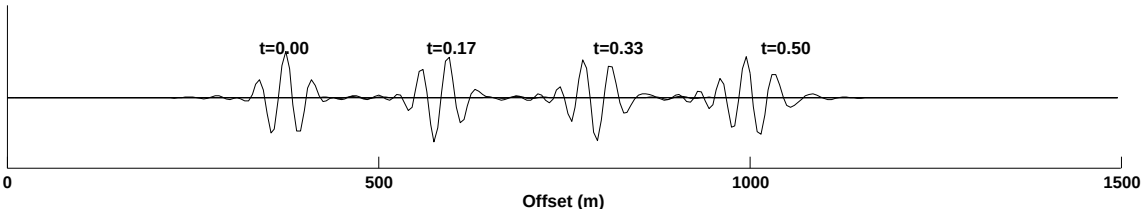

Figure 2.6: The wavelet from Figure 2.5 was propagated uncorrected with equation 2.19.

caused by numerical dispersion.

2.3 The uncorrected equation and velocity dispersion

Some of the most convincing evidence for the accuracy of the corrected time-stepping equation is its use for prediction of uncorrected propagation effects. As an example, the second-order time stepping scheme may be analysed to develop an expression for its grid dispersion velocity. This standard approximation arises by setting the correction filter to unity in equation 2.18 to obtain

$$\phi(x, t + \Delta t) = \left[2 + (\Delta t)^2 v^2 D_x^2\right] \phi(x, t) - \phi(x, t - \Delta t). \tag{2.19}$$

From this perspective, equation 2.19 is an approximate solution to the time-stepping problem whose errors are characterized by the omitted correction filter. However, it can also be viewed as the exact solution to a different problem, that of

modelling in a particular wavenumber-dependent velocity medium. Notice that in equation 2.15, there are no conditions on the velocity, and so it may be defined as wavenumber dependent.

To show the wavenumber-dependent velocity medium which is exactly modelled by equation 2.19, consider the quantity within the square brackets. This may be written as

$$\left[2 + (\Delta t)^2 v^2 \frac{sinc^2(\frac{k\Delta x}{2})}{sinc^2(\frac{ku(k)\Delta t}{2})} \frac{sinc^2(\frac{ku(k)\Delta t}{2})}{sinc^2(\frac{k\Delta x}{2})} D_x^2\right], \tag{2.20}$$

where the wavenumber dependent velocity $u(k)$ at this point can be any completely arbitrary number. Now define $u(k)$ with the following implicit equation

$$u(k) = v \frac{sinc(\frac{k\Delta x}{2})}{sinc(\frac{ku(k)\Delta t}{2})}. \tag{2.21}$$

Here $u(k)$ appears in the equation twice. The equation may be manipulated to give an expression for $u(k)$, but this does not lead to a major increase in understanding (see Appendix K). A squared version of this equation 2.21 may be used to substitute $u(k)^2$ for the left fraction in the square bracket 2.20. The remaining terms in the square bracket are then in the exact form of equation 2.18, and so an event with wavenumber k will propagate perfectly with a velocity given by equation 2.21. Note that the velocity which is used for the time stepping procedure is distinct from the velocity with which any wavenumber propagates. Also note that with some effort, an explicit equation $u(k)$ may be developed (see Appendix K), but a reasonable approximation is

$$u(k) = v \frac{sinc(\frac{k\Delta x}{2})}{sinc(\frac{kv\Delta t}{2})}. \tag{2.22}$$

The velocity dispersion in equation 2.21 is seen to arise from the finite-difference approximations to both the space and time derivatives. The ratio of sinc functions

means that the errors in these approximations tend to oppose one another, and even completely cancel if $v\Delta t = \Delta x$.

The wavenumber dependent velocity equation may be used to predict the action of numerical models. Note that stable modelling requires that $\Delta t \leq \Delta x/v$ (see, for example, Lines et al. (1999). Then $v\Delta t \leq \Delta x$, and if this inequality is inserted into equation 2.22, it turns out that that $u(k) \leq v$. Also, this inequality is increased with higher wavenumbers k, so if $k1 > k2$ then $u(k1) < u(k2)$. This effect may be seen in Figure 2.6, where the wavelet has not propagated as far, and therefore not as fast, as the corrected wavelet in Figure 2.5.

Another way to demonstrate the results of uncorrected finite-difference wave propagation is to study its effects on wavelets with very limited bandwidth. Since the propagation effects are frequency dependent, a limited bandwidth wave will show more consistent effects. Figure 2.7 shows the use of equation 2.19 to propagate two narrow bandwidth waves, constructed as single frequency waves modulated by a Gaussian. The lower frequency wave has traveled farther, and therefore faster, than the higher frequency wave.

The high frequency wave packet result can be quantified by crosscorrelating the propagated wavelet with the original limited bandwidth wavelet and plotting the position of the crosscorrelation maximum. The result is the jagged curve appearing in Figure 2.8 (the jagged nature is explained in the paragraph following). The uppermost curve indicates the real velocity of the material and the next curve indicates the phase velocity (equation 2.22). The wavelet should move at the group velocity, $d\omega/dk$, calculated from the phase velocity (see the Appendix K). This is the third straight line on the plot, and it follows the trend of the crosscorrelations very well.

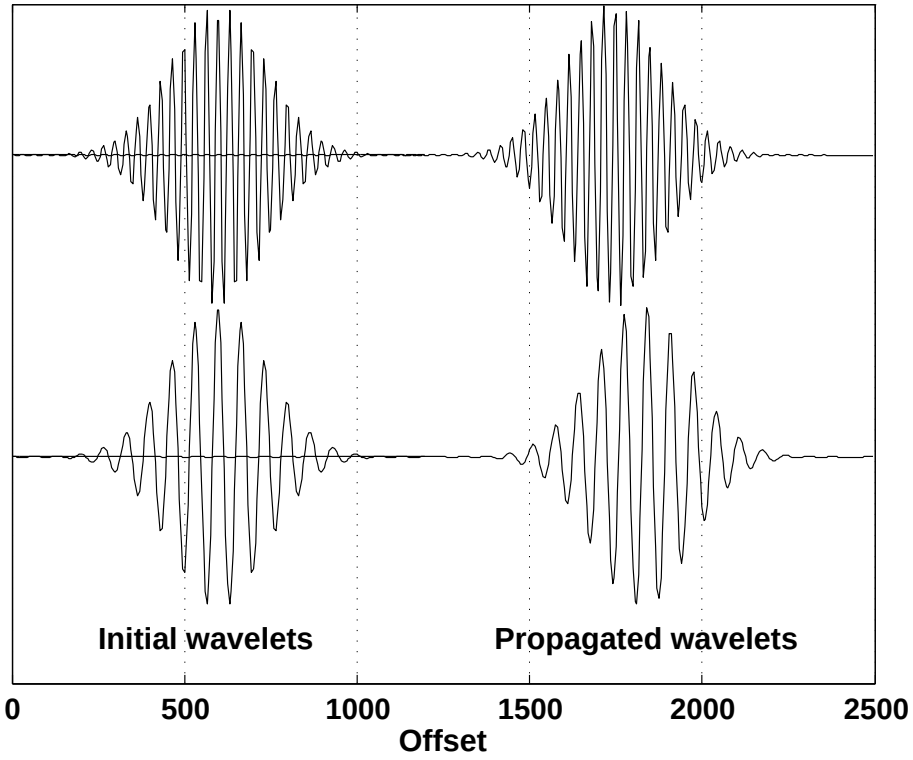

Figure 2.7: Two different narrow-band wavelets propagating to the right using equation 2.19. Snapshots taken at the same time show the relative positions of the two wavelets. The lower frequency wavelet has moved further because its effective velocity was higher.

It is difficult to correlate the high frequency wavelet packages because while the packet moves at the group velocity, the high frequency component of the packet moves at its phase velocity. This means the high frequency component moves within the packet, and the cross correlation tracks the high frequency for detail, even though the general trend follows the packet.

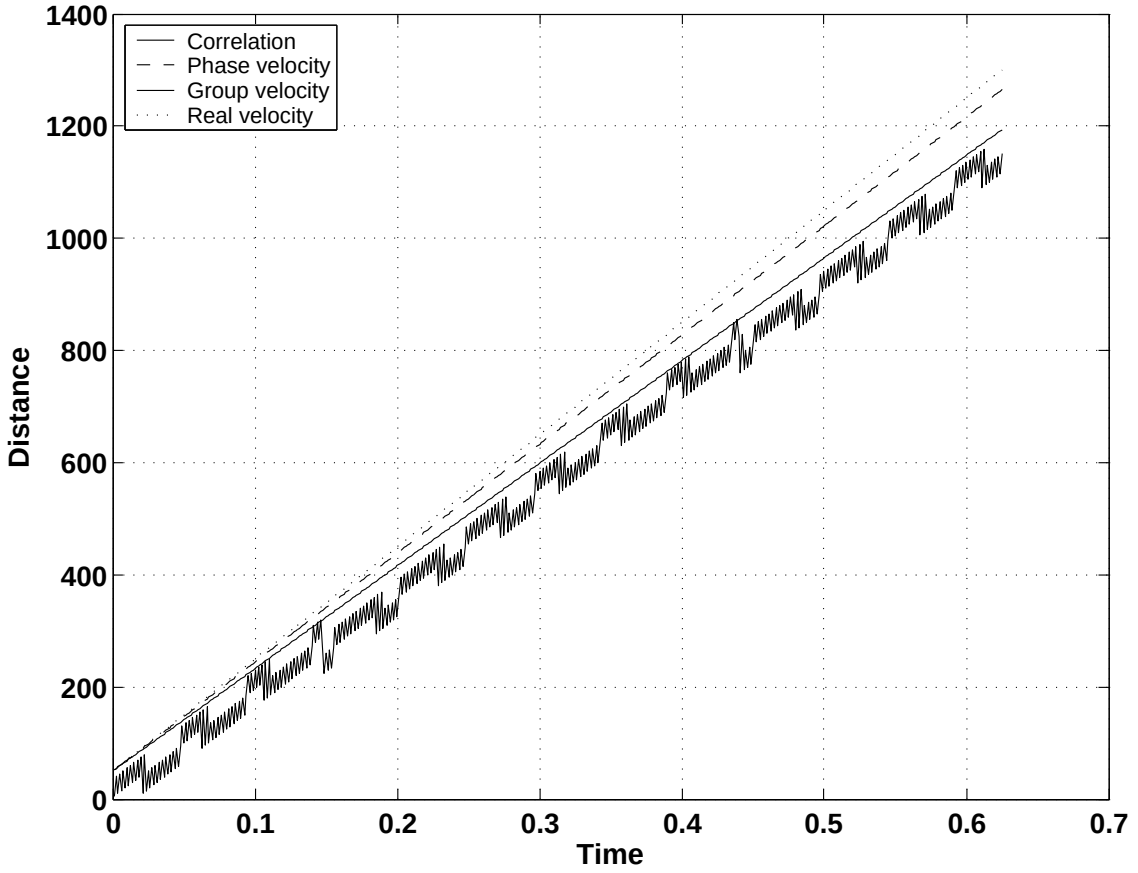

Figure 2.8: The jagged curve shows the position versus time of the high-frequency wavelet (of Figure 2.7) as determined by crosscorrelating successive snapshots. Propagation was accomplished with equation 2.19. Also shown are straight lines indicating the phase velocity (dashed, equation 2.22), group velocity (solid, derivative of equation 2.22), and the material velocity (dotted).

When the band limited wavelets are propagated with the corrected finite-difference

expression (equation 2.18), the results shown in Figure 2.9 are obtained. Both

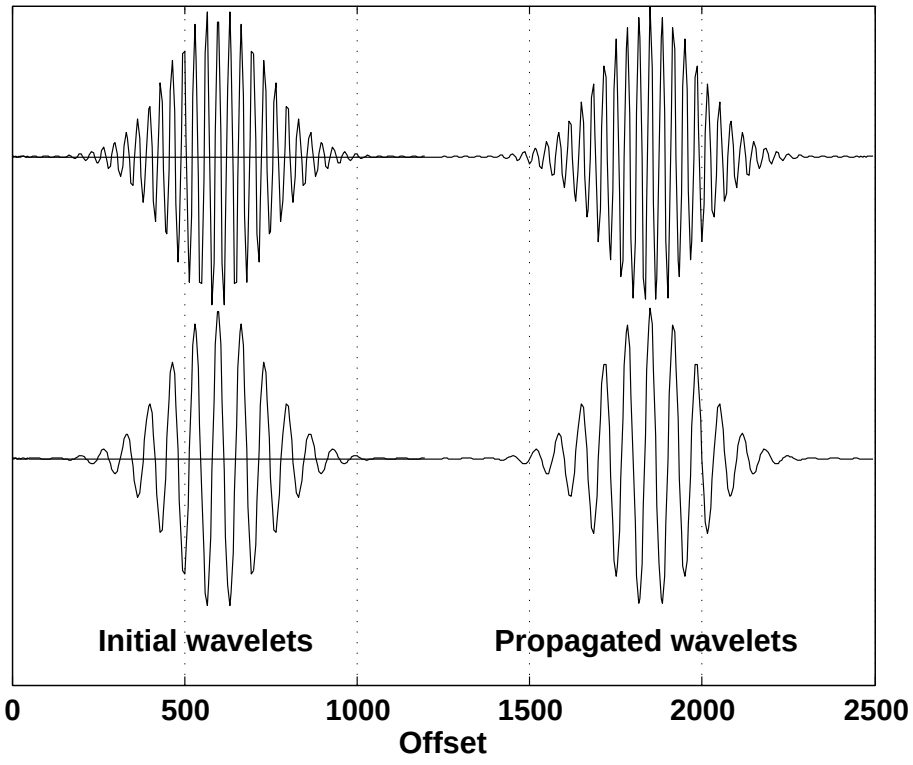

Figure 2.9: The two narrow-band wavelets propagating to the right using equation 2.18. They have moved at a higher velocity which is independent of frequency.

wavelets propagate much further with the same number of time steps, and the two go about the same distance. The cross correlation results are shown in Figure 2.10 and they have the same slope as the actual velocity of the model.

The final method used to evaluate the correction theory predictions is to investigate the nature of wavelet character change when the uncorrected equation is used. Figure 2.11 shows the lag of two frequency components from the material velocity position for a particular set of parameters ($v = 1000m/s, dx = 3m, dt = .0015s$). Also displayed is the distance the high wavenumber component must lag to reach

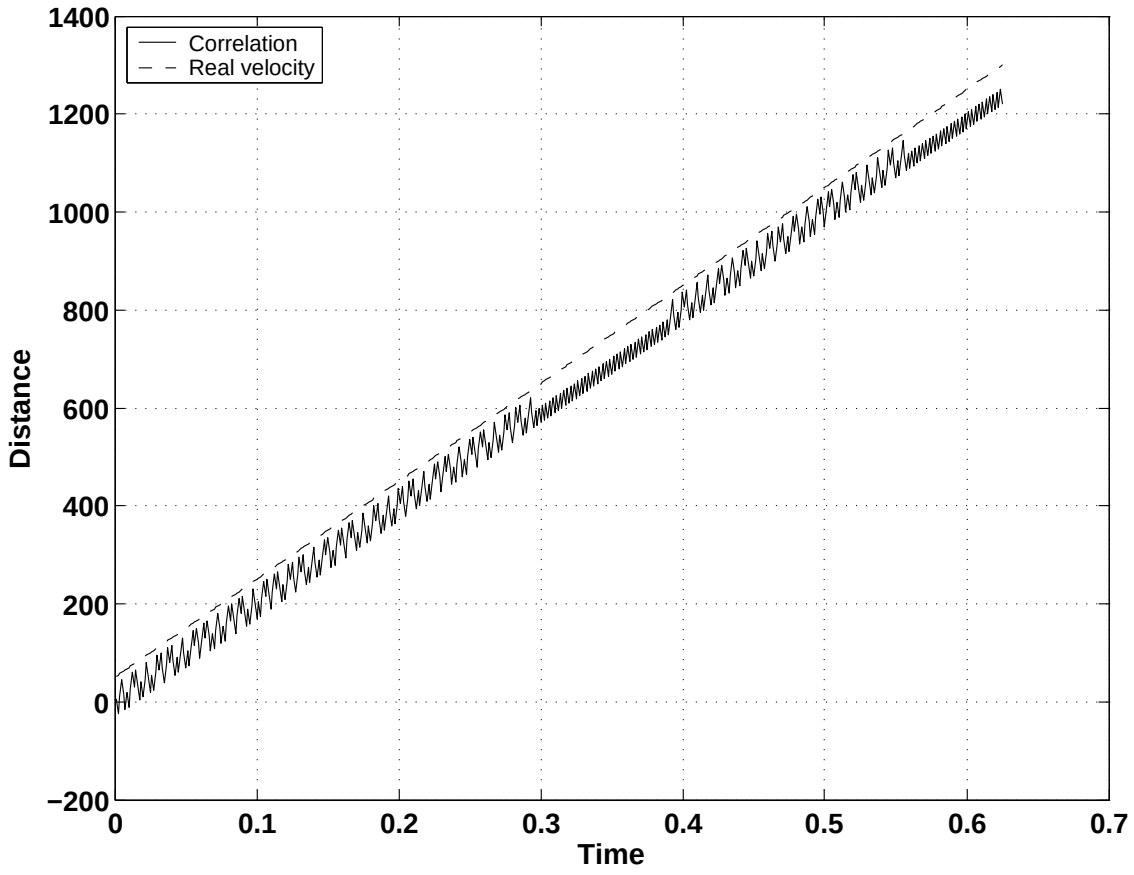

Figure 2.10: The jagged curve shows the position versus time of the corrected high--frequency wavelet (of Figure 2.9). Propagation was accomplished with equation 2.18. The straight line indicates the material velocity, and it follows the trend of the wavelet position.

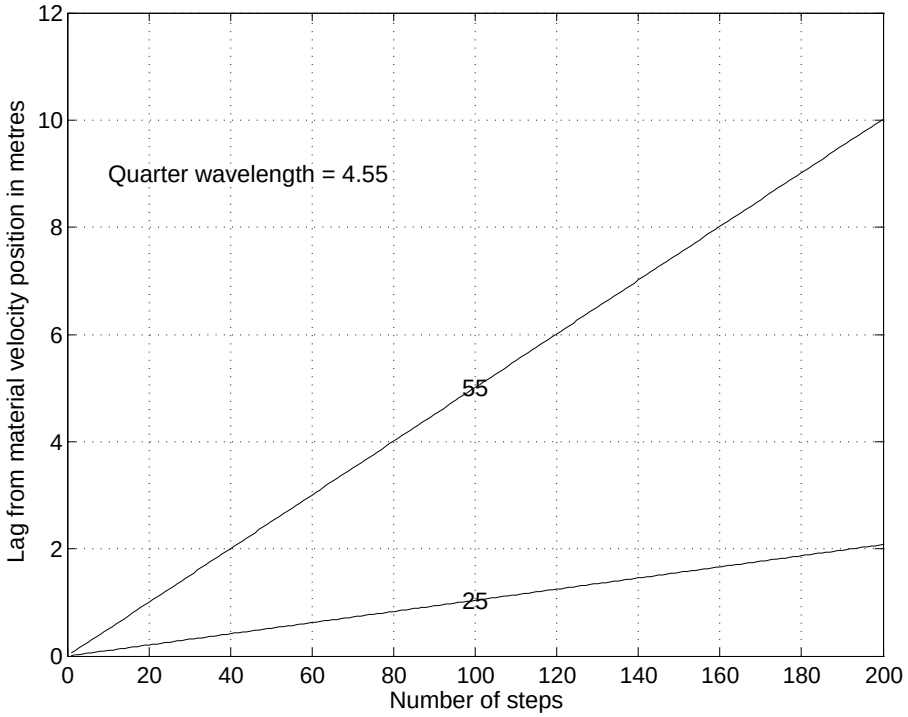

Figure 2.11: The total lag of the 25 and 55 Hz wavelet components after a given number of steps.

1/4 of its wavelength.

Figure 2.12 shows how a stack of several frequency components of uniform amplitude combine to make up a zero phase wavelet. The vertical line shows where the

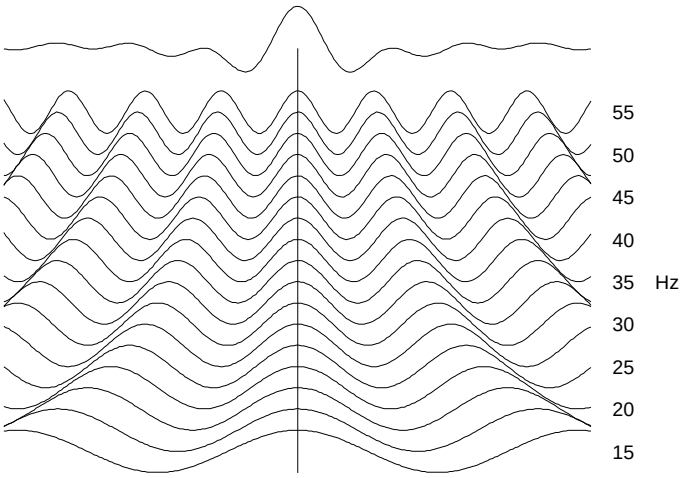

Figure 2.12: The zero phase wavelet plotted at the top is the sum of the frequency components plotted below it.

common phases (peaks) line up.

Figure 2.13 shows how a stack of frequency components may combine to make up a 90 degree phase shift wavelet. The vertical line here shows where the common phases (zero crossings) line up. From Figure 2.11 it may be seen that a quarter wavelet lag difference at 55 Hz will result after about 110 finite-difference steps. Each component in this Figure (2.13) is lagged by using the velocity from 2.22 times the time interval of 110 steps, in this case 0.165 seconds.

In Figure 2.14 the zero phase wavelet at the center is shown after propagating 110 steps to the right. The phase shift of approximately 90 degrees is apparent. Also the lagging high frequencies and leading low frequencies are beginning to show.

The wavelet has also been propagated a further 110 steps to 220, and the result

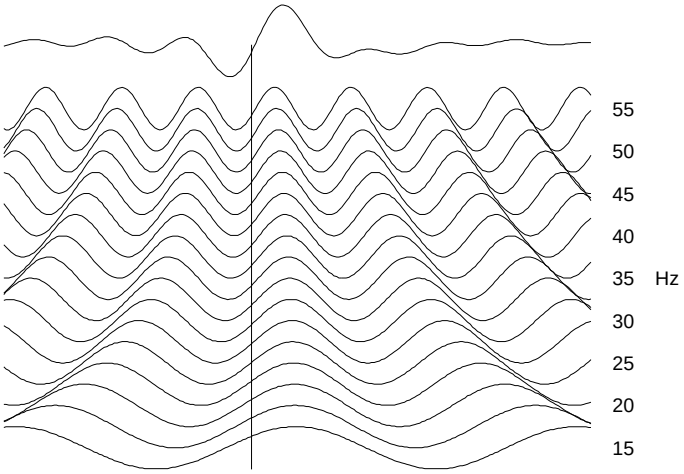

Figure 2.13: The plotted frequency components (shifted) may be summed to form the 90 degree phase wavelet plotted at the top.

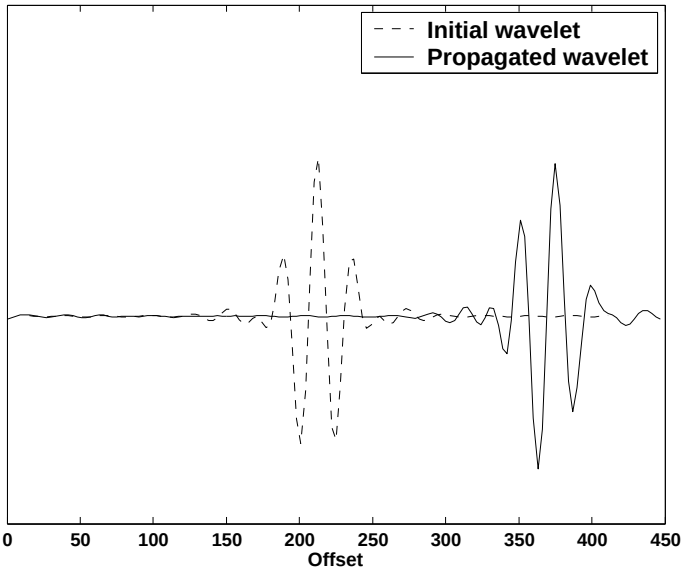

Figure 2.14: The wavelet propagated 110 steps. Note the apparent 90 degree phase shift.

is shown In Figure 2.15. The wavelet in this case has been wrapped around in the

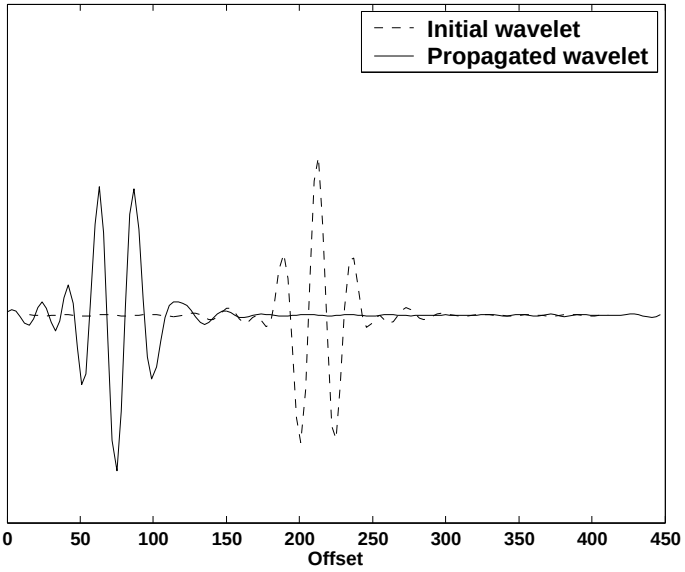

Figure 2.15: The wavelet propagated 220 steps, and wrapped around to the left. Note the apparent 180 degree phase shift(reversal).

x-direction, and has come in from the left to appear at the left of the initial wavelet. The further 90 degree phase shift gives a total shift of 180 degrees, or a polarity reversal from the initial wavelet. The wavelet does appear to be reversed, although more spread out.

A total of 440 propagation steps is shown in Figure 2.16, which has the appearance of a 360 degree phase shift. The growing separation of the high and low frequencies is also becoming more apparent.

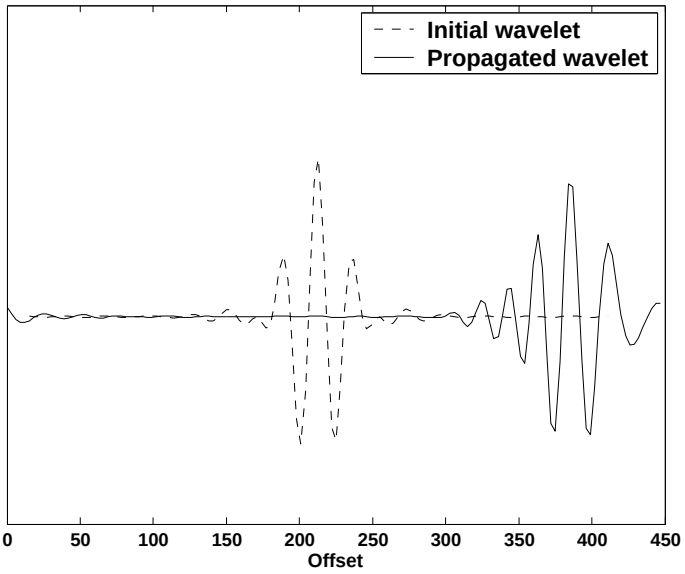

Figure 2.16: The wavelet propagated 440 steps. The phase shift here is about 360 degrees. The spreading out of the lower and higher frequencies is more obvious here.

2.4 Instability and dispersion when time-stepping

When finite-difference modelling, one of the primary concerns with a procedure is its stability. Here it will be shown that instability is another symptom of the basic mismatch between continuous and finite-difference derivatives, and that correction factors may contribute to understanding this mismatch. It has been found that spatial filters for unstable conditions must be designed with different methods from filters designed for stable conditions. This special design technique is discussed in Appendix J. However, one particularly favourable case will be shown here.

The omission of the correction multiplier, $corr = sinc^2(kv\Delta t/2)/sinc^2(k\Delta x/2)$, in equation 2.18 gives rise to instability for wavenumbers where the multiplier would be less than 1, and dispersive but stable wave propagation where it would be greater than 1. These relationships are sumarized in table 2.1.

Sampling choices	*corr* magnitudes	Uncorrected properties
$\Delta t < \Delta x/v$	$corr > 1$	stable/dispersive
$\Delta t = \Delta x/v$	$corr = 1$	stable
$\Delta t > \Delta x/v$	$corr < 1$	unstable

Table 2.1: Correction amplitudes related to the stability criterion.

Since equation 2.18 is an exact reformulation of the continuous wave equation, it is necessarily stable and non dispersive. When the correction multiplier is greater than unity, then setting it to 1 leaves the higher frequencies at progressively lower amplitudes compared to the lower frequencies. The result is stable but with distortion (an exponential decay), and has a side effect of frequency-dependent wave propagation as shown above. This choice of sampling ($\Delta t \leq \Delta x/v$) is the well-known

time-stepping stability condition, e.g. Lines et al. (1999).

When the correction multiplier is less than unity, then setting it to 1 allows the higher frequencies to reach progressively higher amplitudes compared to the lower frequencies. The result is the exponential growth where the classical von Neumann analysis in (e.g.) Aki and Richards (1980) and Press et al. (1992) predicts the behavior.

A correction factor to prevent instability is given here for a particular case to illustrate the principles involved. The case where $\Delta t = 2\Delta x/v$ is unstable for the uncorrected equation, that is, the time sample rate is twice what it should be for stability. A broadband wavelet was propagated only three steps with these conditions in the uncorrected mode and the results are shown in Figure 2.17. It shows the

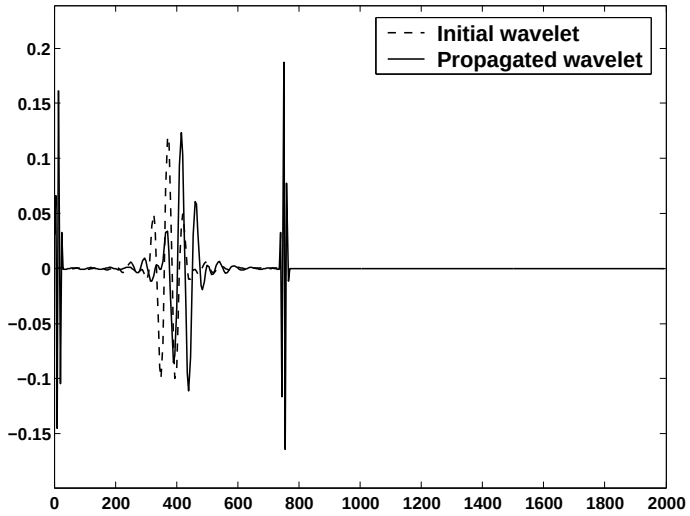

Figure 2.17: A wavelet is shown after 3 propagation steps using equation 2.19 under unstable conditions. The unstable zones appear at the ends of the defined wavelet. These will grow rapidly with each step.

original and propagated wavelets at about 400 metres offset, and typical unstable

artifacts (events which have their highest amplitudes at Nyquist and which grow with each step). The corrected version is shown in Figure 2.18, and the corrections have obviously worked very well after 100 steps.

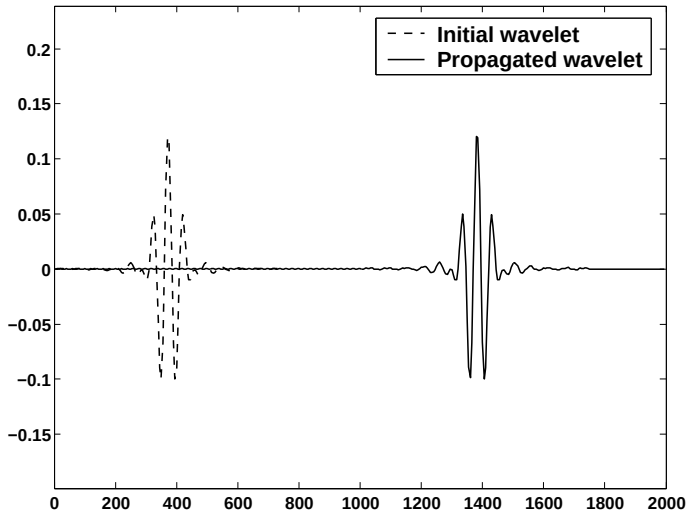

Figure 2.18: The initial conditions here were the same as in Figure 2.17, but 100 steps were taken using the corrected time-stepping equation 2.18.

It is instructive to follow the details of the correction for the $\Delta t = 2\Delta x/v$ case. The squared sinc-function ratio, $sinc^2(kv\Delta t/2)/sinc^2(k\Delta x/2)$, is shown in Figure 2.19, where its amplitude decreases from unity at zero wavenumber to zero at the Nyquist wavenumber. The discrete inverse Fourier transform of this curve is shown in Figure 2.20, and is the very simple spatial operator $(1/4, 1/2, 1/4)$. Since this is the autoconvolution of $(1/2, 1/2)$, the correction is simply a two point running average applied twice. This is a double-dose of the Lax running average which always improves stability (Press et al., 1992). A two point running average and a resample to every-other trace would solve the over-sampling problem, but apparently sufficient averaging by itself can control the high wavenumbers.

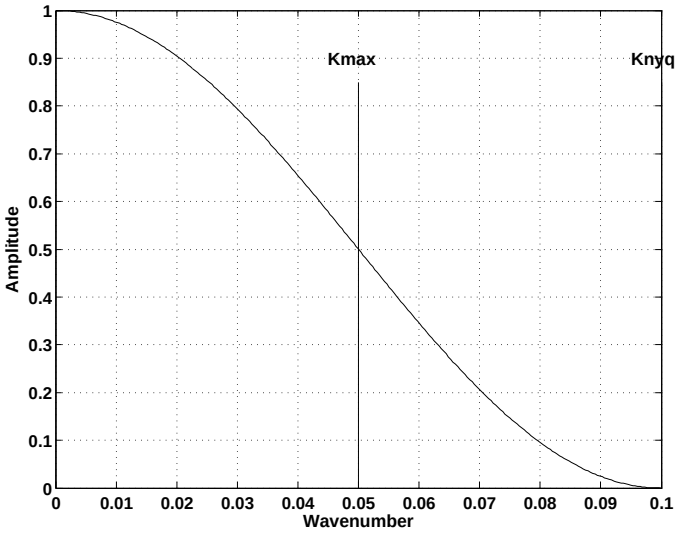

Figure 2.19: The wavenumber correction multiplier which must be used to stabilize for a case where Δt exceeds the stability condition by a factor of two.

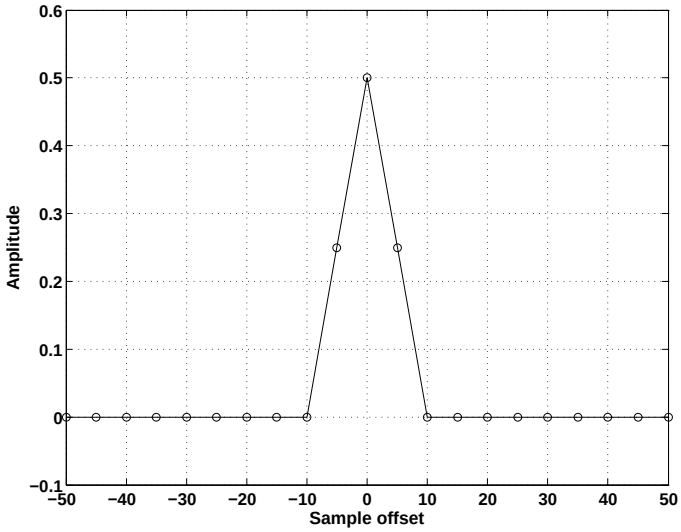

Figure 2.20: The correction filter is shown for the case where Δt exceeds the stability condition by a factor of two. This is the inverse Fourier transform of the spectrum of Figure 2.19

Figure 2.21 shows a suite of correction filters in space for various values of the ratio $v\Delta t/\Delta x$.

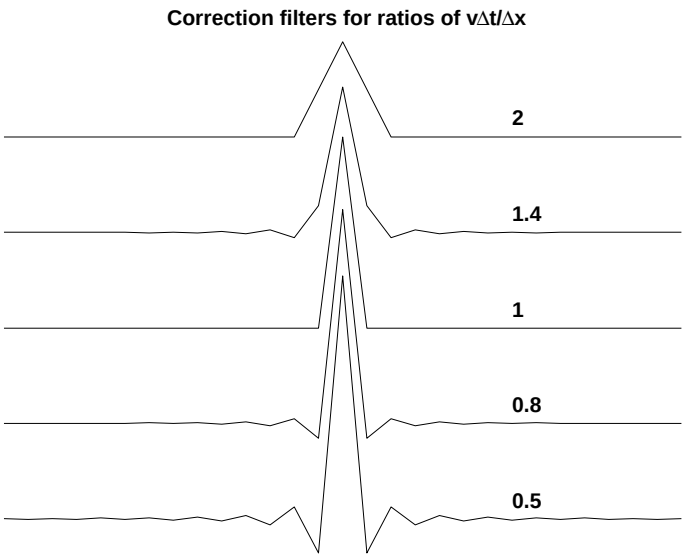

Figure 2.21: Examples of correction filters for the labelled values of $v\Delta t/\Delta x$. The upper two filters are for unstable cases while the lower two are for stable but dispersive cases. The centre filter is a spike for the case which is both stable and nondispersive.

The case just discussed is the uppermost curve where the ratio is exactly 2. In general the filters are infinite in length, although they tend to converge quite rapidly. The filters for unstable cases have an averaging effect, and reduce the high frequency components. The filters for stable but dispersive cases have a deconvolution effect, and enhance the high frequency components. Between these cases is the perfect sampling ratio where the filter is a unit spike.

2.5 New insight into the finite-difference stability condition.

The assessment of requirements in the wavenumber frequency domain may provide more insight into the necessity for the finite-difference time-stepping stability condition. This assessment has not been seen in the literature reviewed to date. The reasoning is suggested by the analysis in the previous section where the supression of the higher wavenumbers makes modelling with larger time sample intervals stable.

The von Neumann stability condition ($\Delta t \leq \Delta x/v$) does not itself provide any intuitive understanding as to why it should hold, and the reason for the asymmetry between the spatial and time sampling is difficult to understand. Some insight is provided by the Courant condition (Press et al. (1992), Figure 19.1.3), where a time step computation is shown as the apex of a pyramid based on a range of spatial values. Here it can be seen that a new displacement calculated for a specific point must have, available for calculation, the whole spatial region from which an event could arrive, given the time elapsed and the material velocity. The key concept within the Courant condition is that, at successive times, displacements described in space are constructed, and the resulting construction in the time or frequency sense can then be validated.

The frequency-domain time-stepping analysis starts with the assumption that the procedure translates wavenumbers (spatial domain) into frequencies (time domain) and not the reverse. Then any procedure must ensure that there are no frequencies generated which would be aliased within the specified time sample rate. The maximum circular frequency (in radians per second) that can be represented at a sample

rate of Δt is given by

$$\omega_{max} = \omega_{Nyquist} = \frac{\pi}{\Delta t} \tag{2.23}$$

The maximum wavenumber which corresponds to this frequency is given by

$$k_{max} = \frac{\omega_{max}}{v} = \frac{\pi}{v\Delta t} \tag{2.24}$$

Since $v\Delta t > \Delta x$ (in the unstable region)

$$k_{max} = \frac{\pi}{v\Delta t} < \frac{\pi}{\Delta x} = k_{Nyquist} \tag{2.25}$$

means that there is a range of possible spatial wavenumbers between k_{max} and $k_{Nyquist}$ which can not propagate because they lack a proper (unaliased) description in time. This in turn means that these wavenumbers, if they exist at all, must be suppressed before they are incorporated into subsequent steps. Note that time domain data is never transformed into space when time-stepping, so under-sampling in the space domain does not cause a stability problem.

Wavenumbers beyond k_{max} can be identified as the 'noise' mentioned in Aki and Richards (1980), and the analysis presented there proved that, with the normal second-order operations, these wavenumbers do not propagate, but rather grow with each step. This corresponds to the von Neumann condition for stability.

A model that is fundamentally unstable (with $\Delta t > \Delta x/v$) can be used if the high wavenumbers are attenuated sufficiently. The wavelet propagated in Figure 2.18 is an example, but the severe attenuation that must be performed with every step is shown in Figure 2.19. Attenuation of this magnitude is practical in a one dimensional model, but becomes much more difficult with a model in two or three dimensions.

2.6 Correction filters

Correction filters are the space domain equivalent of the correction multipliers discussed in previous sections. These filters are the inverse Fourier transforms of the correction multipliers, which were designed in the frequency/wavenumber domain. The filters are convolved with the output of the finite-difference second derivative, and are then followed by the time stepping process. An example of a correction filter has already been developed, and is shown in Figure 2.20. It is the inverse transform of the correction multiplier shown in Figure 2.19, used to control instability.

The advantages of a correction filter are:

1. The forward and inverse Fourier transforms (as in Figure 2.4) are eliminated, saving book-keeping, and often saving computation time.

2. The spatial extent of the filter can be specified, as opposed to frequency domain operators which have essentially infinite spatial requirements.

3. The filters may be designed for regions with unique velocities, and effects from adjacent regions minimized.

The disadvantage of a correction filter is that it is not exact, and it must be designed for optimal performance under certain conditions.

The design and application of correction filters is the subject of the rest of this section. It is at this point where some of the fundamental finite-difference trade-offs must be made: what fraction of the spectral range of zero to Nyquist will be modelled, what filter length will be practical for computer time and at boundaries, and what accuracy is required for the response at each frequency? The design method

described here depends on the first two decisions, and a plot is then made showing the resulting accuracy. Some experiments were done with a more complex spectral selection (e.g. including the Nyquist frequency), but the results were found not to be useful.

It has been found that even quite short correction operators can improve the ordinary second order finite-difference by a large amount. They bring the wavenumber responses much closer to ideal, and therefore give much better simulations of the analytic results. The wavenumbers to be enhanced are chosen from zero to a high value, usually about half the Nyquist wavenumber. It has also been found practical to design these operators within an inherently stable choice of sample rates ($\Delta t \leq \Delta x/v$). This means that generally the higher the wavenumber, the more the amplitudes are enhanced, but wavenumbers above the design top are left attenuated, and the modelling is therefore stable. An example of the ideal wavenumber domain response, and the simulation of the response by a short spatial filter, is shown in Figure 2.26.

The method begins with a one-dimensional discrete Fourier transform in matrix form, shown in Figure 2.22. This is a discrete transform, but the rows are diplayed in analogue form so their nature is more obvious. Only the lower frequency cosine terms are shown. The schematic equation shows how these row samples representing a single frequency are multiplied by the data samples and summed to give the amplitude at each frequency in the transformed vector.

Figure 2.23 shows the case where the data vector is all zeros past a given point. It may also represent the case where, beyond a certain point, the data are unknown and hopefully won't contribute much to the spectrum. In this case a transform may

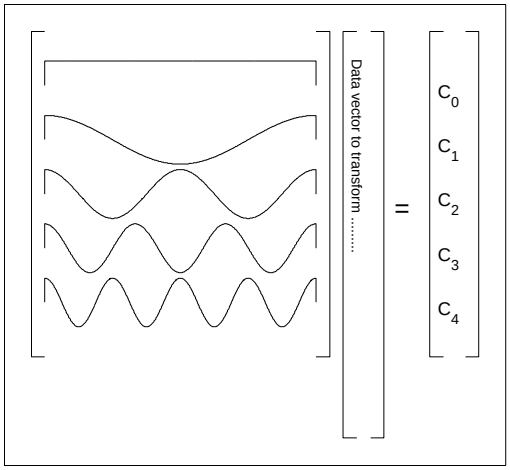

Figure 2.22: First cosine terms of a discrete Fourier transform matrix equation. The transform matrix is discrete but the rows are represented by analogue cosines.

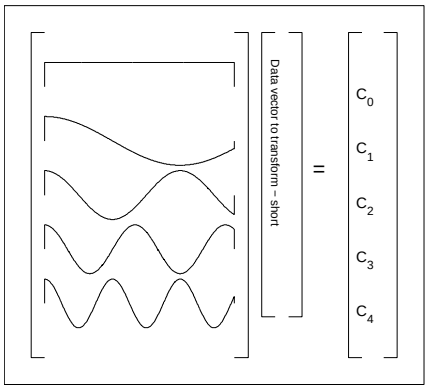

Figure 2.23: First cosine terms of an incomplete discrete Fourier transform matrix equation. The shortened data vector presumably represents the most important frequency components.

still be found, but the cosine terms within the transform matrix may be cut off to the data length, as shown in the figure. The equations represented in Figures 2.22 and 2.23 may be represented in algebraic form by the equation

$$M_{p,j}V_j = S_p \tag{2.26}$$

where $M_{p,j}$ is the Fourier transform operator matrix, V_j is the data vector to be transformed, and S_p is the transformed result. Here the Einstein summation convention over repeated indices is assumed. j ranges from 1 to the data vector length, and p ranges from 1 to the last point of the spectrum.

The case of interest here is shown in Figure 2.24. It is identical to Figure 2.23

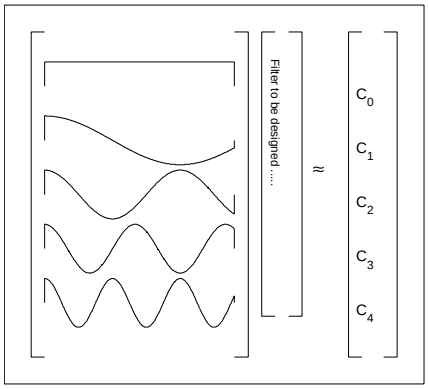

Figure 2.24: The matrix equation similar to Figure 2.23, where the frequency amplitudes are specified and the filter must be designed to approximate them.

except that the frequency response is given, and the data vector is now an unknown filter that will be designed to make the equation work as closely as possible. The matrix equation may be represented by

$$M_{p,j}F_j \approx S_p \tag{2.27}$$

where $M_{p,j}$ is the transform matrix, F_j is the unknown vector or filter, and S_p is the

desired frequency response. A solution for F_j can then be found in a least squares sense by applying standard inverse theory. The solution is given by

$$F_j = (M_{p,j}^T M_{p,j})^{-1} M_{p,j}^T S_p \tag{2.28}$$

where the superscript T indicates transpose and -1 indicates inverse. Note that if the unknown filter is not truncated, the orthogonal rows and columns of the $M_{p,j}$ matrix ensure that the $M_{p,j}^T M_{p,j}$ matrix is the identity matrix, the inverse is also the identity matrix, and the solution is trivial. When the unknown filter is truncated the Fourier components are not orthogonal, and the solution is not trivial.

As an example, the correction filter to accomplish the wavenumber adjustment of equation 2.18 is shown. The desired spectral change is specified for S_p by

$$S_p = \frac{sinc^2(\frac{pv\Delta t}{2})}{sinc^2(\frac{p\Delta x}{2})}, \tag{2.29}$$

and this is substituted into equation 2.28. The resulting correction filter F_j is then used at each time step, by convolving with the complete line of finite-difference derivatives D_x^2. This is accomplished with the standard convolution formula

$$C_k = F_j D_{k+1-j}, \tag{2.30}$$

where C_k is the complete line of corrected second derivatives and D_{k+1-j} is the line of ordinary second-order derivatives D_x^2. The rest of each time step is completed as shown in equation 2.18.

In practice, the matrix equation 2.27 takes a form much closer to that in Figure 2.25. This simulates a short filter length, and a large fraction of the spectrum, usually one-half or three-quarters of the whole spectrum.

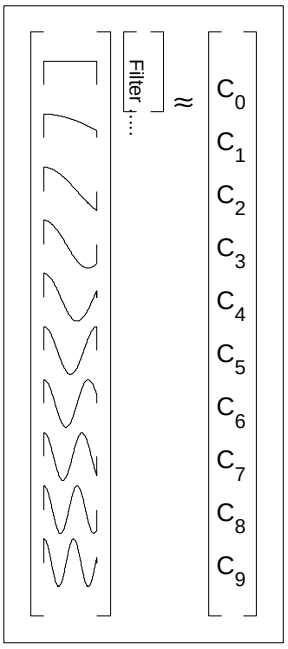

Figure 2.25: The matrix equation identical to Figure 2.24, but with more realistic proportions.

The filter is usually designed to be zero phase, so adjustments must be made to the structure shown in Figure 2.25. In one method, all the transform matrix coefficients are doubled except for those in column 1, those which will be multiplied by C_0. This duplicates the results of convolving with a symmetric zero phase filter. The coefficients obtained will then give the central value and the values from one side. The other side of the filter contains the same coefficients, but in reversed order, and must be added to the beginning of the filter. A more elegant way of designing these filters is shown in Appendix I.

The effectiveness of an optimized spatial filter is most easily estimated in the frequency domain. This is because in the frequency domain the corrections may be specified exactly. A particular case of an optimized short spatial filter is shown in

Figure 2.26, where its frequency response may be compared with the ideal blue curve. Also shown are the actual coefficients of the designed filter. The optimized

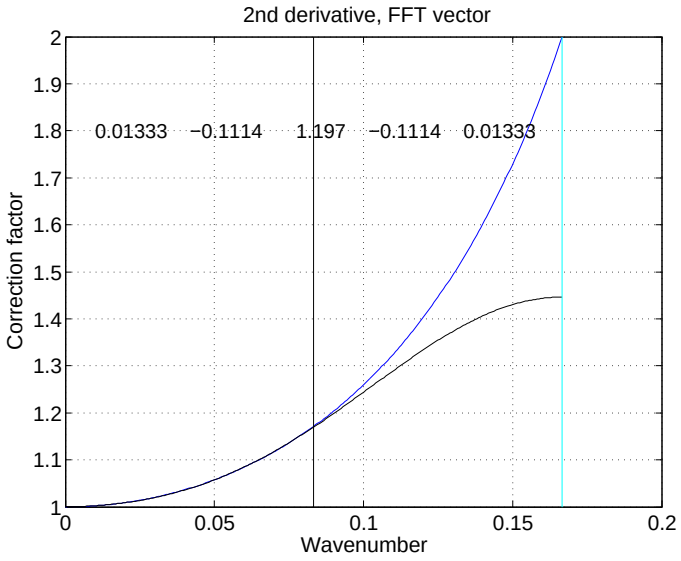

Figure 2.26: The frequency response of an optimized spatial filter and the ideal response in blue. The spatial coefficients appear at the top. Lines at the Nyquist wavenumber (at right) and the top of the design wavenumbers (at half Nyquist) are shown. The parameters are: $v = 1000$ m/sec, $\Delta x = 3$m, and $\Delta t = .0015$ secs.

filter can be seen to match the ideal throughout the design range, from DC to one-half the Nyquist wavenumber.

A second filter was designed with the same parameters as above, except the optimization range was extended up to three-quarters of the Nyquist wavenumber. The quality check of this design is shown in Figure 2.27. The fit with this design is in general not nearly as good, but at the higher wavenumbers the fit is a little better.

The correction filter is most useful in cases where there are several velocities in a model. The same model with two velocities is shown in Figures 2.28, 2.29, and

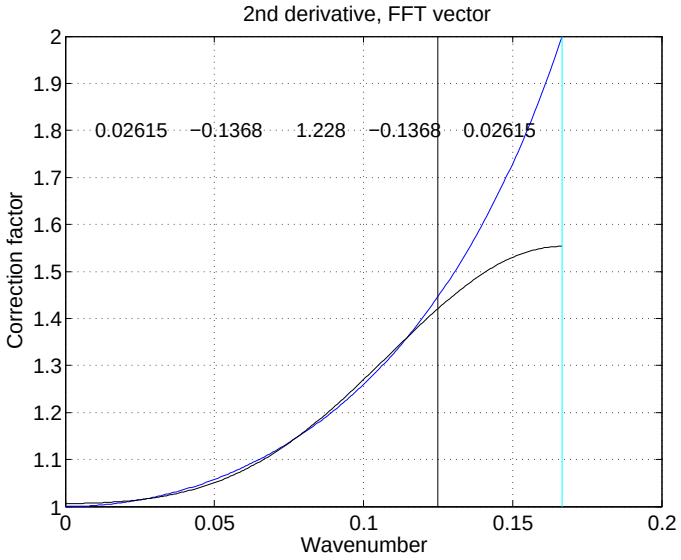

Figure 2.27: The frequency response of a filter designed to fit to three-quarters Nyquist. The other parameters are the same as in Figure 2.26.

2.30, but each figure has had a different treatment of the wave propagation in the lower velocity material to the right.

The wavelet (shown) is initiated to the left of the vertical line, where the velocity is 2000 m/sec., $\Delta x = 3$m, and $\Delta t = .0015$ secs. This constitutes the perfect sampling condition, and in this area no correction is needed or applied. To the right of the vertical line the sample rates are the same, but the velocity is 1000 m/sec., the same parameters used to design the correction filter in Figure 2.26. To the right of the vertical line the designed correction has been applied in Figure 2.29, but not in Figure 2.28. Inspection of the transmitted wavelet in Figure 2.29 shows that its zero phase shape is preserved by the applied correction. By contrast, the uncorrected transmitted wavelet in Figure 2.28 has been severely distorted.

The direct way of improving the response of finite-difference modelling is to reduce

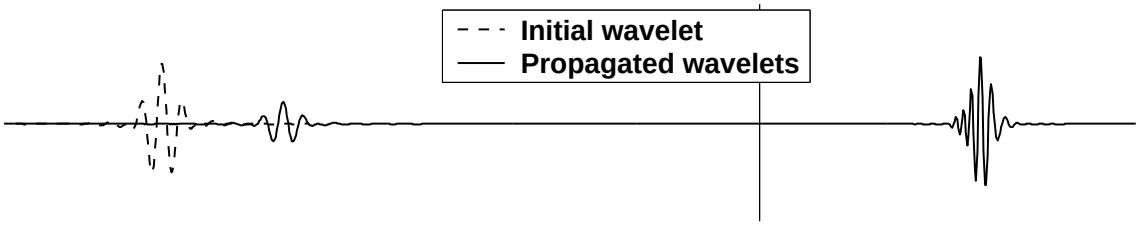

Figure 2.28: The reflected and transmitted wavelets caused by an interface at the vertical line - uncorrected. The right layer has a velocity of one-half that of the left layer.

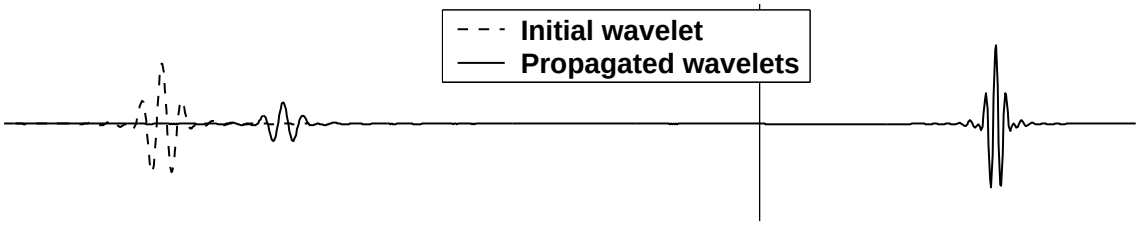

Figure 2.29: The reflected and transmitted wavelets caused by an interface at the vertical line - corrected. The velocities are the same as in Figure 2.28

the spatial and time sampling rates in the same proportions. This method has been applied in Figure 2.30, with the sample rates cut in half and the number of spatial and time samples doubled. Comparison of the finely and coarsely sampled

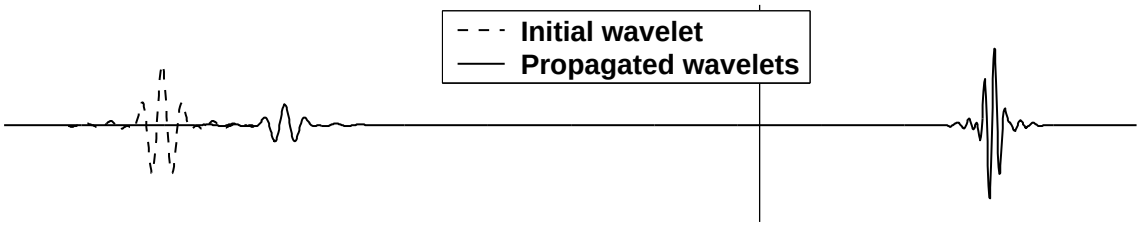

Figure 2.30: The model is the same as in Figure 2.28, but the time and space sample rates have been cut in half.

transmitted waves (Figures 2.30 and 2.28) shows that the finer sampling reduces but does not eliminate dispersion. The corrected version of the transmitted wave in Figure 2.29 is still a much superior result to that in Figure 2.30.

The choice of a wavenumber design window for corrections is determined from the spectrum of the wavelet in space. This in turn is determined from the wavelet spectrum in time and the material velocity. The spatial spectrum of the wavelet used above is plotted in Figure 2.31, which was derived from the zero phase wavelet (20/30-50/60 Hz) and the velocity of 1000 m/sec. The top of the wavelet frequencies may be seen at about .08 cycles/m., within the design window of one-half Nyquist from Figure 2.26.

The operator designed above was applied at a point centered on its output point. This means that near the boundary, the operator convolution used samples from across the boundary, an area with a different velocity. Since the correction filters were designed for a constant velocity environment, the corrections near the boundary were not ideal. On the other hand, the filters were short, so very few convolution

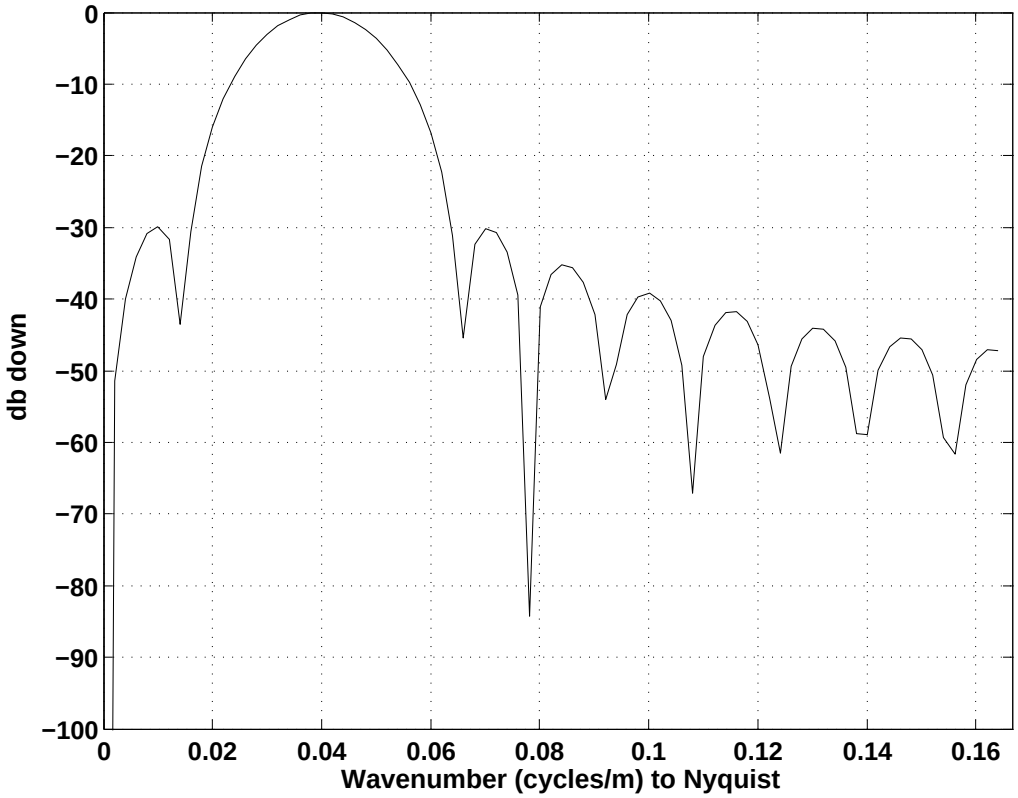

Figure 2.31: Spatial spectrum of the zero phase wavelet translated into wavenumbers at 1000 m/sec. The top of the wavelet frequencies is about .08 cycles/m., within the design window from Figure 2.26.

points were affected by boundaries.

The correction filtering of derivatives was set up as a matrix multiplication for the cases where more than one filter was required. This process is a huge waste of memory and computation time at present, although those drawbacks can be removed with some low level software enhancements. The advantage is that a complex set of corrections can be completely defined for all steps of the model, and then applied as one operation at each time step. The matrix equation is

$$C_k = F_{kj} D_j, \tag{2.31}$$

where C_k is the line of corrected second derivatives and D_j is the line of ordinary derivatives as with equation 2.30, but where F_{kj} is a huge square matrix with each dimension equal to the length of C_k or D_j. The matrix is very sparse (being mostly zeros) and very redundant, having the same filter coefficients repeated through large sections of the matrix. The interesting parts of the matrix are those which operate across the physical boundaries represented along the line. An example is shown in Figure 2.32, where the filters operate across a boundary shown by the red line. The Figure shows that a boundary is assumed to lie directly on a grid point. The f_{1j} filter applies to the left of the boundary, and f_{2j} to the right, the correction being applied at the centre, in this case the 3rd point. The A filter is an average of the two, and applies where there is an equal weight from the two sides of the boundary.

Figure 2.32: Part of a matrix filter at a boundary, indicated by the red line. The f_{1j} filter applies to the left of the boundary, f_{2j} to the right. The correction is applied at the centre, in this case the 3rd point. The A filter is the average of the two f filters.

Chapter 3

Finite-difference elastic wave modelling in two spatial dimensions

Finite-difference modelling in two dimensions has become a very useful tool for seismic applications. It is used to forward model seismic data from a known or possible geological model, usually one that is economically significant. The simulated seismic data may then be used to test the effectiveness of specific acquisition, processing and interpretation methods.

The methods developed here are for what is known as 'elastic' modelling, a more complex and complete model for the solid earth than 'acoustic' modelling. Acoustic models are limited to materials that may be considered to resist deformation by compression only, or materials that are basically fluids. These models are very useful because compressional waves are usually the most important waves transmitted in solids. Elastic models are more truly representative of solid materials, because they also resist shear deformation, and thus can propagate a completely separate type of wave known as a shear wave. Shear waves are interesting for their own properties, but they also interact with compressional waves, and the interchange of energy between the two types of waves can be very significant.

All of the observations and ideas explored above for the one dimensional case also apply, but with much increased complexity, in the two dimensional case. Most of the references mentioned in section 2 are also relevant for two spatial dimensional

modelling. These include Lines et al. (1999), Abramowitz and Stegun (1965), Kreiss and Oliger (1972), Gazdag (1981) and Kosloff and Baysal (1982).

There are many additional references which precede some of the ideas and methods of this thesis. For instance Dablain (1986) used high order spatial operators, and developed an effective method to obtain fourth order accuracy for the second differential in time. Also Holberg (1987) studied how finite-difference operators could be optimized for group velocity and frequency performance in the direction of each axis (for 3-dimensional modelling). This was instead of using the more significant terms of the Taylor series expansion (the classical higher order approach), where "Operators (are) created without physical insight", Holberg (1987) page 636. Later in the thesis these optimizing ideas will be incorporated into the design of small spatial correction filters.

The elastic wave-equation finite-difference solution in two dimensions requires not just a combination of one-dimensional solutions along each axis, but also terms involving combinations of partial derivatives in the two spatial directions. The staggered grid (in space) is particularly suited to this part of the problem, introduced by Madariaga (1976) for polar cordinates. This paper combined the staggered grid with a split of the calculations into two time stages, called the stress step and the velocity step. The staggered grid is even more natural with Cartesian coordinates, and Virieux (1984, 1986) used this grid with stress/velocity splitting, and applied it to interesting exploration cases. The staggered grid is essential to the success of the corrected system given here, although without the stress/velocity or time splitting it is usually associated with. A diagram showing the staggered grid, and the contributions of local x displacements to the z acceleration, will be shown in Figure

3.2.

The following sections will describe a consistent method for analysing the error and stability of finite-difference modelling by direct comparisons to the continuous results. The error found by this method is in the form of a ratio of the calculated to the continuous results, and so the inverse of this error has been called a 'correction multiplier'. This multiplier can be applied to correct second order results, and takes an analytic form in the wavenumber domain.

The method also combines the corrections from the two sides of the wave equation into one, instead of separate corrections for an inaccurate spatial derivative on one side of the equation, and an inaccurate time derivative on the other. The advantage to proceeding in this way is that the two sets of corrections have opposite signs, and only the difference in their effects needs to be applied. Thus the attenuated high frequencies resulting from a second-order spatial derivative can be partially recovered by the inherent inaccuracies of the second-order temporal finite-differencing which tends to enhance the high frequencies. The combined multiplier also takes a compact analytic form in the frequency domain, which can then be transformed and optimized for frequency response and operator length in the time/space domain.

The following six sections will show: the exact results of the two dimensional continuous operators on plane waves, the corresponding finite-difference operators acting on the same waves, the comparisons between the two in the form of 'errors', and the consolidation of the errors to the spatial side of the equation to obtain 'correction multipliers'.

3.1 The continuous wave equation in two spatial dimensions

The two dimensional, continuous, elastic wave equation for a homogeneous, isotropic medium is

$$(\lambda + 2\mu)\frac{\partial^2 U_z}{\partial z^2} + (\lambda + \mu)\frac{\partial^2 U_x}{\partial x \partial z} + \mu\frac{\partial^2 U_z}{\partial x^2} = \rho\frac{\partial^2 U_z}{\partial t^2}, \tag{3.1}$$

which must be paired with an identical equation in which x and z are switched, thus

$$(\lambda + 2\mu)\frac{\partial^2 U_x}{\partial x^2} + (\lambda + \mu)\frac{\partial^2 U_z}{\partial x \partial z} + \mu\frac{\partial^2 U_x}{\partial z^2} = \rho\frac{\partial^2 U_x}{\partial t^2}. \tag{3.2}$$

Here λ and μ are the Lame elastic constants for an isotropic medium, ρ is the density, and U_x and U_z are the horizontal and vertical components of the particle displacement.

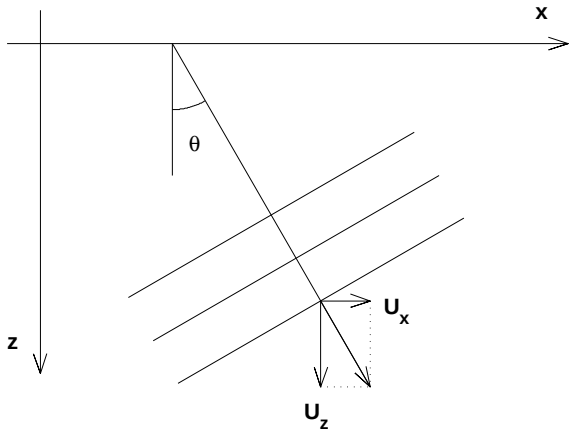

Figure 3.1: A monochromatic pressure plane wave is shown propagating at an angle θ

3.2 The pressure wave continuous solution

A monochromatic compressional plane wave propagating at an angle θ to the z axis is shown in Figure 3.1, and can be represented by the formula

$$\underline{U} = e^{i((zcos\theta + xsin\theta)k - \omega t)}\hat{k},\ \hat{k} = sin\theta\hat{x} + cos\theta\hat{z}, \tag{3.3}$$

where the 'hats' denote unit vectors. This is a compressional wave because the displacement $\hat{k}$ coincides with the propagation direction given in the complex exponential. This is a characteristic property of compressional waves in a homogeneous, isotropic medium. In component notation

$$U_z = cos\theta e^{i((zcos\theta + xsin\theta)k - \omega t)} \tag{3.4}$$

$$U_x = sin\theta e^{i((zcos\theta + xsin\theta)k - \omega t)}. \tag{3.5}$$

For the continuous case, the following partial derivatives of the compressional wave can be calculated

$$\frac{\partial^2 U_z}{\partial z^2} = -cos\theta cos^2\theta k^2 e^{i((zcos\theta + xsin\theta)k - \omega t)}, \tag{3.6}$$

$$\frac{\partial^2 U_z}{\partial x^2} = -cos\theta sin^2\theta k^2 e^{i((zcos\theta + xsin\theta)k - \omega t)}, \tag{3.7}$$

$$\frac{\partial^2 U_x}{\partial x \partial z} = -sin\theta sin\theta cos\theta k^2 e^{i((zcos\theta + xsin\theta)k - \omega t)}, \tag{3.8}$$

$$\frac{\partial^2 U_z}{\partial t^2} = -cos\theta\omega^2 e^{i((zcos\theta + xsin\theta)k - \omega t)}. \tag{3.9}$$

To check that the pair of equations 3.4 and 3.5 are a solution of 3.1, equations 3.6, 3.7, 3.8 and 3.9 can be substituted into 3.1 giving

$$\begin{aligned} & -cos\theta k^2 e^{i((zcos\theta + xsin\theta)k - \omega t)} \left[(\lambda + 2\mu)cos^2\theta + (\lambda + \mu)sin^2\theta + \mu sin^2\theta\right] \\ = \quad & -cos\theta\omega^2\rho e^{i((zcos\theta + xsin\theta)k - \omega t)}. \end{aligned} \tag{3.10}$$

This equation holds if

$$k^2 \left[(\lambda + 2\mu)cos^2\theta + (\lambda + \mu)sin^2\theta + \mu sin^2\theta\right] = \omega^2\rho, \tag{3.11}$$

which rearranges to

$$k^2 \left[(\lambda(cos^2\theta + sin^2\theta) + 2\mu(cos^2\theta + sin^2\theta)\right] = \omega^2\rho, \tag{3.12}$$

and further simplifies to

$$\frac{\lambda + 2\mu}{\rho} = \frac{\omega^2}{k^2} = v_\alpha^2, \tag{3.13}$$

where v_α is the compressional wave velocity.

3.3 The pressure wave finite-difference solution and comparison

In this section, the two dimensional finite-difference operators will be applied to the continuous waveforms, just as the one dimensional finite-difference operators were in section 2.1. These finite-difference operators will use the same notation as the one dimensional operators, with the addition of a subscript to indicate the axis direction in which the derivative is being taken. Thus

$$\frac{\partial^2 U_z}{\partial z^2} \rightarrow D_z^2 U_z, \tag{3.14}$$

etc. The formulae will be very similar to the one dimensional formulae, except for the second term of equation 3.1, which has no analogue there. This second term will depend on the form of the grid.

The most obvious approach for the design of a two dimensional finite-difference grid, and the historical one, is to use a single network of positions in a rectangular

array. Displacements are then vectors positioned at each point of the grid, which may be decomposed into vector pairs oriented in the two perpendicular grid directions, here in the x and z directions. This grid is discussed in appendix D, and shown in Figure D.1. Section D explains how a model using this grid is impossible to 'correct' at Nyquist wavenumbers, and much more difficult to correct at smaller wavenumbers.

It has been found by many modellers, beginning with Madariaga (1976), that more satisfactory results may be obtained by using the staggered grid. This grid is shown in appendix G, Figure G.1. It may also be seen in Figure 3.2, below in this section, where it will be used to set up the correction equations. The displacements, in this case in the directions x and z, are set up on separate grids, displaced one-half a sample spacing from each other in both the x and z directions. This is a satisfactory way to represent a continuous material, and as will be seen, makes the interaction between the two displacement systems (via the cross term) more simple.

When the two equations 3.1 and 3.2 are coded for finite differences, the indexing has subtle changes, but this is just a bookkeeping problem.

To investigate the results of a two-dimensional finite-difference operator, the finite-difference formulae can be applied to the continuous waveforms of equations 3.4 and 3.5. The second derivatives in the direction of the two axes are the same as the one-dimensional form (equation 2.7) so that

$$D_z^2 U_z = \frac{cos\theta}{(\Delta z)^2}\{e^{i\varepsilon(z+\Delta z,x,t)} - 2e^{i\varepsilon(z,x,t)} + e^{i\varepsilon(z-\Delta z,x,t)}\}, \tag{3.15}$$

where ε here is defined by

$$\varepsilon(Z,X,T) = (Zcos\theta + Xsin\theta)k - \omega T. \tag{3.16}$$

The property that

$$e^{\varepsilon(Z_1+Z_2,X_1+X_2,T_1+T_2)} = e^{\varepsilon(Z_1,X_1,T_1)}e^{\varepsilon(Z_2,X_2,T_2)} \tag{3.17}$$

can be used to convert equation 3.15 into

$$D_z^2 U_z = \frac{cos\theta}{(\Delta z)^2} e^{i\varepsilon(z,x,t)}\{e^{i\varepsilon(\Delta z,0,0)} - 2 + e^{i\varepsilon(-\Delta z,0,0)}\}. \tag{3.18}$$

Further algebraic manipulations give

$$D_z^2 U_z = \frac{cos\theta}{(\Delta z)^2} e^{i\varepsilon(z,x,t)} \left(e^{i\varepsilon\left(\frac{\Delta z}{2},0,0\right)} - e^{-i\varepsilon\left(\frac{\Delta z}{2},0,0\right)}\right)^2, \tag{3.19}$$

$$D_z^2 U_z = cos\theta \frac{\left(2isin\left(\frac{k\Delta z}{2}cos\theta\right)\right)^2}{(\Delta z)^2} e^{i\varepsilon(z,x,t)}, \tag{3.20}$$

$$D_z^2 U_z = -k^2 cos^3\theta \frac{sin^2\left(\frac{k\Delta z}{2}cos\theta\right)}{\left(\frac{k\Delta z}{2}cos\theta\right)^2} e^{i\varepsilon(z,x,t)}, \tag{3.21}$$

$$D_z^2 U_z = -k^2 cos^3\theta sinc^2\left(\frac{k_z\Delta z}{2}\right) e^{i((zcos\theta+xsin\theta)k-\omega t)}, \tag{3.22}$$

which uses the form

$$k_z = kcos\theta. \tag{3.23}$$

or the vertical wavenumber.

Equation 3.22 takes the same form as the continuous differential 3.6 but with the extra sinc squared factor, that is

$$D_z^2 U_z = sinc^2\left(\frac{k_z\Delta z}{2}\right)\frac{\partial^2 U_z}{\partial z^2}. \tag{3.24}$$

Similarly it can be shown that

$$D_x^2 U_z = -k^2 cos\theta sin^2\theta \frac{sin^2\left(\frac{k\Delta x}{2}sin\theta\right)}{\left(\frac{k\Delta x}{2}sin\theta\right)^2} e^{i\varepsilon(z,x,t)}, \tag{3.25}$$

$$D_x^2 U_z = -k^2 cos\theta sin^2\theta sinc^2\left(\frac{k_x \Delta x}{2}\right) e^{i((zcos\theta + xsin\theta)k - \omega t)}, \tag{3.26}$$

and

$$D_x^2 U_z = sinc^2\left(\frac{k_x \Delta x}{2}\right) \frac{\partial^2 U_z}{\partial x^2}. \tag{3.27}$$

It should be emphasized that equations 3.24 and 3.27 are true only for a monochromatic plane wave characterized by the wavenumbers k_z and k_x.

Equations 3.24 and 3.27 give the contributions of displacement in the z direction to acceleration in the z direction. The contribution from U_x has no equivalent from the one-dimensional case and so must be developed from first principles. It has single derivatives in both x and z. The staggered-grid representation displaces this x displacement one half of a grid spacing in both x and z, so the output point coincides with the output points for equations 3.24 and 3.27, as shown in Figure 3.2.

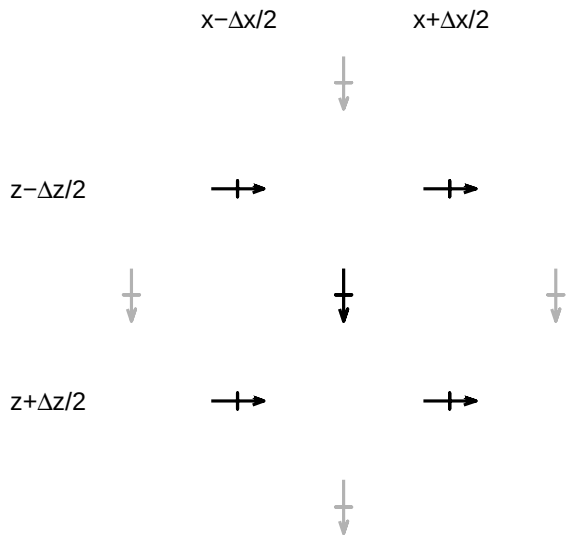

Figure 3.2: The dark arrows show the relative positions of the input and output displacements for the second term of equation 3.1 using the staggered grid. The output z acceleration point is in the centre. The four contributing input x displacements surround it evenly.

The U_x term contribution then takes the following form

$$D_{xz}U_x = \frac{sin\theta}{(\Delta x \Delta z)}\left(e^{i\varepsilon\left(z+\frac{\Delta z}{2},x+\frac{\Delta x}{2},t\right)} - e^{i\varepsilon\left(z+\frac{\Delta z}{2},x-\frac{\Delta x}{2},t\right)} - e^{i\varepsilon\left(z-\frac{\Delta z}{2},x+\frac{\Delta x}{2},t\right)} + e^{i\varepsilon\left(z-\frac{\Delta z}{2},x-\frac{\Delta x}{2},t\right)}\right). \tag{3.28}$$

Algebraic manipulation leads through the following steps

$$D_{xz}U_x = \frac{sin\theta}{(\Delta x \Delta z)}e^{i\varepsilon(z,x,t)}\left(e^{i\varepsilon\left(\frac{\Delta z}{2},\frac{\Delta x}{2},t\right)} - e^{i\varepsilon\left(\frac{\Delta z}{2},-\frac{\Delta x}{2},t\right)} - e^{i\varepsilon\left(-\frac{\Delta z}{2},\frac{\Delta x}{2},t\right)} + e^{i\varepsilon\left(-\frac{\Delta z}{2},-\frac{\Delta x}{2},t\right)}\right), \tag{3.29}$$

$$D_{xz}U_x = \frac{sin\theta}{(\Delta x \Delta z)}e^{i\varepsilon(z,x,t)}\left(e^{i\varepsilon\left(\frac{\Delta z}{2},0,0\right)} - e^{i\varepsilon\left(-\frac{\Delta z}{2},0,0\right)}\right)\left(e^{i\varepsilon\left(0,\frac{\Delta x}{2},0\right)} - e^{i\varepsilon\left(0,-\frac{\Delta x}{2},0\right)}\right), \tag{3.30}$$

$$D_{xz}U_x = sin\theta k^2 sin\theta cos\theta \frac{isin\left(\frac{k\Delta x}{2}sin\theta\right)}{\left(\frac{k\Delta x}{2}sin\theta\right)}\frac{isin\left(\frac{k\Delta z}{2}cos\theta\right)}{\left(\frac{k\Delta z}{2}cos\theta\right)}e^{i\varepsilon(z,x,t)}, \tag{3.31}$$

$$D_{xz}U_x = -k^2 sin^2\theta cos\theta sinc\left(\frac{k_x\Delta x}{2}\right)sinc\left(\frac{k_z\Delta z}{2}\right)e^{i((zcos\theta+xsin\theta)k-\omega t)}. \tag{3.32}$$

Again, this is similar to the continuous derivative (3.8) with the two sinc functions as extra terms, so

$$D_{xz}U_z = sinc\left(\frac{k_x\Delta x}{2}\right)sinc\left(\frac{k_z\Delta z}{2}\right)\frac{\partial^2 U_x}{\partial x \partial z}. \tag{3.33}$$

The time derivative is identical to the one-dimensional case, where

$$D_t^2U_z = -\omega^2 cos\theta \frac{sin^2\left(\frac{\omega\Delta t}{2}\right)}{\left(\frac{\omega\Delta t}{2}\right)^2}e^{i((zcos\theta+xsin\theta)k-\omega t)}, \tag{3.34}$$

$$D_t^2U_z = -\omega^2 cos\theta sinc^2\left(\frac{\omega\Delta t}{2}\right)e^{i((zcos\theta+xsin\theta)k-\omega t)}, \tag{3.35}$$

and

$$D_t^2U_z = sinc^2\left(\frac{\omega\Delta t}{2}\right)\frac{\partial^2 U_z}{\partial t^2}. \tag{3.36}$$

3.4 The shear wave continuous solution

A two-dimensional elastic grid can also be expected to propagate a shear wave, and a monochromatic shear plane wave propagating at an angle θ to the z axis is shown in Figure 3.3, and can be represented by the formula

$$\underline{U} = e^{i((zcos\theta+xsin\theta)k-\omega t)}\hat{k},\ \hat{k} = -cos\theta\hat{x} + sin\theta\hat{z}, \tag{3.37}$$

where the 'hats' denote unit vectors. The z and x components of a possible shear wave (similar to expressions 3.4 and 3.5) are

$$U_z = sin\theta e^{i((zcos\theta+xsin\theta)k-\omega t)}, \tag{3.38}$$

$$U_x = -cos\theta e^{i((zcos\theta+xsin\theta)k-\omega t)}. \tag{3.39}$$

The characteristic property of shear waves in a homogeneous, isotropic medium is what defines these equations. Here the displacement $\hat{k}$ is perpendicular to the propagation direction given in the complex exponential. The negative sign in 3.39 is required to give this displacement, see Figure 3.3. Equally valid would be a displacement in the opposite direction, so care must be taken to keep a consistent relationship between the propagation direction and the displacement. Again, for the continuous case, similar to equations 3.6, 3.7, 3.8 and 3.9, the derivatives are

$$\frac{\partial^2 U_z}{\partial z^2} = -sin\theta cos^2\theta k^2 e^{i((zcos\theta+xsin\theta)k-\omega t)}, \tag{3.40}$$

$$\frac{\partial^2 U_z}{\partial x^2} = -sin\theta sin^2\theta k^2 e^{i((zcos\theta+xsin\theta)k-\omega t)}, \tag{3.41}$$

$$\frac{\partial^2 U_x}{\partial x \partial z} = cos\theta sin\theta cos\theta k^2 e^{i((zcos\theta+xsin\theta)k-\omega t)}, \tag{3.42}$$

$$\frac{\partial^2 U_z}{\partial t^2} = -sin\theta\omega^2 e^{i((zcos\theta+xsin\theta)k-\omega t)}. \tag{3.43}$$

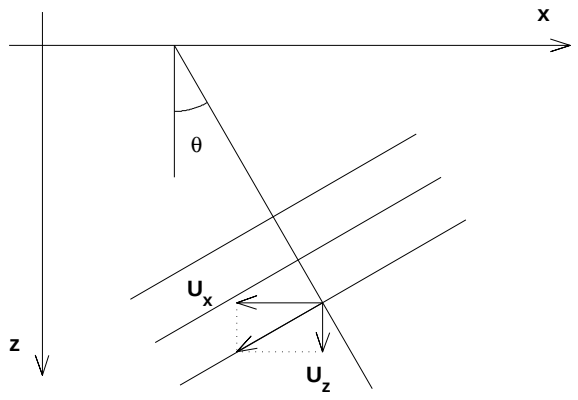

Figure 3.3: A monochromatic shear plane wave is shown propagating at an angle θ. This may be considered a right hand convention, with the displacement to the right when facing in the propagation direction.

These four equations are substituted into 3.1 to get

$$\begin{aligned} & -sin\theta k^2 e^{i((zcos\theta+xsin\theta)k-\omega t)} \left[(\lambda+2\mu)cos^2\theta-(\lambda+\mu)cos^2\theta+\mu sin^2\theta\right] \\ = \quad & -sin\theta\omega^2\rho e^{i((zcos\theta+xsin\theta)k-\omega t)}. \end{aligned} \tag{3.44}$$

This equation holds if

$$k^2\left[(\lambda+2\mu)cos^2\theta-(\lambda+\mu)cos^2\theta+\mu sin^2\theta\right]=\omega^2\rho, \tag{3.45}$$

which manipulates into

$$k^2\left[(\lambda-\lambda)cos^2\theta+(2\mu-\mu)cos^2\theta+\mu sin^2\theta\right]=\omega^2\rho, \tag{3.46}$$

and then simplifies to

$$\frac{\mu}{\rho}=\frac{\omega^2}{k^2}=v_\beta^2, \tag{3.47}$$

where v_β is the shear wave velocity.

3.5 The shear wave finite-difference solution and comparison

Substitution of the shear wave z displacement (equation 3.38) into the finite-difference second derivative formula gives a result almost identical to equation 3.15. It is

$$D_z^2 U_z = \frac{sin\theta}{(\Delta z)^2}\{e^{i\varepsilon(z+\Delta z,x,t)} - 2e^{i\varepsilon(z,x,t)} + e^{i\varepsilon(z-\Delta z,x,t)}\}, \tag{3.48}$$

and further development results in an expression that is similar to 3.22

$$D_z^2 U_z = -k^2 sin\theta cos^2\theta sinc^2\left(\frac{k_z\Delta z}{2}\right) e^{i((zcos\theta+xsin\theta)k-\omega t)}. \tag{3.49}$$

Note that comparison of this finite-difference result and the continuous result (equation 3.40) gives

$$D_z^2 U_z = sinc^2\left(\frac{k_z\Delta z}{2}\right)\frac{\partial^2 U_z}{\partial z^2}, \tag{3.50}$$

which is exactly the same as equation 3.24. Similarly

$$D_x^2 U_z = -k^2 sin^3\theta sinc^2\left(\frac{k_x\Delta x}{2}\right) e^{i((zcos\theta+xsin\theta)k-\omega t)}, \tag{3.51}$$

$$D_{xz} U_x = -k^2 sin\theta cos^2\theta sinc\left(\frac{k_x\Delta x}{2}\right) sinc\left(\frac{k_z\Delta z}{2}\right) e^{i((zcos\theta+xsin\theta)k-\omega t)}, \tag{3.52}$$

$$D_t^2 U_z = -\omega^2 sin\theta sinc^2\left(\frac{\omega\Delta t}{2}\right) e^{i((zcos\theta+xsin\theta)k-\omega t)} \tag{3.53}$$

may be derived. Note that equations 3.24, 3.27 and 3.33 relating the finite-difference and continuous derivatives still apply.

It appears that for pressure and shear waves the continuous equation 3.1 can be represented by the following finite-difference equation

$$(\lambda+2\mu)\frac{D_z^2 U_z}{sinc^2\left(\frac{k_z\Delta z}{2}\right)} + (\lambda+\mu)\frac{D_{xz} U_x}{sinc\left(\frac{k_x\Delta x}{2}\right) sinc\left(\frac{k_z\Delta z}{2}\right)} + \mu\frac{D_x^2 U_z}{sinc^2\left(\frac{k_x\Delta x}{2}\right)} = \rho\frac{D_t^2 U_z}{sinc^2\left(\frac{\omega\Delta t}{2}\right)} \tag{3.54}$$

If spatial derivatives were calculated using the formulae on the left side of this equation, the result would be the same as those calculated by the pseudo spectral approach (as in Kosloff and Baysal (1982)). This is because for the monochromatic case, as here, calculation of derivatives in the frequency domain is exact.

3.6 Inclusion of the acceleration correction term

Note that the left side of equation 3.54 can be fully determined because the complete wavefield in space is available to calculate the spatial wavenumbers in x and z. The sinc correction on the right side of the equation can not be made in a straightforward way because the temporal frequencies are not yet available.

In the one-dimensional case the ω can be determined from the formula $\omega = vk$, as is used in the derivation of equation 2.17 from equation 2.16. This works because there is only one velocity and it can be used to relate the spatial and time frequencies. In the two-dimensional case it can also be expected to work in the case where only one type of wave can propagate.

In the case of a compressional wave travelling in the z direction, the displacement in the x direction is zero, and the variation of the z displacement in the x direction is also zero. The only non-zero terms from equation 3.1 are then the first and last so that

$$(\lambda + 2\mu)\frac{\partial^2 U_z}{\partial z^2} = \rho\frac{\partial^2 U_z}{\partial t^2}. \tag{3.55}$$

Substitution for the continuous derivatives (using equations 3.24 and 3.36) gives

$$(\lambda + 2\mu)\frac{D_z^2 U_z}{sinc^2\left(\frac{k_z \Delta z}{2}\right)} = \rho\frac{D_t^2 U_z}{sinc^2\left(\frac{\omega \Delta t}{2}\right)} = \rho\frac{D_t^2 U_z}{sinc^2\left(\frac{v_\alpha k \Delta t}{2}\right)}. \tag{3.56}$$

So the contribution of the first term of 3.54 must be corrected by the sinc function on the right above, yielding

$$(\lambda + 2\mu)\frac{sinc^2\left(\frac{v_\alpha k\Delta t}{2}\right)}{sinc^2\left(\frac{k_z\Delta z}{2}\right)}D_z^2U_z = \rho D_t^2U_z. \tag{3.57}$$

Similarly, only the third term on the left of equation 3.1 is relevant to a shear wave propagating in the x direction, with the result

$$\mu\frac{sinc^2\left(\frac{v_\beta k\Delta t}{2}\right)}{sinc^2\left(\frac{k_x\Delta x}{2}\right)}D_x^2U_z = \rho D_t^2U_z. \tag{3.58}$$

The factor for the central term on the left side of equation 3.1 was found by inspection, and will be shown to be correct in section 3.7. With this term included, the fully corrected finite-difference version of equation 3.1 is

$$(\lambda + 2\mu)\frac{sinc^2\left(\frac{v_\alpha k\Delta t}{2}\right)}{sinc^2\left(\frac{k_z\Delta z}{2}\right)}D_z^2U_z + \frac{(\lambda + 2\mu)sinc^2\left(\frac{v_\alpha k\Delta t}{2}\right) - \mu sinc^2\left(\frac{v_\beta k\Delta t}{2}\right)}{sinc\left(\frac{k_x\Delta x}{2}\right)sinc\left(\frac{k_z\Delta z}{2}\right)}D_{xz}U_x + \mu\frac{sinc^2\left(\frac{v_\beta k\Delta t}{2}\right)}{sinc^2\left(\frac{k_x\Delta x}{2}\right)}D_x^2U_z = \rho D_t^2U_z. \tag{3.59}$$

The finite-difference version of equation 3.2 may be obtained by replacing each appearance of x in equation 3.59 with z, and replacing each appearance of z in that equation with x. This second equation follows from applying the same replacements used above. The second term on the equation's left hand side remains the same, but the other two terms are unique. The values of each term may be seen in table 3.1.

The result of the calculations in equation 3.59 is the acceleration $D_t^2U_z$. Time stepping is done by decomposing the second-order operator D_t^2 using

$$\frac{U_z(t + \Delta t, ...) - 2U_z(t, ...) + U_z(t - \Delta t, ...)}{(\Delta t)^2} = D_t^2U_z(t, ...), \tag{3.60}$$

Term 1	Term 2a (pressure)	Term 2b (shear)	Term 3
$D_z^2 U_z$	$D_{xz} U_x$	$D_{xz} U_x$	$D_x^2 U_z$
$\frac{sinc^2\left(\frac{v_\alpha k \Delta t}{2}\right)}{sinc^2\left(\frac{k_z \Delta z}{2}\right)}$	$\frac{sinc^2\left(\frac{v_\alpha k \Delta t}{2}\right)}{sinc\left(\frac{k_x \Delta x}{2}\right) sinc\left(\frac{k_z \Delta z}{2}\right)}$	$\frac{sinc^2\left(\frac{v_\beta k \Delta t}{2}\right)}{sinc\left(\frac{k_x \Delta x}{2}\right) sinc\left(\frac{k_z \Delta z}{2}\right)}$	$\frac{sinc^2\left(\frac{v_\beta k \Delta t}{2}\right)}{sinc^2\left(\frac{k_x \Delta x}{2}\right)}$

Table 3.1: The complete suite of correction multipliers which must be applied for the finite-difference U_z acceleration.

Term 4	Term 5a (pressure)	Term 5b (shear)	Term 6
$D_x^2 U_x$	$D_{xz} U_z$	$D_{xz} U_z$	$D_z^2 U_x$
$\frac{sinc^2\left(\frac{v_\alpha k \Delta t}{2}\right)}{sinc^2\left(\frac{k_x \Delta x}{2}\right)}$	$\frac{sinc^2\left(\frac{v_\alpha k \Delta t}{2}\right)}{sinc\left(\frac{k_x \Delta x}{2}\right) sinc\left(\frac{k_z \Delta z}{2}\right)}$	$\frac{sinc^2\left(\frac{v_\beta k \Delta t}{2}\right)}{sinc\left(\frac{k_x \Delta x}{2}\right) sinc\left(\frac{k_z \Delta z}{2}\right)}$	$\frac{sinc^2\left(\frac{v_\beta k \Delta t}{2}\right)}{sinc^2\left(\frac{k_z \Delta z}{2}\right)}$

Table 3.2: The complete suite of correction multipliers which must be applied for the finite-difference U_x acceleration.

as with equation 2.17. This equation is then solved for the advanced time displacement, so that

$$U_z(t + \Delta t, ...) = 2U_z(t, ...) - U_z(t - \Delta t, ...) + (\Delta t)^2 D_t^2 U_z(t, ...). \tag{3.61}$$

This is the solution for the corrected advanced time step of the Z displacement where, again, $D_t^2 U_z(t, ...)$ is given in equation 3.59. A similar equation for the U_x displacement is also required.

Note that these equations have the wavenumber k in the numerator of the correction terms, and the wavenumbers k_z and k_x in the denominator of the correction terms. The relationships between these terms may be illustrated by the use of wave lengths, as illustrated in Figure 3.4. The Figure shows that

$$\lambda_z = \frac{\lambda}{cos\theta} \text{ and } \lambda_x = \frac{\lambda}{sin\theta}. \tag{3.62}$$

Since the wavenumber $k = 1/\lambda$, it follows that

$$k_z = kcos\theta \text{ and } k_x = ksin\theta, \tag{3.63}$$

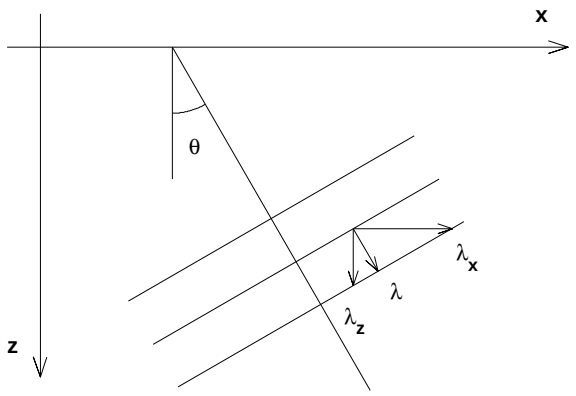

Figure 3.4: Wave length components within a monochromatic plane wave propagating at an angle θ

which is consistent with the definition in formula 3.23

In principle, equation 3.59 is an exact reformulation of the elastic wave equation, but with the restriction that it is valid for a single wavenumber and frequency. No approximations have been made to accommodate finite-differencing. Each term consists of a product of elastic constants, a finite-difference operator, and a ratio of sinc functions. In this document these various sinc function ratios are refered to as 'correction multipliers'. If all the sinc functions are set to unity, then the conventional, second-order, finite-difference elastic wave equation results. If the sinc functions are directly evaluated, they 'correct' the finite-difference calculations for their dispersion and instability. However, the correction multipliers are frequency dependent and so must be applied on Fourier transformed data, or as correction filters in the space domain. These correction factor sinc functions do have zeros, but for a broad range of practical modelling problems it has been found that the effective domain of the correction multipliers lie well within the zeros on each side of the x and z axes. This is supported by the one-dimensional conclusion found in

section 2.1, where Figure 2.2 shows the significant separation between the Nyquist wavenumbers and the zeros.

3.7 Verification of the finite-difference equivalent equation theory

To show that equation 3.59 propagates an analytical pressure wave properly, a wave described by equations 3.4 and 3.5 can be used. Equations 3.22, 3.26, 3.32 and 3.35 describe how the finite-difference operators apply to this wave. The right hand side of these equations may be substituted into equation 3.59. The spatial sinc functions obviously cancel out, and when the factor $\cos\theta e^{i((zcos\theta+xsin\theta)k-\omega t)}$ is divided from both sides, the remaining terms are

$$\begin{aligned} -(\lambda+2\mu)sinc^2\left(\frac{v_\alpha k\Delta t}{2}\right)cos^2\theta k^2 - (\lambda+2\mu)sinc^2\left(\frac{v_\alpha k\Delta t}{2}\right)sin^2\theta k^2 \\ +\mu\, sinc^2\left(\frac{v_\beta k\Delta t}{2}\right)sin^2\theta k^2 - \mu\, sinc^2\left(\frac{v_\beta k\Delta t}{2}\right)sin^2\theta k^2 \\ = -\rho\omega^2 sinc^2\left(\frac{\omega\Delta t}{2}\right). \end{aligned} \quad (3.64)$$

The solution will be correct if this equation holds, and it will hold if

$$(\lambda+2\mu)k^2 sinc^2\left(\frac{v_\alpha k\Delta t}{2}\right) = \rho\omega^2 sinc^2\left(\frac{\omega\Delta t}{2}\right), \quad (3.65)$$

and hold if $v_\alpha = \omega/k$ and $(\lambda+2\mu)/\rho = v_\alpha^2 = \omega^2/k^2$, consistent with the definition of pressure wave velocity. Note that this result is independent of θ, and so it is valid for a pressure wave propagating in any direction.

In a similar fashion, equations 3.38 and 3.39 describe an arbitrary shear wave, and equations 3.49, 3.51, 3.52 and 3.53 describe the results of applying the finite-difference

operators to this wave. This set of consistent equations may also be substituted into equation 3.59. The spatial sinc functions obviously cancel out, and when the factor $\sin\theta e^{i((zcos\theta+xsin\theta)k-\omega t)}$ is divided from both sides, the remaining terms are

$$\begin{aligned} -(\lambda+2\mu)sinc^2\left(\frac{v_\alpha k\Delta t}{2}\right)cos^2\theta k^2 + (\lambda+2\mu)sinc^2\left(\frac{v_\alpha k\Delta t}{2}\right)cos^2\theta k^2 \\ -\mu\, sinc^2\left(\frac{v_\beta k\Delta t}{2}\right)cos^2\theta k^2 - \mu\, sinc^2\left(\frac{v_\beta k\Delta t}{2}\right)sin^2\theta k^2 \\ = -\rho\omega^2 sinc^2\left(\frac{\omega\Delta t}{2}\right). \end{aligned} \quad (3.66)$$

The solution will be correct if this equation holds, and it will hold if

$$\mu k^2 sinc^2\left(\frac{v_\beta k\Delta t}{2}\right) = \rho\omega^2 sinc^2\left(\frac{\omega\Delta t}{2}\right), \quad (3.67)$$

and hold if $v_\beta = \omega/k$ and $\mu/\rho = v_\beta^2 = \omega^2/k^2$, consistent with the definition of shear wave velocity.

This shows that the same pair of finite-difference equations will propagate both pressure and shear waves accurately. Also note that this result is independent of θ, and so is equally accurate in propagation along the grid directions, or at angles in between.

3.8 Further insight into the finite-difference stability condition.

The analysis of the stability criterion in section 2.5 applied to the one-dimensional case. Some may find that the ideas developed here provide further insight into the stability condition for finite-difference modelling in two dimensions. In particular, equation 3.63 may be used to show that a waveform of arbitrary wavenumber k must

obey the formula

$$k^2 = k_x^2 + k_z^2. \tag{3.68}$$

This shows that the maximum wavenumber that can be represented in a one-dimensional sense ($k = \pi/\Delta t$) is no longer the maximum if the wave is not aligned with an axis. The maximum wavenumber in a two-dimensional sense is given by a wave characterized as having the Nyquist wavenumber in both x and z, so that

$$k_{max}^2 = k_{xNyq}^2 + k_{zNyq}^2. \tag{3.69}$$

If the sample rates in x and z are the same, the maximum is given by

$$k_{max}^2 = 2k_{Nyq}^2, \tag{3.70}$$

and

$$k_{max} = \sqrt{2}k_{Nyq}. \tag{3.71}$$

Then stability requires that

$$\omega_{max} > v\, k_{max} = v\sqrt{2}k_{Nyq}, \tag{3.72}$$

and the one-dimensional stability condition ($\Delta t < \Delta x/v$) must be modified to

$$\Delta t < \Delta x/(v\sqrt{2}). \tag{3.73}$$

This is consistent with the criterion specified for second order modelling in (for example) Lines et al. (1999).

3.9 Application of corrections in the frequency domain

It has been found that the most practical way to use frequency domain corrections in modelling is to start with inherently stable parameters, as given by equation 3.73.

The corrections have been found to be very useful to reduce the amount of numerical dispersion, especially in the direction of the axes, and in lower velocity areas.

The method described here has been tested by a straightforward Fourier domain approach. For each acceleration component (for U_z and U_x), the result of each of the three finite-difference terms were transformed into the Fourier domain and multiplied by the appropriate wavenumber surface. The components were then added together and inverse transformed for use in time stepping. Thus the correction factors were applied after each time step. The processing flow is illustrated in Figure 3.5.

An example of a wavenumber correction surface for the first term in equation 3.59 is shown in Figure 3.6. This is the $D_z^2 U_z$ term. The Figure shows that a model with the specified parameters must have the amplitudes of the higher wavenumbers in z increased, and of the higher wavenumbers in x decreased.

The correction surface for the third term ($D_x^2 U_z$), for a model with the same parameters, is shown in Figure 3.7. Here it is the high x wavenumbers that must be amplified, and the z wavenumbers slightly attenuated.

The value of applying correction multipliers may be seen in the comparison of uncorrected and corrected models. One of the best tests of a modelling method consists of waves in the form of a ring propagating outwards. These rings show propagation at all angles and have no edge effects. Figure 3.8 shows a 30 Hz zero phase P-wave initiated as a ring in the centre of the model and propagated through 120 time steps. It would be considered undersampled for conventional modelling, although all frequencies in the wavelet are well below the Nyquist frequency. Figure 3.9 shows a P-wave initiated in the same manner as in Figure 3.8, but propagated with a correction multiplier at each time step. The propagated wave, with its circular

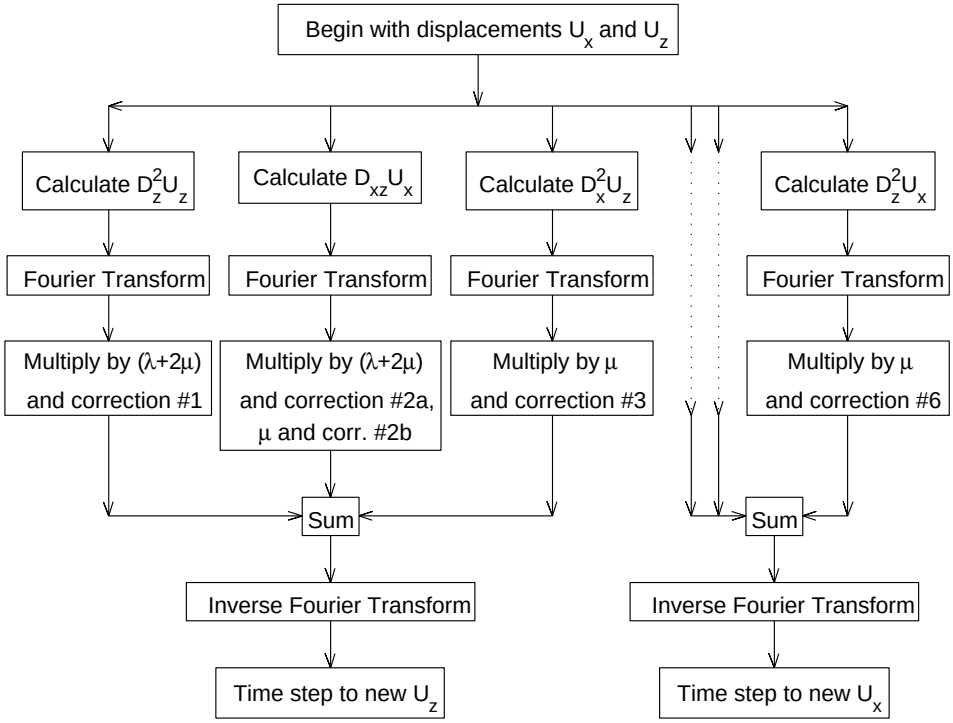

Figure 3.5: The flow chart for application of the correction multipliers in the frequency domain. The correction numbers are defined in Tables 3.1 and 3.2. The fourth and fifth processing sequences were abbreviated to save space.

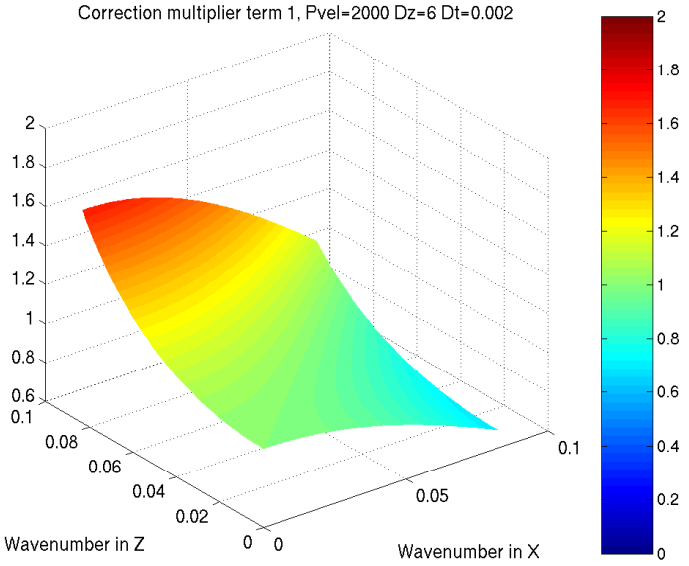

Figure 3.6: An example of a correction multiplier for the first ($D_z^2 U_z$) term in the wavenumber domain. A model with this particular set of parameters (for velocity, Δx and Δt) requires the amplitudes of the higher wavenumbers in z to be increased, and the higher wavenumbers in x to be attenuated.

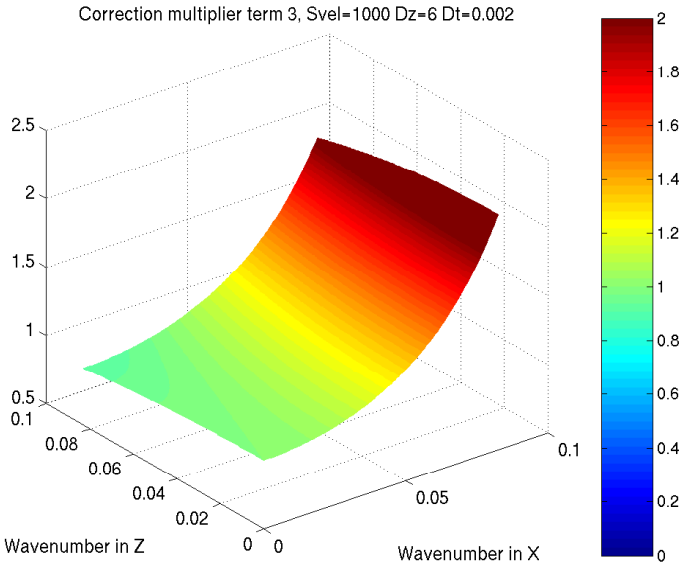

Figure 3.7: An example of a correction multiplier for the third ($D_x^2 U_z$) term in the wavenumber domain. Here, the higher wavenumbers in x must have their amplitudes increased, and the higher wavenumbers in z slightly decreased.

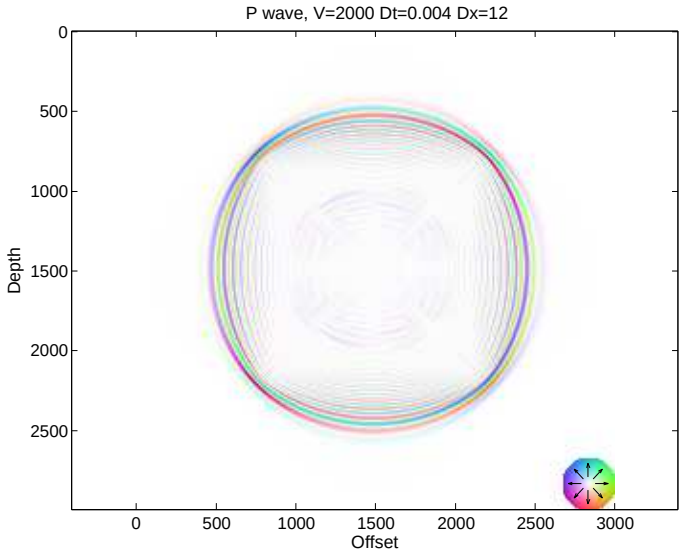

Figure 3.8: An uncorrected P-wave is shown after propagation through 120 time steps. Note the 'square' shape to the dispersion pattern within the wavefront. The legend showing how displacement direction is represented by colour is described in section F, and Figure F.1.

shape and preserved zero phase character, is much closer to what would be expected from an analytic solution. The square like shape of uncorrected propagation is a flaw which has been directly addressed in Cole (1994).

A second example is a combination of two cylindrical waves, one a pressure wave and the other a shear wave. The shear wave ring is necessary to complete the testing of the elastic wave equation. The waves are initiated by defining them at two times separated by an interval equal to the time sample rate. The wave as defined at time zero is plotted in Figure 3.10 as vector displacements, and in Figure 3.11 with colour coding.

The uncorrected model is shown after propagation through 120 steps in Figure 3.12. The P-wave ring may be compared to that in Figure 3.8. Here the propagation

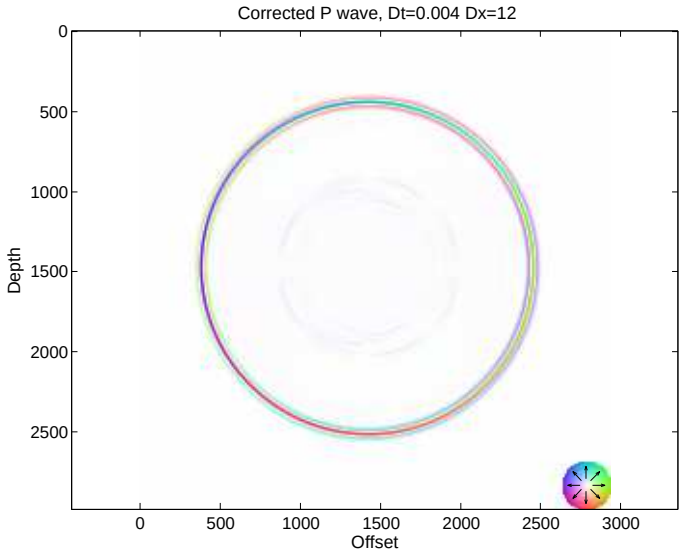

Figure 3.9: A P-wave is shown after propagation with higher frequencies enhanced by correction multipliers at each time step. The circular form of the wavefront, and the zero phase character of the wavelet, are both preserved.

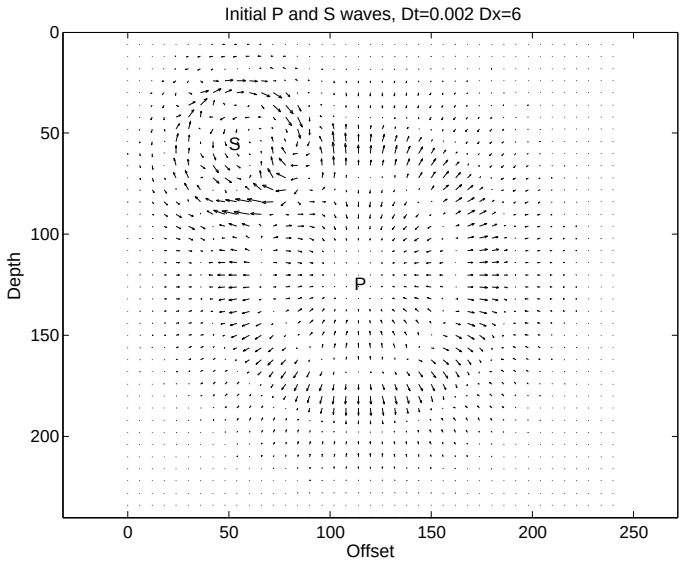

Figure 3.10: The initial P and S wave rings about to be propagated outward are shown in detail as displacement vectors. The centre of the S-wave ring is marked at upper left. The displacements of the P-wave ring at lower right are added to the S-wave displacements.

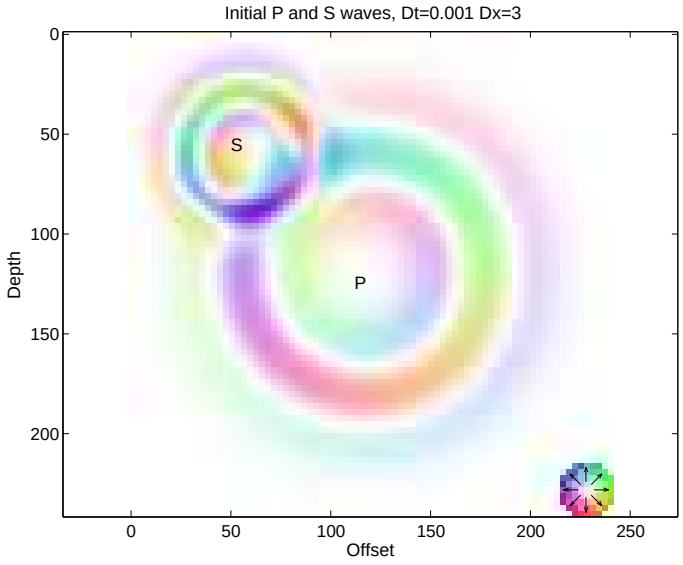

Figure 3.11: The initial P and S wave rings in detail in colour format. This is identical to Figure 3.10.

has preserved the wave much more successfully, as a result of the halved sample rate in space and time, and because the distance propagated has been halved. The S-wave here is distorted, even at these finer sample rates, showing that S-wave propagation is a more rigorous test for a modelling system.

The corrected model in Figure 3.13 shows a most notable improvement in the S-wave, and also preserves the zero phase character of the P-wave.

The improvement to be gained by the straightforward technique of finer sampling is employed with the model in Figure 3.14. It has almost perfect P-wave propagation, but leaves the S-wave with an unbalanced appearance.

Another method of evaluating these results is by comparing individual traces from the models. Figure 3.15 and Figure 3.16 are traces extracted from the raw and corrected models in Figures 3.12 and 3.13. The preserved zero phase nature of the

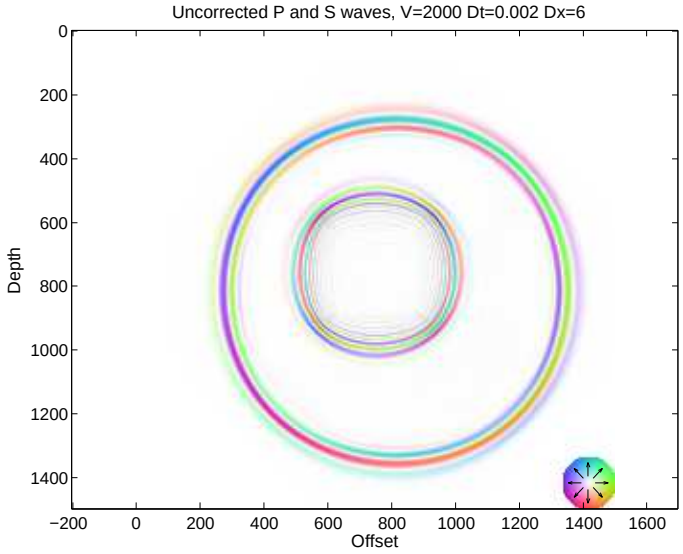

Figure 3.12: The uncorrected model propagated 120 steps from Figure 3.11 is shown. Note that the scale has changed. The finer sample rate in space and time compared with Figure 3.8 has allowed the P-wave to propagate quite evenly, but the S-wave remains distorted.

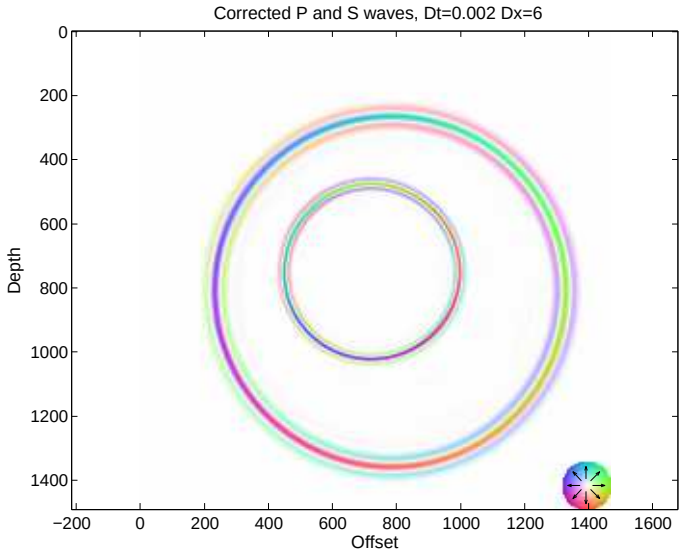

Figure 3.13: This shows the model propagated from Figure 3.11, but with corrections. The S-wave has retained its circular shape, and both waves have retained their zero phase character.

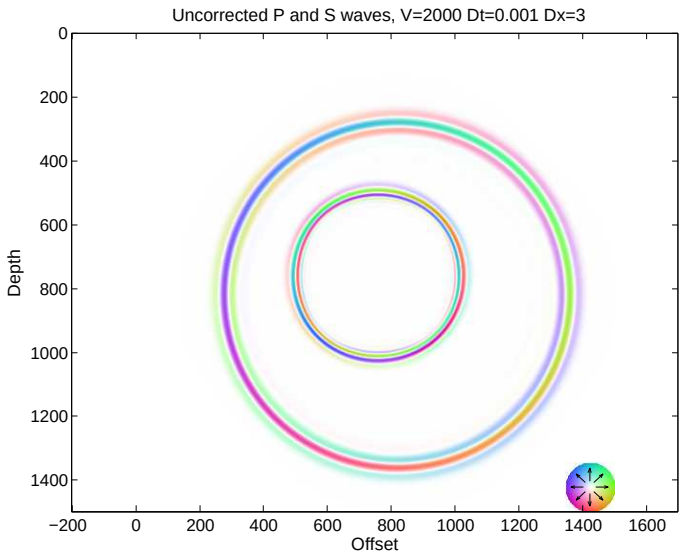

Figure 3.14: The uncorrected model propagated 240 steps with the spatial and time sample rates halved. The scale here is the same as in Figure 3.12. The finer sample rates have corrected the phase of the P-wave, but the S-wave phase is incorrect.

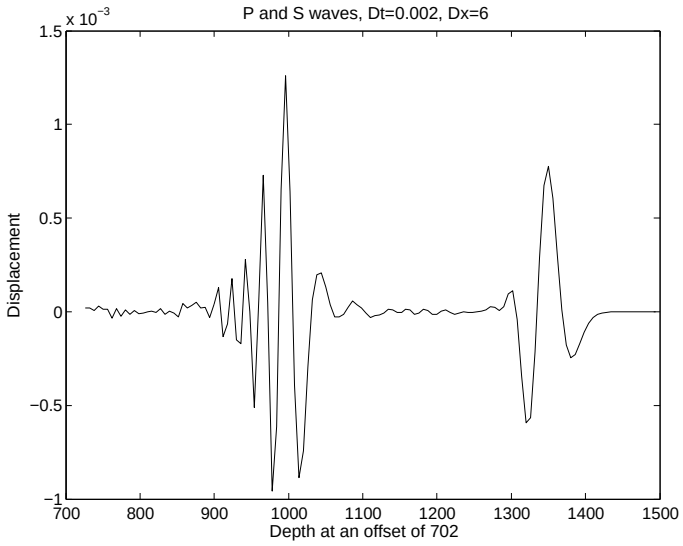

Figure 3.15: The uncorrected S-wave (left) and P-wave (right) are shown in a trace from Figure 3.12. The S-wave has been badly distorted and the P-wave has been phase shifted.

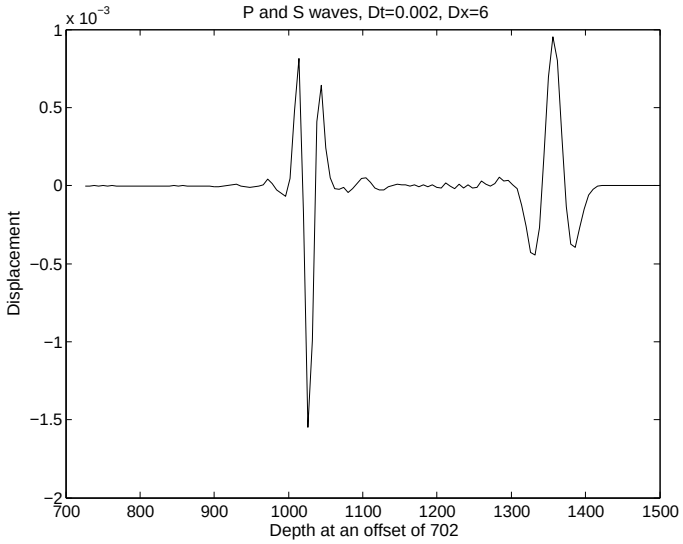

Figure 3.16: The corrected S-wave (left) and P-wave (right) are shown in a trace from Figure 3.13. Both S and P waves are zero phase.

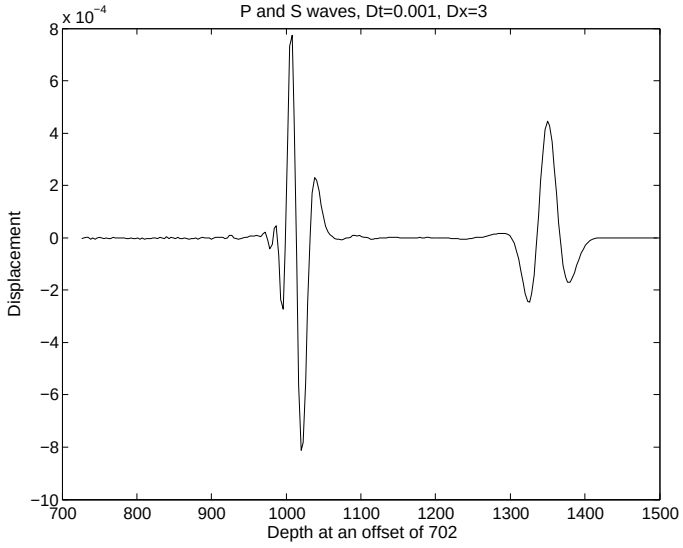

Figure 3.17: The finer sampling has corrected the phase of the P-wave (right) but the S-wave (left) is still not zero phase.

pressure and shear waves is very obvious in the extracted trace (Figure 3.16) from the corrected model from Figure 3.13. The straightforward method of improving modelling results, halving the sample rates and doubling the number of spatial and time samples, has essentially fixed the P-wave, and has improved but not completely corrected the S-wave. For this example, the corrected model required 50 percent more computer time, and the finely sampled model more than 400 percent more computer time. In all experiments, the 'correction' route has been found to be more effective than halving the sample rates in x, z and t. This difference shows up earlier for S-waves, but must appear eventually with P-waves if they are propagated far enough. The doubling of the number of samples required has also been found to require more computer time.

Chapter 4

Optimised correction filters for modelling in two dimensions

Correction filters are the space domain equivalent of the correction multipliers discussed in previous sections. This section extends the design principles from the one-dimensional case in section 2.6 to two dimensions. The same reasons, advantages, disadvantages, and design philosophy apply. Again, just as in section 2.6, choices must be made among some of the fundamental finite-difference alternatives: what fraction of the spectral range of zero to Nyquist will be modelled, what filter sizes will be practical for computer time and at boundaries, and what accuracy is required for the response at each frequency? The same type of matrix equations will be used, and will be compared to the corresponding equations in the one-dimensional case.

There will also be comparisons made to a particular style of corrections, fourth order in space with a finer (than usual) time sample rate (Levander, 1988).

4.1 Optimum spatial design in two dimensions

The two-dimensional Fourier transform operates, in this case, on a function with the independent variables x and z, and transforms it into a function with the independent variables specified as the k_x and k_z wavenumbers. For sampled data, a four

dimensional matrix may be set up to do this transform as

$$M_{k_x,k_z,x,z} A_{x,z} = S_{k_x,k_z}, \tag{4.1}$$

where M is the Fourier transform operator matrix, A is the two dimensional function to be transformed, and S is the spectrum, or transformed result. At this point, k_x and k_z can be assumed to be arbitrary wavenumbers in x and z. The analagous relationship in one dimension is equation 2.26.

Figure 4.1 shows a matrix diagram which emphasizes the discrete Fourier transform nature of equation 4.1, here used to obtain a few of the lower frequency Fourier coefficients. The four dimensional transform matrix has been specified here as the

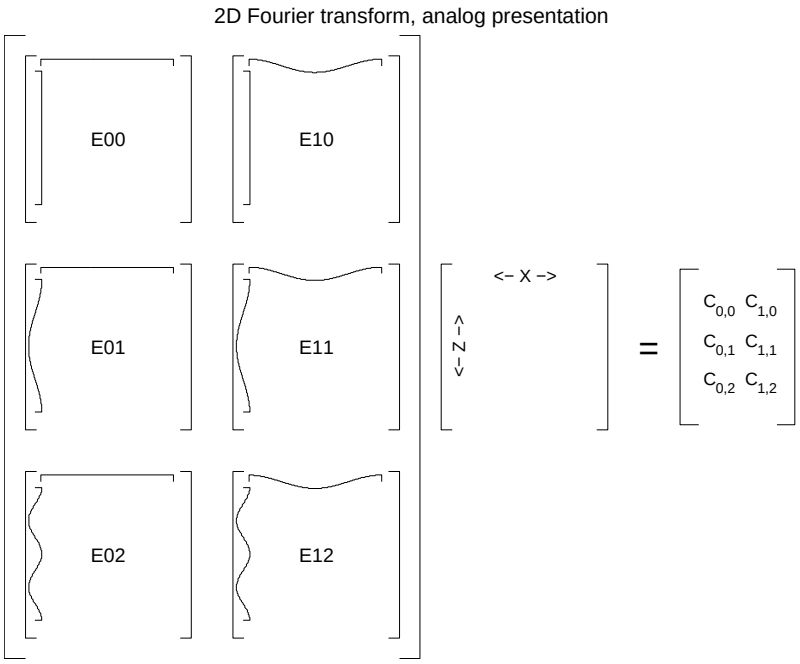

Figure 4.1: First cosine terms of a 4D transform matrix in an equation to do 2D Fourier transforms. Each sub matrix is characterized by the frequencies along its edges. The transform matrix is discrete but the edge frequencies are represented by analogue cosines.

matrix of matrices shown on the left. Next to it is the input 2 dimensional spatial data set, and to the right of the equal sign is the output spectrum. The transform is done by overlaying each elementary Fourier component matrix (within the super matrix on the left) on the data matrix and multiplying (element by element) and summing to obtain a single output cosine term within the matrix on the right side of the equation. Each elementary matrix is labelled by the frequency (in cycles per data length) in the x and z directions, and may also be identified by the analogue (cosine) traces along the top and left side. This might be called a pseudo matrix equation because each sub matrix acts like a row in the equation in Figure 2.22.

The equivalent 2D Fourier transform for the cosine amplitude $C_{l,m}$ is given by

$$E_{l,m,p,q}A_{p,q} = C_{l,m}, \tag{4.2}$$

where

$$E_{l,m,p,q} = \left[cos(2\pi lp/n_x)cos(2\pi mq/n_z)\right], \tag{4.3}$$

the two-dimensional function of the cosines multiplied together, where $p = 1 : n_x$ and $q = 1 : n_z$. Assuming that the maximum wavenumber required in the x and z directions are the same k_{max}, then l and m each range independently from 1 to k_{max}. These are constructed and then multiplied against the sampled function in space A, and all these results summed.

The above transform expressions have described only cosines, but the same principles apply to general transforms. Only cosines were displayed for the following reasons:

- Restricting the display to cosines reduces 'complexity', so the principles are more obvious.

- Zero phase processes or filters may be naturally described using only cosines.
- Use of zero phase symmetry saves memory and computation time.

Figure 4.2 shows the partial 2D Fourier transform, analogous to Figure 2.23. This demonstrates the case where the function (or filter) is limited in size. In practice these elementary matrices will be small, in the symmetric case perhaps as small as 3x3, which represents a final filter size of 5x5. The number of these small matrices may be large, perhaps containing wavenumbers up to half of Nyquist, although each wavenumber is represented by only its leading samples (in the case mentioned, only the leading 3 samples).

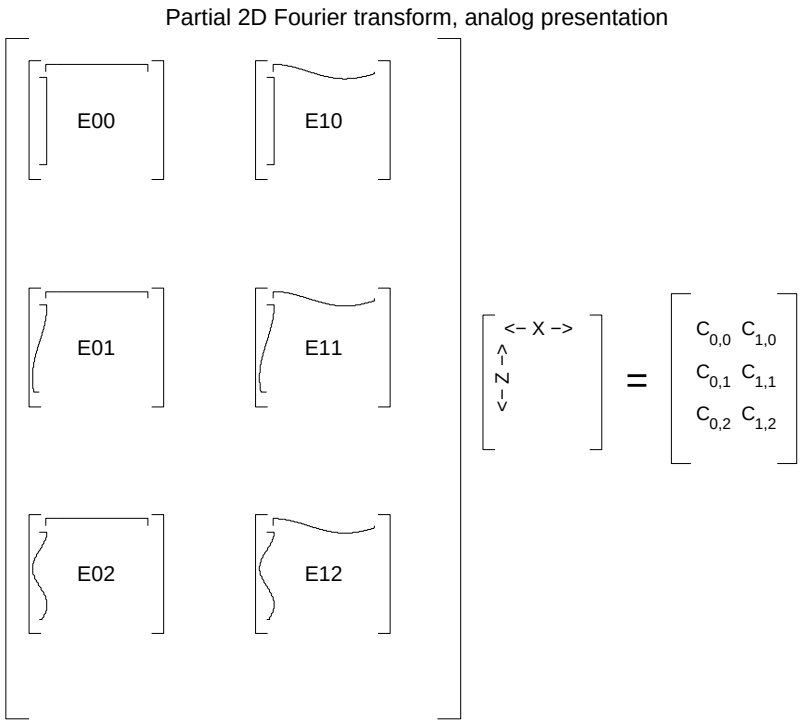

Figure 4.2: Two dimensional Fourier transform of a partial (length and width reduced) function.

Figures 4.3 and 4.4 show the steps taken to reform the 4D matrices into standard

2D matrices. Figure 4.3 shows the stage where the elementary Fourier matrices have been resized into long row vectors, and the function has been resized into a long column vector. This reshaping is legitimate as long as it is done consistently, forcing the same pairs of numbers to be multiplied together, and adding to the same sum.

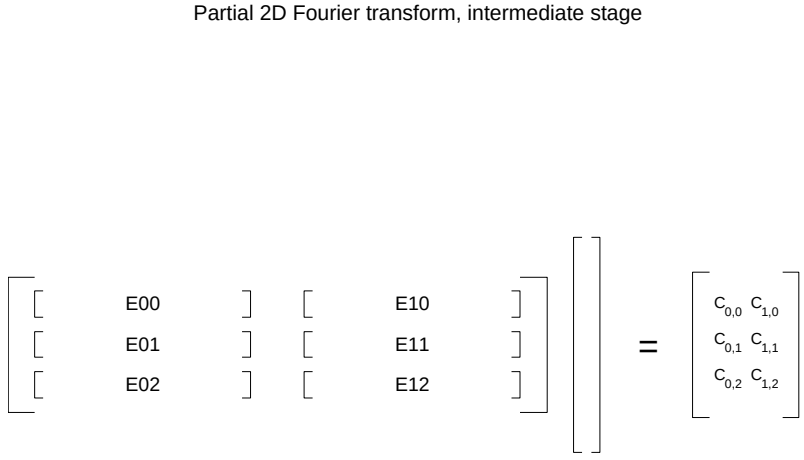

Figure 4.3: an equivalent version of the equation shown in Figure 2.23, with the elementary matrices reformed into rows, and the function into a column.

Figure 4.4 shows how the matrices have been resized into a standard matrix equation format. At the same time, analogous to the difference between equations in Figures 2.23 and 2.24, the equal sign has been changed into an approximation sign to indicate that the column vector on the right is the known (desired) response, and the column vector which is part of the matrix multiplication is the unknown filter. This fits the format of equation 2.27, which has a solution for F_j given by equation 2.28. This solution is a vector which may be resized in reverse fashion into a 2D filter with a least squares optimal frequency response.

In practice, the elementary matrices shown in analogue form are modified slightly

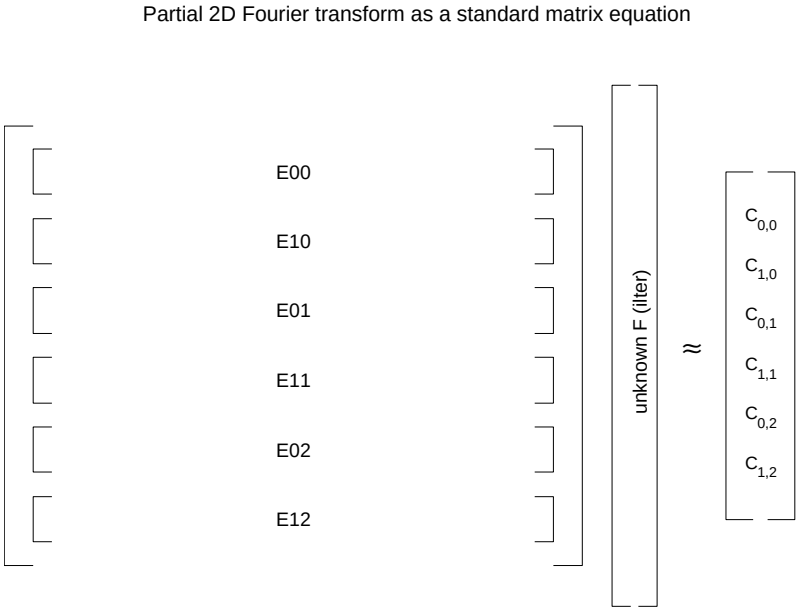

Figure 4.4: Here the equation from Figure 4.3 has the elementary matrices reformed into separate rows, and the output amplitudes reformed into one column. It is in the form of equation 2.27 and therefore the unknown F has a solution given by equation 2.28.

to represent the analysis of a two dimensional filter that is zero phase in both the x and z directions. The Fourier components may be obtained from little more than one quarter of the coefficients in a filter of this type, and they are guaranteed to all be cosines because of the symmetry of the correction filters. However, the coefficient matrices must be modified to allow for the duplicated samples in the other three quadrants.

The modifications are of the same nature as those given for the one dimensional case in section 2.6. Most of the transform matrix coefficients are multiplied by 4 except for those on the inside edges, which are multiplied by 2 except for the central value, which is multiplied by 1. The complete filter is then reconstructed by flipping and adding the one calculated quadrant into the other three quadrants.

4.2 Examples of optimized correction filters in two dimensions

Correction filters are applied within the second-order finite-difference calculations in the places marked in the flow chart of Figure 4.5. This flow chart is similar to the one for correction multipliers in Figure 3.5, the differences being that here there are no Fourier transforms, and the correction operations are convolutions instead of multiplications.

The examples shown here will have the same parameters as were used for some of the frequency domain corrections in section 3.9. The pressure and shear wave velocities are 2000 and 1000 m/sec respectively, the spatial sample rate is 6 m and the time sample rate is .002 seconds. The initial wave forms are the combination of

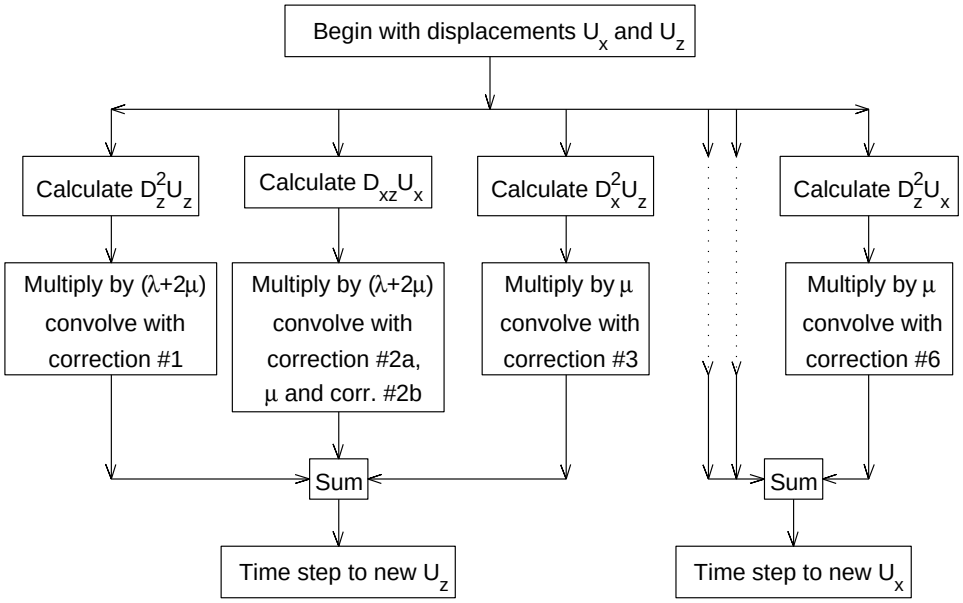

Figure 4.5: The flow chart for convolution of the correction filters. The correction filter numbers are defined in Tables 3.1 and 3.2. The fourth and fifth processing sequences were abbreviated to save space.

pressure and shear energy shown in Figures 3.10 and 3.11.

The correction multiplier plots in wavenumber will be shown as contours for easier comparison between the different methods. The 3D plots in Figures 3.6 and 3.7 are useful for showing the relative amplitudes within a correction, but are not as useful for comparing corrections.

The ideal wavenumber domain response of the correction multipliers for 3 terms of a model with the chosen example parameters are given in Figures 4.6, 4.8 and 4.10. The corresponding wavenumber domain responses of a practical set of small

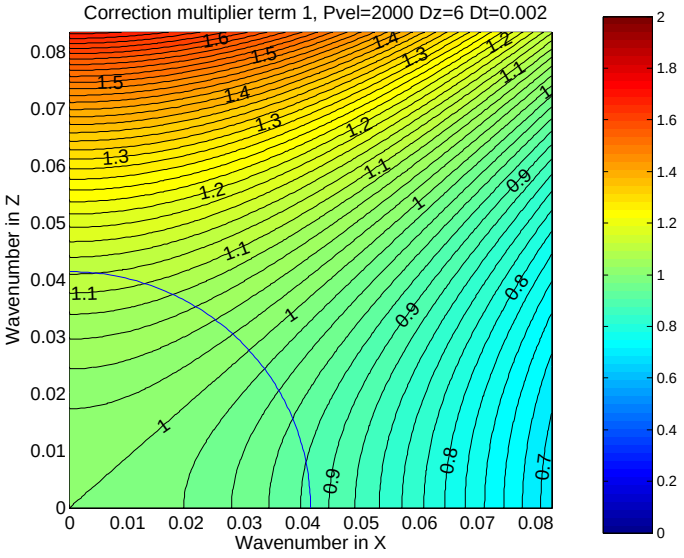

Figure 4.6: The Fourier domain response of the ideal correction multiplier for term number 1.

correction filters is shown in Figures 4.7, 4.9 and 4.11. They are all 5 points by 5 points in size, designed on the wavenumbers ranging from zero to one-half Nyquist. This zone is marked roughly by a quarter circle centered on wavenumbers (0,0), with a radius extending to one-half of the Nyquist wavenumber. A similar quarter circle is also marked on the ideal plots, for comparison.

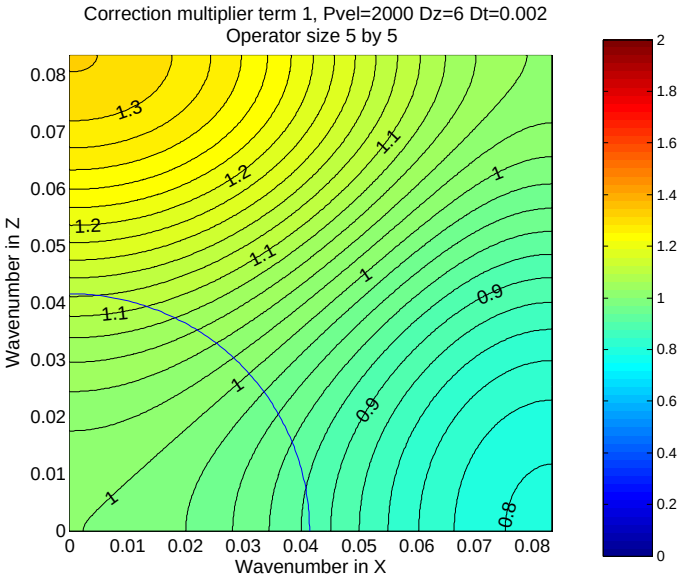

Figure 4.7: The Fourier domain contour plot of the 5 by 5 correction filter (in wavenumbers) for term number 1. Compare with the ideal corrections in Figure 4.6

	x_1	x_2	x_3	x_4	x_5
z_1	-0.0000	0.0006	0.0082	0.0006	-0.0000
z_2	0.0004	-0.0048	-0.0714	-0.0048	0.0004
z_3	-0.0046	0.0602	1.0310	0.0602	-0.0046
z_4	-0.0004	-0.0048	-0.0714	-0.0048	0.0004
z_5	-0.0000	0.0006	0.0082	0.0006	-0.0000

Table 4.1: Correction filter coefficients for term 1. A deconvolution effect may be seen in the z direction, and a smoothing effect in the x direction.

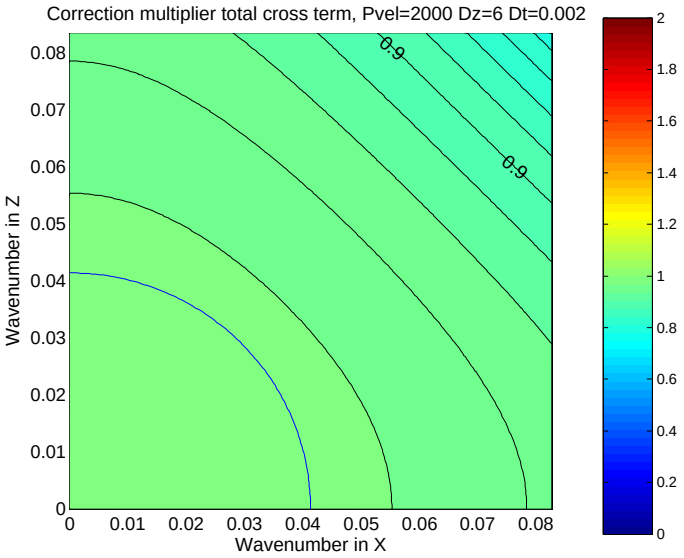

Figure 4.8: The Fourier domain contour plot of the ideal correction multiplier for the combination of terms 2a and 2b.

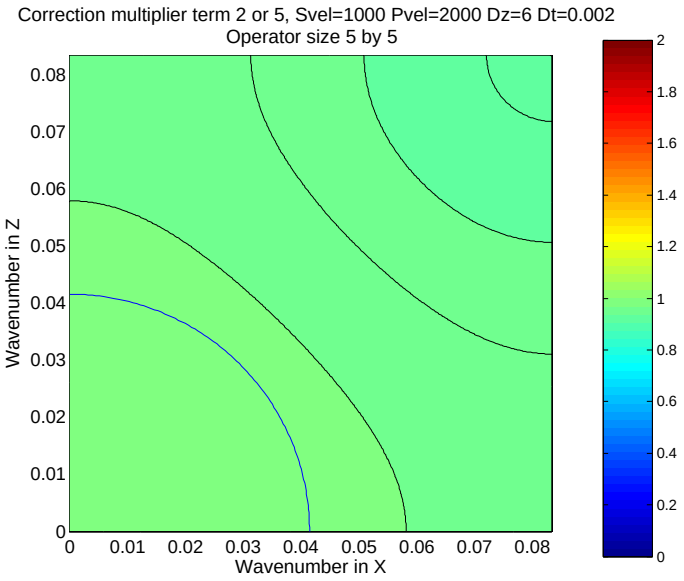

Figure 4.9: The Fourier domain contour plot of the 5 by 5 correction filter (in wavenumbers) for term number 2. Compare with the ideal corrections in Figure 4.8

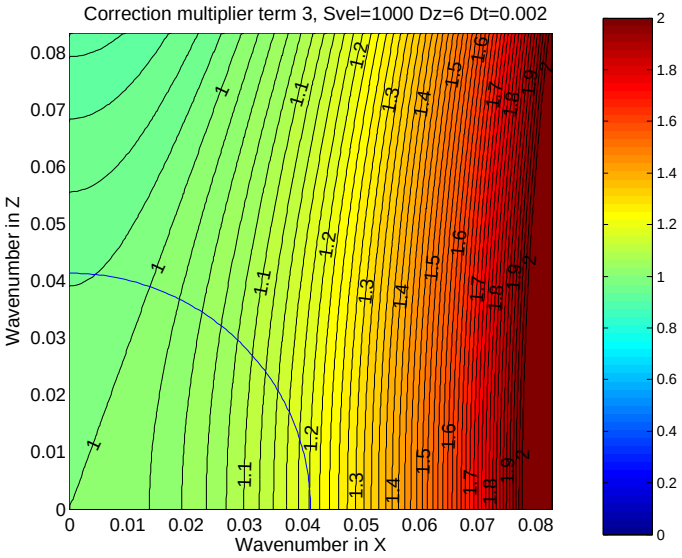

Figure 4.10: The Fourier domain contour plot of the ideal correction multiplier for term number 3.

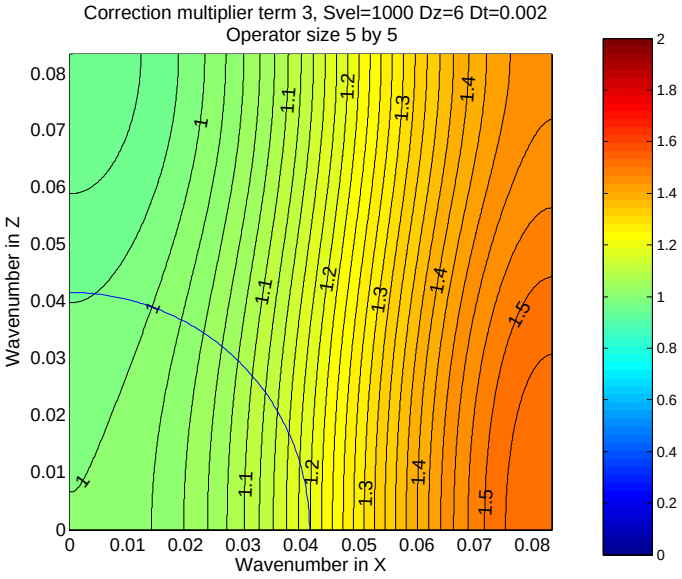

Figure 4.11: The Fourier domain contour plot of the 5 by 5 correction filter (in wavenumbers) for term number 3. Compare with the ideal corrections in Figure 4.10

The ideal corrections and the correction filter responses may be seen as good matches within the design window range.

A correction filter was added to the process used to generate the model in Figure 3.8, and the result is in Figure 4.12. This almost matches the wavenumber domain

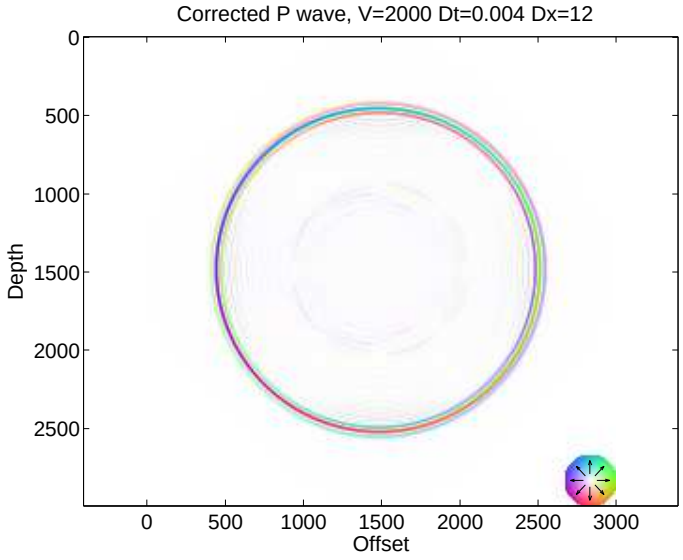

Figure 4.12: This shows the filter correction model corresponding to Figure 3.9, and the results are almost as good.

results in Figure 3.9, being only slightly less precise.

The correction filter was applied to the P/S ring model and the result in Figure 4.13 was obtained. This is very good propagation for both the P and S waves, almost as good as the correction multiplier result in Figure 3.13. The modelling time was 40 percent more than with the uncorrected version, and a little less than the correction multiplier version. The filter design time is very minimal. A more definitive test of wavelet quality preservation is shown in Figure 4.14. The quality of the P-wave is almost identical to that obtained using the ideal correction (in Figure 3.16), and the S-wave quality is also similar except for the additional hash following (to the left

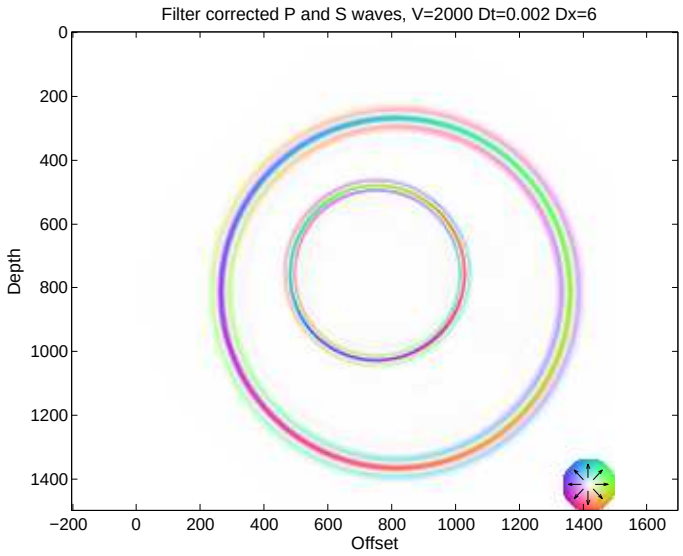

Figure 4.13: This shows the model propagated from Figure 3.11, but with filter corrections. Both the P and S waves have retained their circular shapes, and zero phase character.

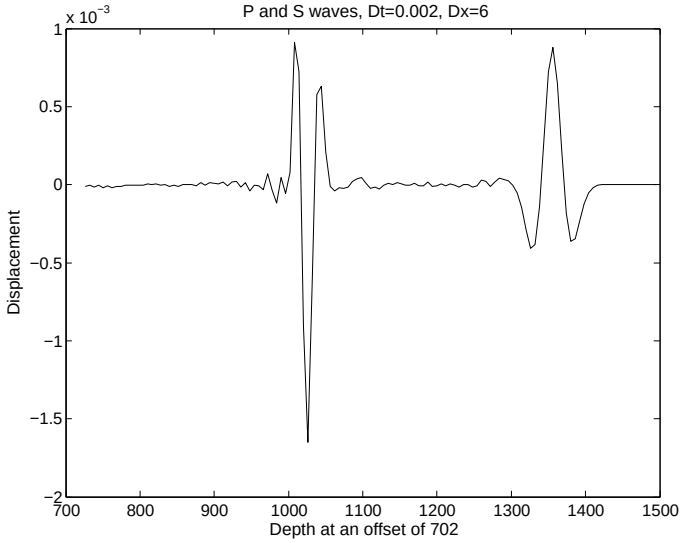

Figure 4.14: A trace extracted from the filter corrected model (Figure 4.13). Even the S-wave (left) compares quite favorably with the ideal operation result from Figure 3.16.

of) the wavelet.

4.3 Correction filters compared to the Levander scheme

As discussed earlier, the whole wavenumber range available within a sampled data set can not be utilized for modelling. Instead of using the theoretical range from zero to the Nyquist wavenumber, the practical range is often limited to a high wavenumber of Nyquist/4 or lower. One of the better known schemes to improve on this is described by Levander (1988).

The Levander scheme uses a split time step system, where the second-order wave equation is split into two first-order equations, and each of these equations is stepped through a time interval of one-half of the time sample rate. It also uses a higher order approximation for the continuous spatial derivatives. Instead of using the first-order operator of $[1, -1]$ for a derivative, the operator $[\frac{-1}{24}, \frac{9}{8}, \frac{-9}{8}, \frac{1}{24}]$ is used for each of the two steps. For comparison purposes, this may be considered to be the first-order operator convolved with a correction filter of $[\frac{-1}{24}, \frac{13}{12}, \frac{-1}{24}]$, although Levander does not use the correction filter concept.

In Levander's scheme, the correction filters are effectively applied to both stages of the split-step process, and so the complete second-derivative corrections are a combination of the two stages of the first-order corrections. The equivalent correction in the direction of the axes (either x or z) is $[\frac{1}{576}, \frac{-13}{144}, \frac{113}{96}, \frac{-13}{144}, \frac{1}{576}]$. The equivalent

correction for the cross-term calculation is a symmetric square function,

$$\begin{bmatrix} \frac{1}{576} & \frac{-13}{288} & \frac{1}{576} \\ \frac{-13}{288} & \frac{169}{144} & \frac{-13}{288} \\ \frac{1}{576} & \frac{-13}{288} & \frac{1}{576} \end{bmatrix}.$$

The first type of operator is the longest at 5 points, requiring two extra points in each direction for the correction to be effective. This must be considered near any boundaries because the extra points are required in both the x and z directions.

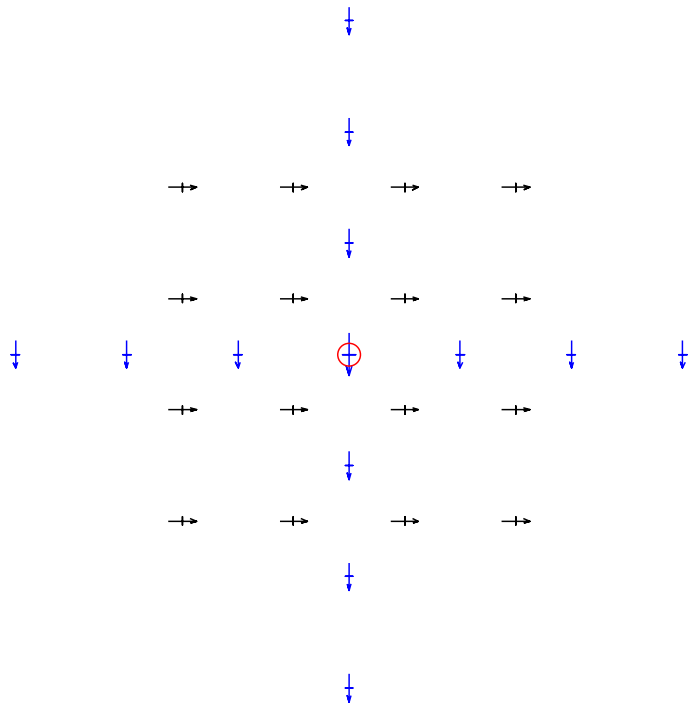

Figure 4.15: All the displacements which contribute to the Levander U_z acceleration at the centre.

Figure 4.15 shows all of the displacements used as input points for the Levander acceleration in z. The $\frac{\partial^2 U_z}{\partial z^2}$ term has input from the column of z displacements. The $\frac{\partial^2 U_z}{\partial x^2}$ term has input from the row of z displacements, and the $\frac{\partial^2 U_x}{\partial x \partial z}$ term has input

from all of the x displacements shown. In contrast, the second order derivatives plus optimum corrections developed in this paper uses a square array of input points for each of the three terms mentioned.

4.4 An example of correction filters compared to the Levander scheme

This example has velocities of 2000 m/sec. and 1000 m/sec. for the P and S waves, a spatial sample rate of 6 metres and a time sample rate of .0018 seconds. The time sample rate was chosen for stability with the Levander method, as specified in Lines et al. (1999) for a fourth-order spatial derivative. The correction filter method actually works better with a time sample rate of .002 seconds, but this would be unstable with the Levander method. A common time sample rate was chosen to allow the 'corrections' to be compared in detail.

The first set of comparisons are in the spatial wavenumber domain. The correction filters in this case have been designed for the spatial region from zero to one-half Nyquist, in both the x and z directions. A cyan coloured arc has been drawn on the plots in this corner so they may be compared more easily.

The first case presented is for the second derivative in the z direction of the z displacement. The ideal correction is shown in Figure 4.16. The Levander fourth-order correction multiplier term is shown in Figure 4.17. This operator is one column of five rows, and appears to be a rough match to the ideal case.

The optimised operator for this term, developed from the theory presented in this thesis, is shown in Figure 4.18. This design matches the ideal quite closely in

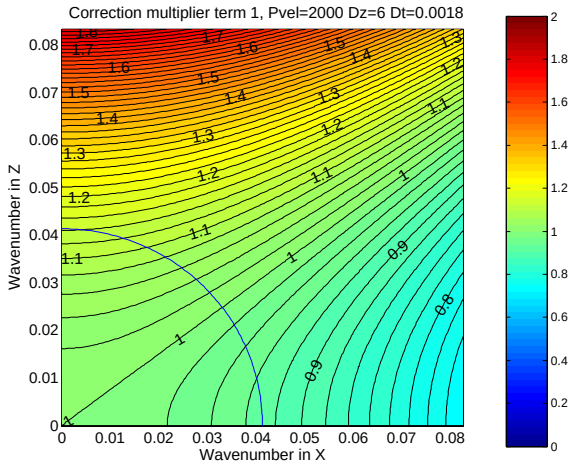

Figure 4.16: The ideal correction multiplier for the $\frac{\partial^2 U_z}{\partial z^2}$ term.

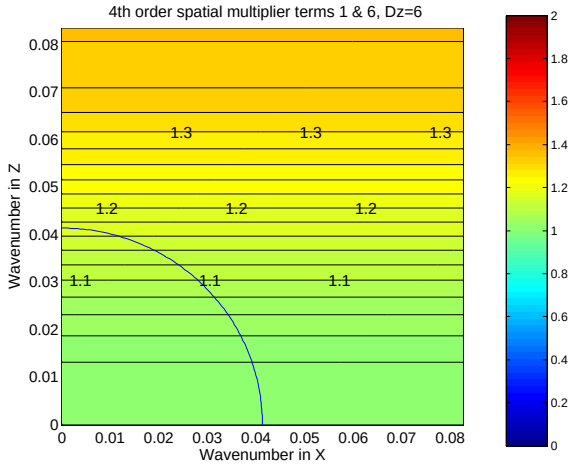

Figure 4.17: The Levander correction multiplier for the $\frac{\partial^2 U_z}{\partial z^2}$ term.

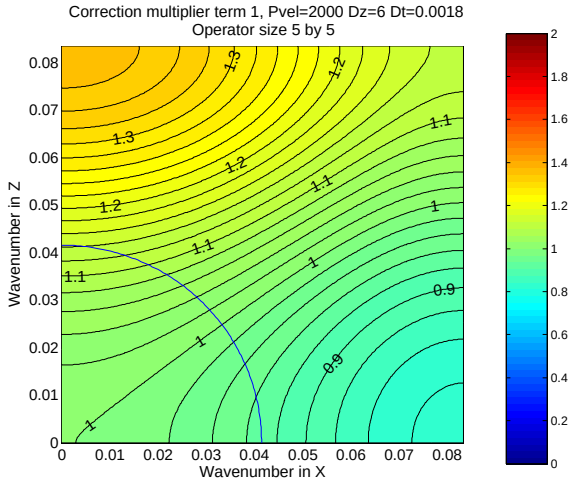

Figure 4.18: The optimum 5 by 5 correction filter for the $\frac{\partial^2 U_z}{\partial z^2}$ term.

the zone within the marked quarter circle.

The second case presented is for the second derivative of either the x or z component with respect to both x and z. The ideal correction multiplier term is shown in Figure 4.19, and in this case shows that very little correction is necessary. This is

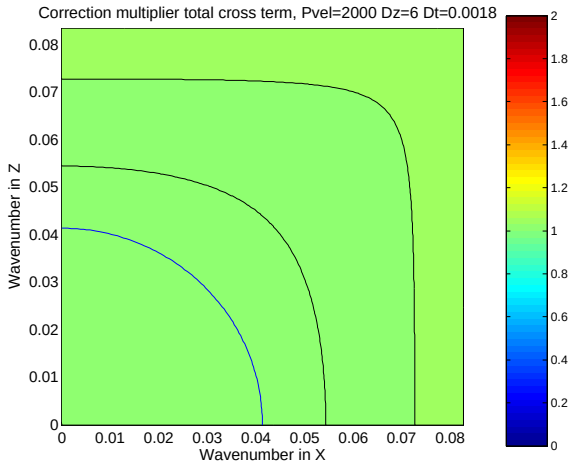

Figure 4.19: The ideal correction multiplier for the $\frac{\partial^2 U_z}{\partial x \partial z}$ term.

consistent with the uncorrected propagation of the ring model, where at 45 degrees

the wavelet is comparatively undistorted (see Figure 4.24). The Levander correction for this term is shown in Figure 4.20, and in this case is over corrected. This can happen because the correction is designed mainly for use in the direction of the axes, and not for the cross terms. The 5 by 5 correction filter designed for the same case

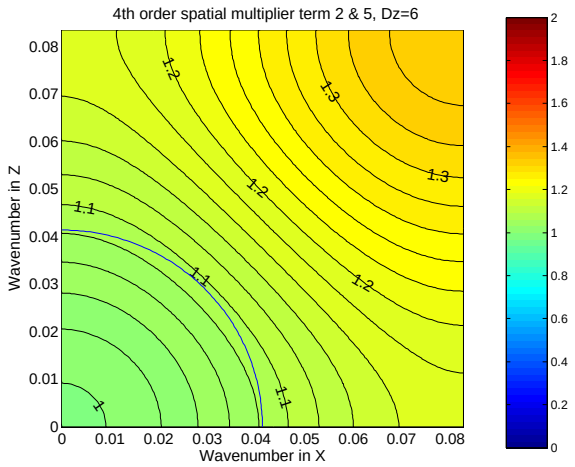

Figure 4.20: The Levander correction multiplier for the $\frac{\partial^2 U_z}{\partial x \partial z}$ term.

is shown in Figure 4.21. The term was designed specifically, and therefore matches quite well.

The last case presented is for the second derivative of the x component in the z direction. This is for term 6, the last term of the second operator (see table 3.2). The ideal correction multiplier for this sixth term is shown in Figure 4.22, where the relevant shear velocity is 1000 m/sec. The Levander correction in Figure 4.17 applies to this case too, because it is determined only by the value of the second derivative. The ideal correction is distinct for this case because it allows for the inaccurate second derivative in time, and is affected by the shear velocity and time sample rate. The optimised correction filter response is shown in Figure 4.23, and

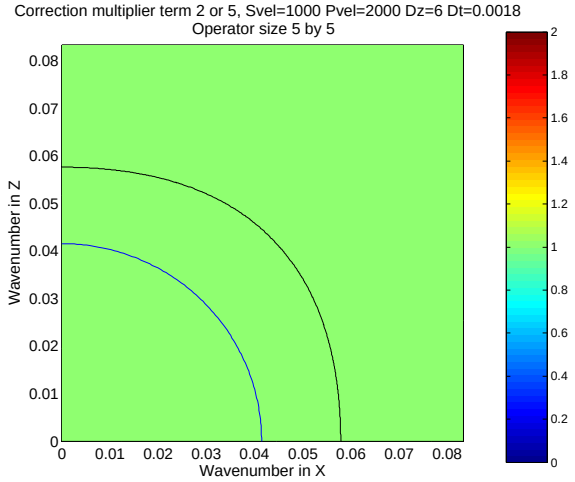

Figure 4.21: The optimum 5 by 5 correction filter for the $\frac{\partial^2 U_z}{\partial x \partial z}$ term.

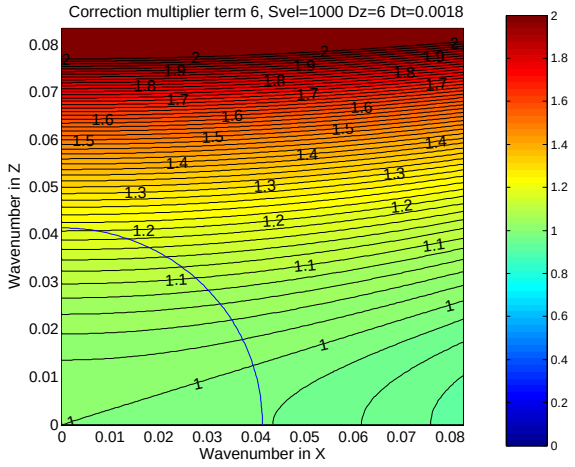

Figure 4.22: The ideal correction multiplier for the $\frac{\partial^2 U_x}{\partial z^2}$ term.

it matches quite well in the lower wavenumbers region.

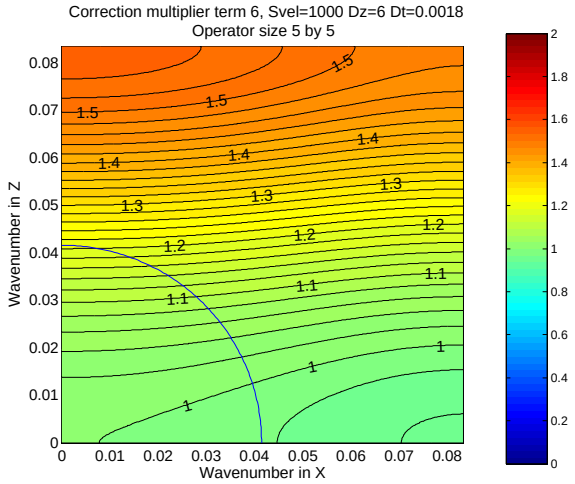

Figure 4.23: The optimum 5 by 5 correction filter for the $\frac{\partial^2 U_x}{\partial z^2}$ term.

The second set of comparisons are in the space domain, and parallel the frequency domain type of modelling done in section 3.9. The P/S ring model here was also started from the initial position given in Figure 3.11, and the model was propagated through 134 steps of .0018 seconds each. This time step was chosen because it is close to the largest possible while still providing stability. With the Levander method, as with other models, small time sample rates cause more dispersion.

The result is shown in Figure 4.24, where the numerical dispersion and non-circular shape of the smaller shear ring is quite obvious, and the larger pressure ring can be seen to deviate from its original zero phase (symmetrical) shape.

The second display in Figure 4.25 shows the result of the simulated Levander-style wave propagation. The pressure wave has been propagated more accurately as shown by the wavefront shape being almost zero phase (symmetric). The shear wave wavelet has been improved in quality but the wave front has an even stronger

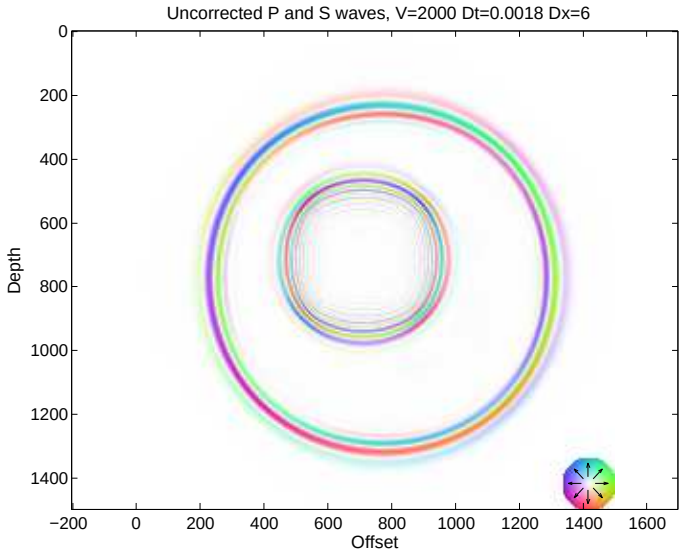

Figure 4.24: The uncorrected P and S wave model with $\Delta t = .0018 secs$. This is close to the maximum time sample rate which still ensures stability with 4th order methods.

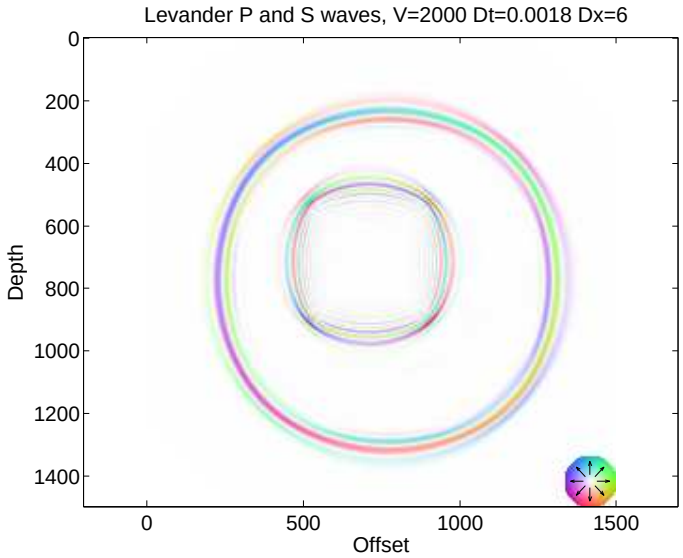

Figure 4.25: The model of Figure 4.24, but with the Levander style corrections.

deviation from circular. That the shear wave propagation is less than ideal is not surprising, since the system was not designed for shear waves.

The next display in Figure 4.26 shows propagation by the optimised correction filter of size 5 by 5. Both the pressure and shear rings here are circular, and the

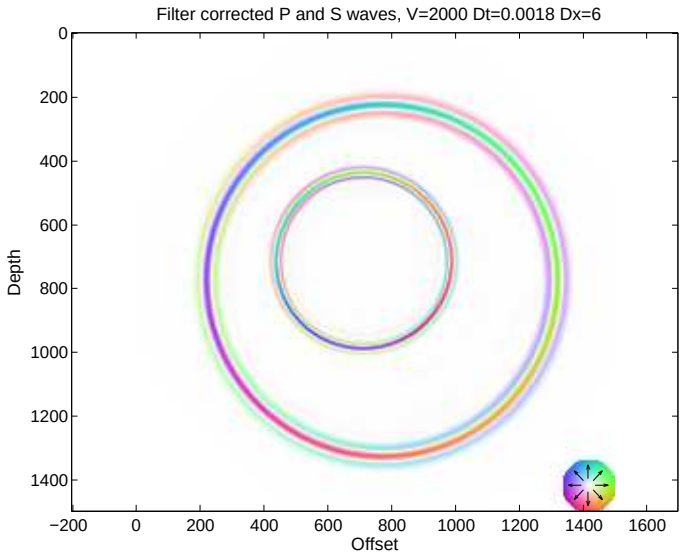

Figure 4.26: The model of Figure 4.24, but with correction filters applied.

wavelets are compact and zero phase.

4.5 Correction filters in a model with two velocities

The theory of correction multipliers and correction filters was developed within models with a constant velocity, but the designed filters are still effective in more complex models. At a boundary between high and low velocity regions a filter designed for one region will have to have some of its coefficients operate on samples from the other region. The corrections at these points will not be accurate, but will still usually have a beneficial effect, even where the velocity contrasts are quite severe. Also,

the area near strong velocity contrasts is usually small compared to the size of the model, so the corrections may be considered to be accurate over most of the model.

An example of a model with two velocity regions is given here. In Figure 4.27, a 30 Hz. P-wave ring was initiated in a 2000 m/sec. region, just above a second region with a velocity of 1400 m/sec. There is obvious numerical dispersion on the primary

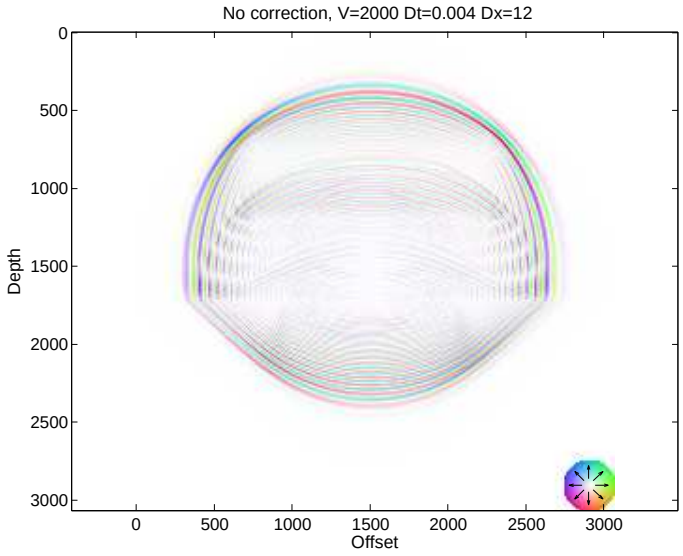

Figure 4.27: Uncorrected two velocity P-wave model.

P-wave, as well as the reflected and transmitted P-waves.

Figure 4.28 shows the same model, but with two separate suites of corrections applied, one for each of the two velocity regions. The three wavefronts of P-wave energy here show major improvements. Also, reflected shear wave energy is apparent, and there is a slight indication of a transmitted shear wave. Dispersion is very apparent.

Numerical dispersion may be reduced by the application of correction filters, but is ultimately limited by sample rates that are too coarse. Figure 4.29 shows the

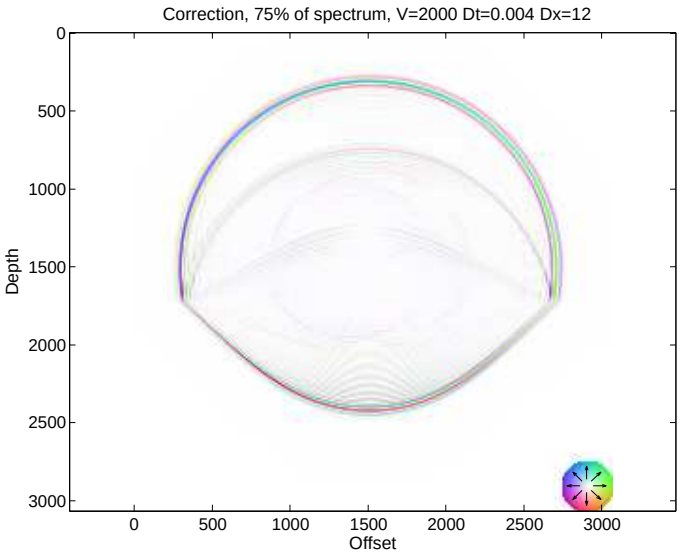

Figure 4.28: Corrected two velocity P-wave model of Figure 4.27.

same model, uncorrected, but with much finer sample rates. The refinement of the sample rates has improved the quality of the P-wave events, almost to the point where the filter corrections are not required. Considerable numerical dispersion still appears on the S-wave events.

Figure 4.30 is the corrected version of the finely sampled model. Even the weak reflected and transmitted shear wave events have very little dispersion. The change in polarity of these events is obvious at the point where the P-wave intersected with the velocity boundary at right angles.

The High Velocity Wedge model is shown in Figures 4.31 and 4.32 as another uncorrected and corrected modelling pair.

The model has 4000 m/sec (P-wave) zones in the top left, and in the bottom layer. Between the two high velocity zones is a medium of 2000 m/sec. The S-wave velocities were set to one-half the P-wave velocities. The correction matrices here

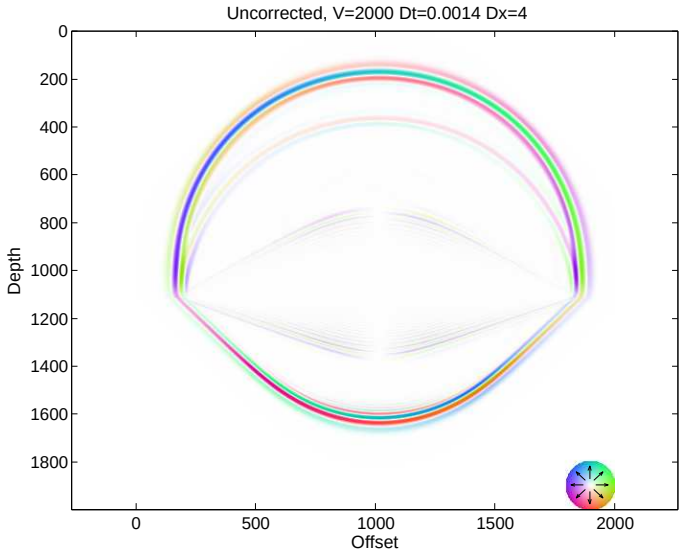

Figure 4.29: Uncorrected two velocity P-wave model.

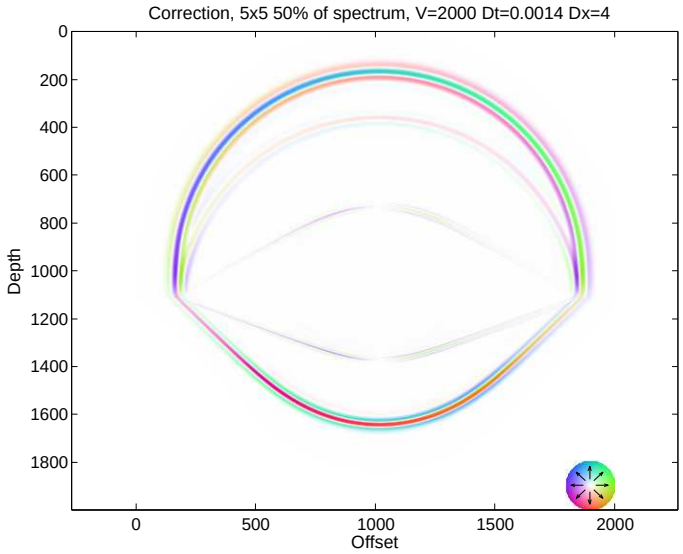

Figure 4.30: Corrected two velocity P-wave model of Figure 4.29.

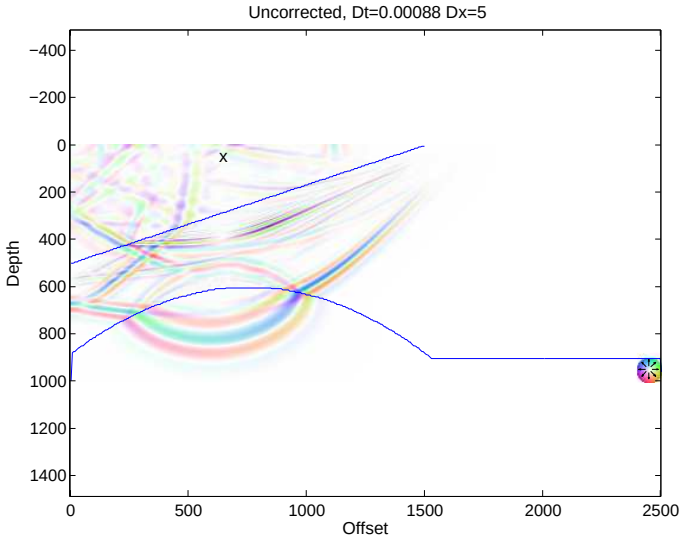

Figure 4.31: An uncorrected shot in the High Velocity Wedge model.

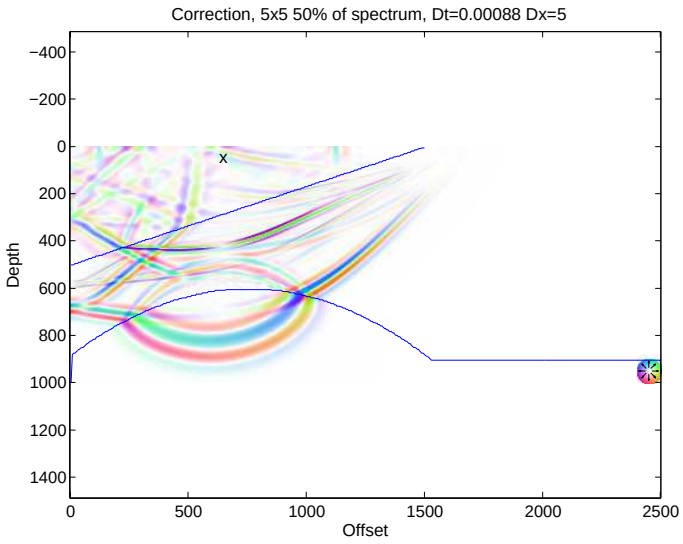

Figure 4.32: A corrected shot in the High Velocity Wedge model.

are of size 5 by 5, which may be seen to reduce some of the shear wave dispersion in Figure 4.31.

The same model pair is shown in Figures 4.33 and 4.34 in the interpreted P/T (Pressure/Twist) colour format (see appendix F).

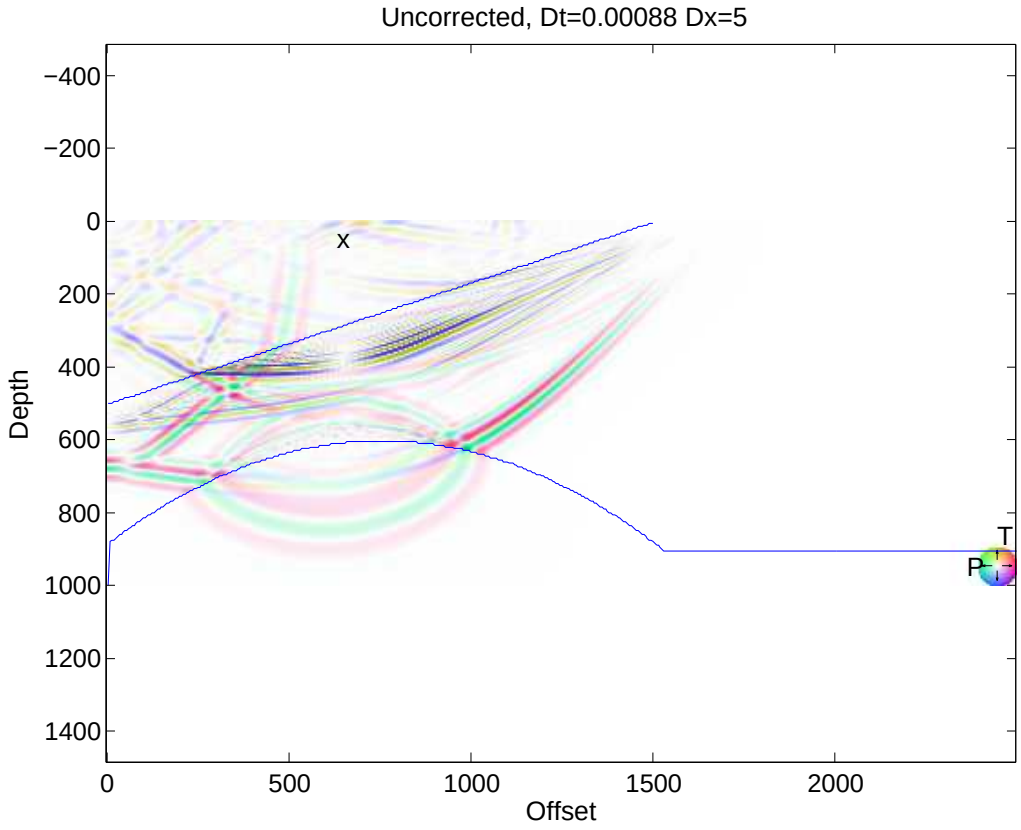

Figure 4.33: An uncorrected shot in the High Velocity Wedge model, interpreted with the PT format.

This format tends to separate the pressure and shear wave energy. Figure 4.34 shows that the corrections do not have a major effect on the P-wave events, but tend to concentrate the S-wave events.

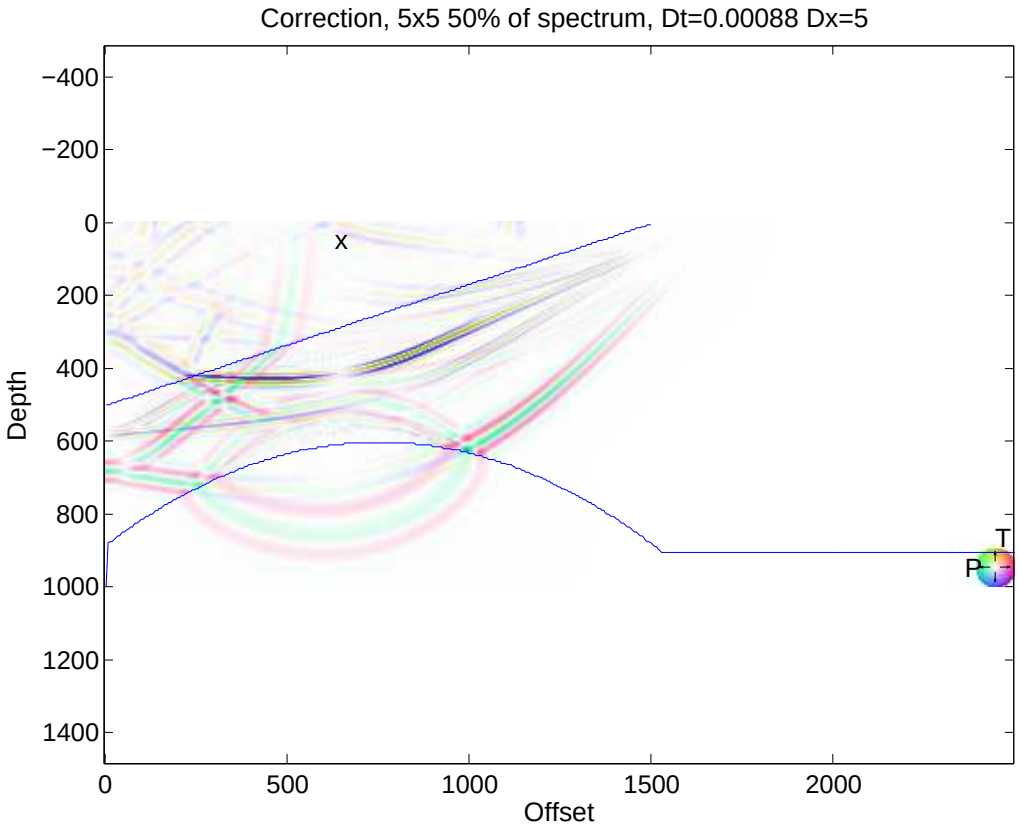

Figure 4.34: A corrected shot in the High Velocity Wedge model, interpreted with the PT format.

Chapter 5

Transmitting boundaries

An important part of many finite-difference models is to have minimal reflections from most of the external boundaries, and simulate the infinite real earth. This is important for economic reasons, so that a model size can remain small and yet simulate the effects of specified internal and external boundaries without getting interference from the other model edges.

In the finite-difference literature, these boundaries can be known as 'numerical boundaries' (Strikwerda, 2004). They are called 'numerical boundaries' to distinguish them from real boundaries, where physical conditions apply (for example, zero stress). In Strikwerda, the emphasis is on boundaries which will not cause instability, as these can affect the whole model.

The basic technique is to provide extra rows and columns of points around the edges of a model. Reasonable displacement amplitudes at these points are needed to allow the finite-difference operations to be executed within the model, but cannot themselves be generated by the same techniques because of their edge positions. Unique algorithms, or in some cases unique conditions, must be used to calculate these displacement amplitudes.

The earlier techniques used to reduce boundary effects were called absorbing boundaries, and simulated the effects of having a highly attenuating material around the model. This technique is very practical where the modelling already accounts for viscous effects on the particle motion, see Kelly and Marfurt (1999) page 423. The

viscosity is simply made very high for several rows and columns around the model's area of interest.

Another absorbing technique that can be used is to taper, at each time step, the amplitudes toward the model edge by a minimal amount. Cerjan et al. (1985) got very successful results by tapering to a maximum of 0.92 across a boundary zone of 20 points in width. With these absorbing boundaries, the edge point amplitudes are calculated by an approximate algorithm, but any error that this introduces is shielded by the attenuating zone. The increased overhead caused by providing the attenuating zone is usually not a major barrier with modern computers.

An alternative to absorbing boundary conditions can be called transmitting boundary conditions. Reynolds (1978) called his boundaries transmitting, and although Clayton and Engquist (1977) called their boundaries absorbing, they used algorithms similar to Reynolds. These algorithms project amplitudes into the boundary zones from the values already calculated for the zone of interest. Clayton and Engquist adapted a migration algorithm to project boundary values. Reynolds factored the wave-equation and then used approximations for finite-differencing. A requirement of these techniques is to select only those solutions that advance into the boundary, and suppress solutions that advance out of the boundary (the reflections). They are found to work very well with waves moving directly toward the boundary, but not so well with waves approaching the boundary at an acute angle.

The most general method found to date is given in Randall (1988), using a method developed by Lindman (1975). Lindman called the problem the 'free-space' boundary condition. They determine a spectrum of wavenumbers and frequencies in the vicinity of the boundary to design an operator which projects a scalar potential

across it. They claim very high accuracy to within 1 degree of the boundary direction for an analytic solution, and limited only by the sampling for the finite-difference solution.

This section of the thesis experiments with the eikonal equation as a means of describing the conditions of a transmitting boundary. This is an analytic equation, and so the finite-difference version suffers from accuracy problems of the same type as those treated in the main sections of this thesis. In fact the eikonal equation has first derivatives of first order accuracy, compared with the wave equation with second derivatives, having second order accuracy. These inaccuracies were not specifically addressed, yet some encouraging results were found.

In the space of values at the transmitting boundary edge of a digital model, two unknowns must be found. The first unknown is the extra (beyond the) boundary value displacement amplitude, and the second unknown is the advanced time-step amplitude that is calculated using the extra boundary value. The first of the two equations that is required for a solution is, of course, the time-stepping equation. A second equation that may be used is the one that relates all the first derivatives of an unimpeded advancing wave (the appropriate eikonal equation). Any solution that does not satisfy this equation must involve some reflected energy.

The above simultaneous solution takes the form of a quadratic. The root of the quadratic must be chosen so that the slope of the wave toward the boundary is consistent with the slope in time of an advancing wave. In particular, a slope down toward the boundary must accompany more positive amplitudes with time, and vice-versa.

5.1 Transparent boundaries in the one dimensional case

Before developing the theory of two dimensional transmitting boundaries, it is useful to show the nature of the solution for a one dimensional case. The one-dimensional wave equation is given in equation 2.2 from section 2, and the time stepped solution is given later in that section. In general terms, the un-corrected solution for the advanced time step ($\phi(x, t + \Delta t)$) is given in terms of the current and adjacent displacements at x, and also the previous displacement at x, with a function F, so that

$$\phi(x, t + \Delta t) = F(\phi(x - \Delta x, t), \phi(x, t), \phi(x + \Delta x, t), \phi(x, t - \Delta t)). \tag{5.1}$$

Figure 5.1 shows a model of a one-dimensional material displaced vertically, for example a string. The string extends from upper right an indefinite distance toward the lower left. It is represented by the limited lines of the model which are oriented in the same direction. The succession of strings toward the lower right represent the same string at later times. The wave in the string can be seen approaching the supposedly non-existent boundary to the left.

The black cross in Figure 5.1 shows the five points where the displacements must satisfy the relationship specified in equation 5.1. The red cross shows one of the locations where equation 5.1 will be used for construction of a new representation of the line at the next time step.

Figure 5.2 shows an additional cross at the last directly modelled point for the newly built string, with one of the required input points dangling in space. This is the point mentioned above, where a second equation is required to solve for the two unknown displacements. The eikonal equation is a possibility to fulfill this.

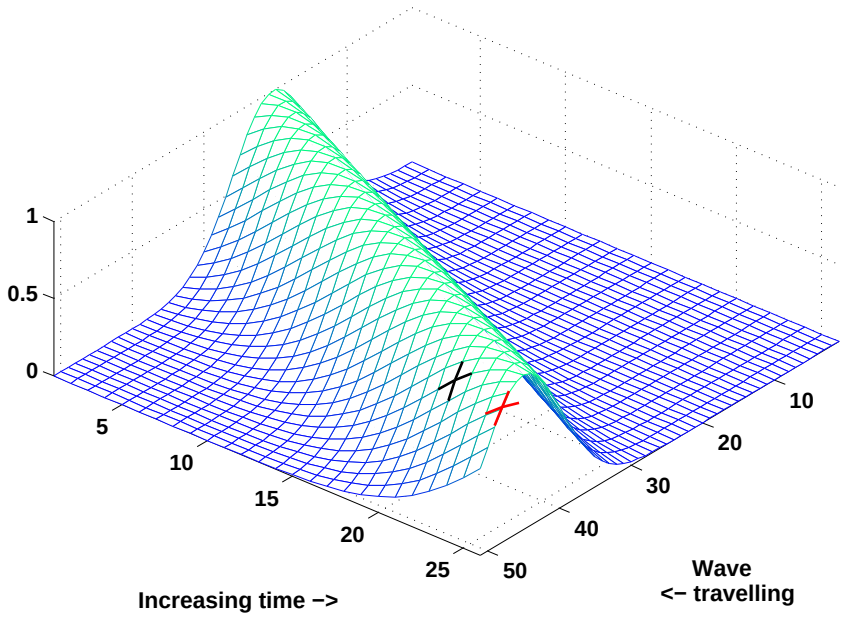

Figure 5.1: The string (one-dimensional) model displayed at successive points in time. The time stepping equation relates the displacements at the two crosses shown, and could be duplicated at most other parts of the grid. The black cross represents each point on the space/time grid where the equation must hold. The red cross shows an example of where a string displacement at an advanced time may be calculated from the displacements at the other four positions covered by the cross.

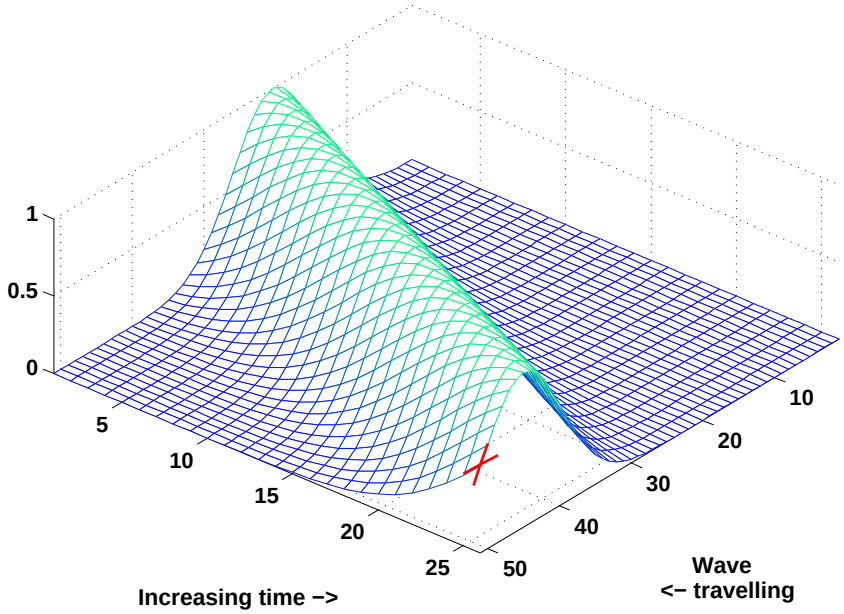

Figure 5.2: The red cross shows a boundary point for the string model. The two unknowns are represented by the two ends of the cross which are not part of the grid of known displacements.

The one-dimensional eikonal equivalent equation is given by

$$\frac{\partial \phi}{\partial x} = -\frac{1}{v}\frac{\partial \phi}{\partial t}, \tag{5.2}$$

where the negative sign requires that the wave advance to larger x. This may be translated into a finite-difference equation of the form

$$\phi(x, t + \Delta t) = G(\phi(x - \Delta x, t), \phi(x + \Delta x, t), \phi(x, t - \Delta t)). \tag{5.3}$$

This second equation gives enough information to solve for both of the unknown points in Figure 5.2. The details of the simultaneous solution is completed for the two-dimensional equation below.

5.2 Theory

The development of the theory starts with the definition of a scalar plane-wave, which may be chosen to advance with time

$$P = F\left((zcos\theta + xsin\theta)k - \omega t\right). \tag{5.4}$$

Then an equation relating the first derivatives of the function may be shown to be

$$\left(\frac{\partial P}{\partial x}\right)^2 + \left(\frac{\partial P}{\partial z}\right)^2 = \frac{k^2}{\omega^2}\left(\frac{\partial P}{\partial t}\right)^2 = \frac{1}{v^2}\left(\frac{\partial P}{\partial t}\right)^2. \tag{5.5}$$

This is the well known eikonal equation. Note that the squaring of the derivatives destroys the sign of the inward or outward wave, so that the selection of an outward advancing wave must be made by choosing the correct root.

This equation of the scalar function P may be translated into a finite-difference version using central differences. If m, n, and k represent the function at x, z, and

t respectively, then

$$\left(\frac{P(m+1)-P(m-1)}{2\Delta x}\right)^2+\left(\frac{P(n+1)-P(n-1)}{2\Delta z}\right)^2= \frac{1}{v^2}\left(\frac{P(k+1)-P(k-1)}{2\Delta t}\right)^2, \quad (5.6)$$

where $P(m,n,k)$ has the independent variables omitted unless they have been incremented or decremented. At the right x border, where m now represents the x edge, the decremented variables can be assumed to represent the interior spaces and older times, and are therefore known. Also all the n's are known in the z direction $(n+1)$ and $(n-1)$. The two unknown amplitudes are $P(m+1)$ and $P(k+1)$.

If R is defined by

$$R^2=\left(P(n+1)-P(n-1)\right)^2, \quad (5.7)$$

and

$$C=\Delta x/v\Delta t, \quad (5.8)$$

where $\Delta x=\Delta z$ and generally $C\geq 1$ for stability, then

$$\left(P(m+1)-P(m-1)\right)^2+R^2=C^2\left(P(k+1)-P(k-1)\right)^2. \quad (5.9)$$

The scalar wave equation

$$\frac{\partial^2 P}{\partial x^2}+\frac{\partial^2 P}{\partial z^2}=\frac{1}{v^2}\frac{\partial^2 P}{\partial t^2}, \quad (5.10)$$

has a finite-difference representation of the form

$$\frac{P(m+1)-2P+P(m-1)}{(\Delta x)^2}+\frac{P(n+1)-2P+P(n-1)}{(\Delta z)^2}= \frac{1}{v^2}\frac{P(k+1)-2P+P(k-1)}{(\Delta t)^2}, \quad (5.11)$$

which may be converted into the form

$$P(k+1) = 2P - P(k-1) + \frac{1}{C^2}\left(P(m+1) + P(m-1) + P(n+1) + P(n-1) - 4P\right). \quad (5.12)$$

Again, the two unknown amplitudes are $P(m+1)$ and $P(k+1)$.

If D is defined by the equation

$$D = 2C^2P - 2C^2P(k-1) + P(m-1) + P(n+1) + P(n-1) - 4P, \quad (5.13)$$

then, when equation 5.12 is substituted into equation 5.9 the quadratic equation in $P(m+1)$ which can be derived is

$$P^2(m+1) - 2\left(\frac{C^2P(m-1) + D}{C^2 - 1}\right)P(m+1) + \frac{C^2P^2(m-1) + C^2R^2 - D^2}{C^2 - 1} = 0, \quad (5.14)$$

which can be solved for $P(m+1)$, and using 5.12, for $P(k+1)$. The root that must be chosen for the right (x) boundary is the one for which

$$(P(m+1) - P(m-1)) * (P(k+1) + P(k-1)) \leq 0, \quad (5.15)$$

ensuring that when the difference in the x direction is positive, the difference in the time direction is negative, and vice-versa. These are the conditions for a wave advancing into the right boundary.

For the special case $C = 1$, the solution for $P(m+1)$ is

$$P(m+1) = 2P + 2P(k-1) - P(n+1) - P(n-1) + \frac{R^2}{2P(m-1) + 2D}. \quad (5.16)$$

5.3 Application to the elastic wave equation

The boundary conditions specified above have been adapted to the elastic wave equation by converting the elastic wave displacements into two sets of scalar amplitudes in the region near the boundaries. This decomposition has been done by Randall (1988) and Long and Liow (1990). A compressional potential is sufficient to describe the pressure wave (P), which Long and Liow called dilation. Shear distortion requires a vector potential in a three dimensional model, but a scalar potential is sufficient in the two dimensional case (T), Long and Liow calling this rotation. Figure 5.3 shows the relative positions of the x and z displacements and the P and T potentials within the staggered grid, all near the right side x boundary.

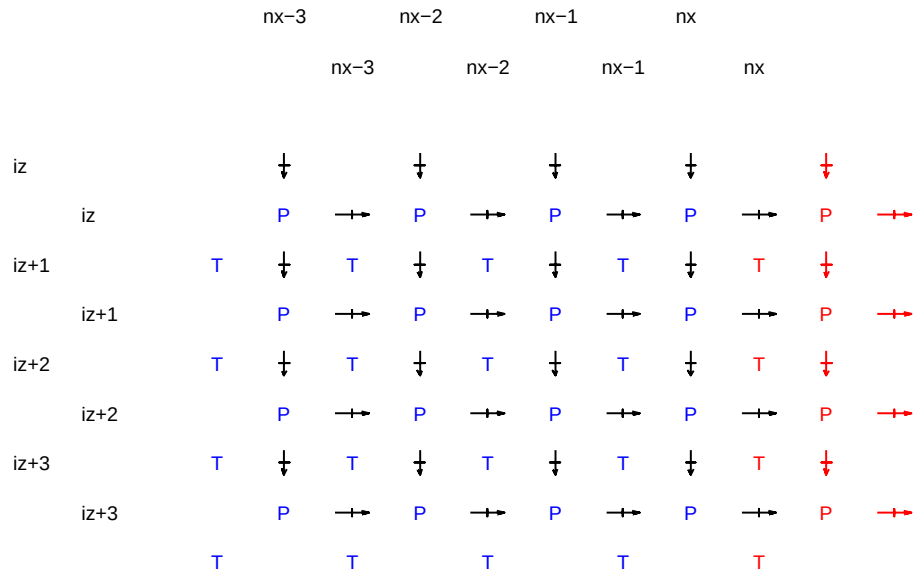

Figure 5.3: The staggered grid displacements with the scalar potentials near the right boundary. The projected scalars and vectors are shown in red.

Note that the difference in displacements from above and below each 'P' position gives a measure of the pressure contribution from the z direction. Similarly, the

difference in displacements from left and right of each 'P' position gives a measure of the pressure contribution from the x direction. The total pressure is the sum of these two, so that

$$P(m,n) = [U_x(m-1,n) - U_x(m,n)] + [U_z(m,n) - U_z(m,n+1)]\,. \tag{5.17}$$

In a similar fashion, a twist (clockwise) may be determined from the displacements surrounding each 'T' position. These are located at the intermediate positions staggered from the pressure positions. The formula for these is

$$T(m,n) = [U_x(m,n-1) - U_x(m,n)] - [U_z(m,n) - U_z(m+1,n)]\,. \tag{5.18}$$

Note that the relative values of the indices for U_x, U_z, P and T depend on how a particular staggered grid system is defined.

The positions of U_x, U_z, P and T are related graphically in Figure 5.3. The displacements calculated within the normal (interior) positions of the model are shown by the arrows in black. The blue P's and T's are calculated from these displacements. The P's and T's are estimated at the red positions by the scalar projection described above. The projected T's allow the red z displacements to be calculated, and then the P's may be used to calculate the x displacements.

5.4 Examples

The first example is shown in Figures 5.4, 5.5, and 5.6. Figure 5.4 shows a pressure wave about to encounter a transmitting boundary. It originates as an explosive source at the symmetric boundary on the left. The parameters are: compressional velocity is 1600 m/sec, shear velocity is 800 m/sec, $\Delta x = 2$ m, and $\Delta t = .0006$ seconds.

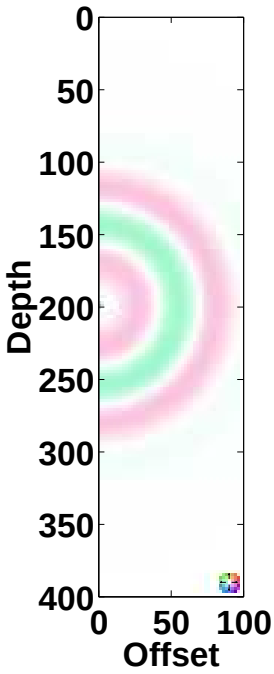

Figure 5.4: A pressure wave about to reach a transmitting boundary at right angles. The source is a compressive wavelet on the symmetric edge.

Figure 5.5 shows the pressure wave after it has encountered the transmitting boundary. There is almost no indication of reflected energy with incident angles of zero degrees through about plus and minus 70 degrees.

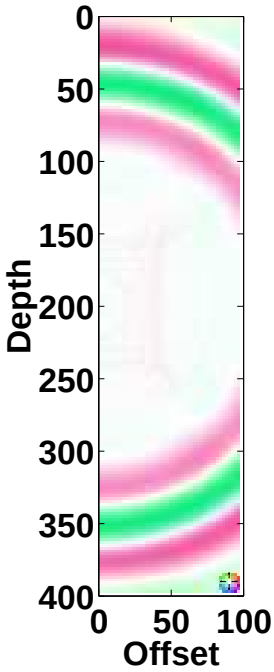

Figure 5.5: A pressure wave after reaching the transmitting boundary. There is very little reflection energy from the boundary for incident angles ranging from +/- 70 degrees.

Figure 5.6 shows the wave after it has reached the corners of the model. The upper right corner is where the transmitting boundary meets the free surface boundary, and the beginning of a Rayleigh wave may be seen. Elimination of reflections here requires the simultaneous solution of the transmitting conditions and the free surface conditions, and this has not yet been accomplished. By contrast, the lower right corner is where the totally reflecting and transmitting boundaries meet, and there is not much of a problem.

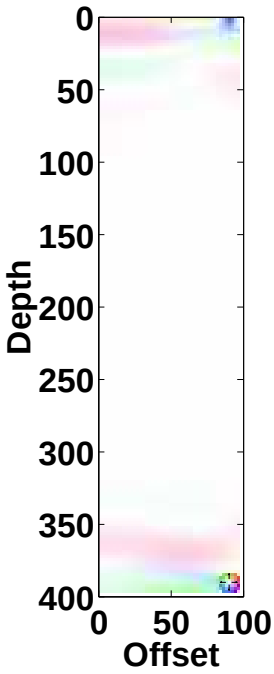

Figure 5.6: A pressure wave encounter at the free surface/transmitting corner. A strong Rayleigh wave has been generated.

The second example is from the case studies, section 6.2.4. Figure 5.7 is a duplicate of Figure 6.14 from that section, which displays a model with a transmitting right boundary at 200 milliseconds after the shot.

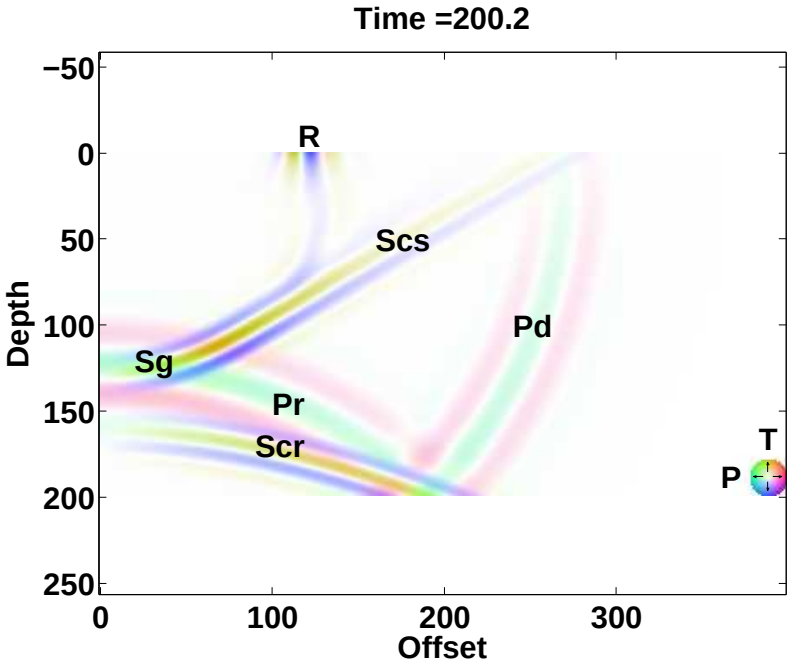

Figure 5.7: Snapshot of case 1, basic model with 9m. source. The right boundary is transmitting. This is a duplicate of Figure 6.14

The model was continued for another 200 milliseconds, and displayed in Figure 5.8. The direct pressure event Pd has moved cleanly across the boundary, and the reflection of Pr from the surface (Prs) shows no reflection from the boundary. Also, the shear events Scr (moving up) and Scs (moving down) show no boundary reflections. The beginnings of a surface wave may be seen in the top right corner.

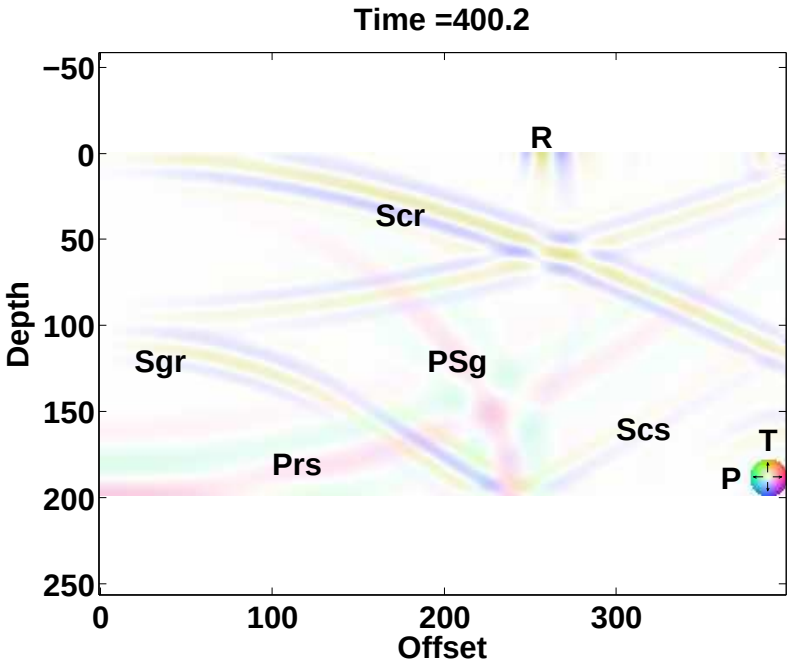

Figure 5.8: Snapshot of case 1, basic model continued for 200 ms. The pressure event Pd has made a clean escape across the boundary. Also, the high angle pressure event Prs and shear event Scs (moving down) and Scr (moving up) show no boundary reflections.

5.5 Conclusions

- The eikonal equation can be combined with the scalar wave equation at a boundary to solve for the unknown amplitude across the boundary.
- The transmitted wave amplitude is the solution to a quadratic with the choice of sign corresponding to the direction of wave motion across the boundary.
- The method can be extended to the 2D elastic case by solving for scalar potentials at the boundary corresponding to pressure and twist effects.
- Tests on simple models show the method to be effective for a broad range of incidence angles.

Chapter 6

Finite-difference case studies

6.1 Surface waves

6.1.1 Introduction

This study shows the result of numerical experiments where Rayleigh waves encounter abrupt near surface velocity changes. These results are easily obtained, but have not been found in the literature, and so have been included here. Exploration seismologists are generally motivated to study Rayleigh waves because their high energy near the shot point masks the valued reflections from deep horizons. There is also some hope that a better understanding will allow an interpretation of near surface conditions around the source point.

There are many papers showing successful finite-difference simulations of surface waves, but their main focus is on earthquake seismology. Levander (1990) surveys several significant Rayleigh and Love wave studies and their interactions with body waves at surface anomalies. In one of Levander's own papers covering the subject (Levander, 1985), he developed an isolated Rayleigh wave designed for a particular layered earth, and propagated it through several realistic models of the earth's crust. Many papers use finite-difference methods to simulate how abrupt topographic changes affect surface waves and convert energy to other wave forms. A paper by Robertsson and Holliger (1997) is one example of these.

6.1.2 Source wavelet

Surface waves have been studied mathematically since Rayleigh's work in the 19th century (Rayleigh, 1885), but usually in reference to earthquake generated waves observed at long distances from their origin. Here the waves have formed into natural vibroseis sweeps, with a single frequency at any given time, but the frequency gradually changing with time. These can be effectively modelled as single frequency waves, and equations 6.2 and 6.3 can be used to describe the real and imaginary components of these waves. Note that the single frequency in time is given in the last term of each equation. The relative amplitudes of the components on the surface and at depth are given in the rest of the equations.

The key to constructing a surface 'wavelet' is then to sum earthquake type waves with a sampling of frequencies and the proper amplitudes so that the result takes a compact form in both space and time. Levander has also used this trick.

The examples shown here build a Rayleigh wavelet similar to the one in Levander (1985), but designed for a simple half-space. The construction begins with an estimate of the wavelet propagation speed c, given by a formula from Achenbach (1973), page 192. The Achenbach equation is

$$c \approx \beta \frac{0.862 + 1.14\sigma}{1 + \sigma}, \tag{6.1}$$

where β is the shear wave velocity and σ is Poisson's ratio. This velocity can be checked as a solution for Rayleigh's equation, as for example equation 3.7 in Grant and West (1965). For realistic exploration near surface conditions, this velocity was found to be accurate to within 0.1 percent.

This velocity (c) may then be used to translate time frequencies into spatial

wavenumbers, but also within the formulae for the x and z displacements. The other symbols in the following equations are β for the shear wave velocity as given above, α for the pressure wave velocity, and ω for the single frequency. The equations are

$$U_x = \frac{\alpha}{c} A \left[e^{-\zeta z} - (1 - \frac{c^2}{2\beta^2}) e^{-\xi z} \right] cos \left[\omega (\frac{x}{c} - t) \right] \tag{6.2}$$

and

$$U_z = -\frac{\alpha}{c} \sqrt{1 - \frac{c^2}{\alpha^2}} A \left[e^{-\zeta z} - (1 - \frac{1}{1 - c^2/2\beta^2}) e^{-\xi z} \right] sin \left[\omega (\frac{x}{c} - t) \right], \tag{6.3}$$

where ζ is defined by

$$\zeta = \frac{\omega}{c} \sqrt{1 - \frac{c^2}{\alpha^2}}, \tag{6.4}$$

and ξ is defined by

$$\xi = \frac{\omega}{c} \sqrt{1 - \frac{c^2}{\beta^2}}. \tag{6.5}$$

These equations are expanded versions of the equations for U and W on page 61 from Grant and West (1965).

The method creates an isolated Rayleigh wavelet defined on the surface and at depth, and a second similar wavelet displaced in position and phase to define how the wavelet propagates. The following steps were used to construct this wavelet, similar to Levander's wavelet:

1. Generate a suitable zero phase surface wavelet, for example, a Ricker wavelet.

2. Do a discrete Fourier analysis of the wavelet, obtaining only cosine terms when the wavelet is zero phase.

3. Translate each frequency into a wavenumber and resample if necessary.

4. For each wavenumber, generate a discrete cosine trace of the analysed amplitude for the surface case.

5. For each wavenumber, create a matrix with the surface trace from above, and deeper traces with the modified amplitudes given by equation 6.3.

6. Sum the matrices for the U_z component.

7. For each frequency/wavenumber, generate a sine trace of the same amplitude as the cosine trace, but modified by the factor from equation 6.2, for the surface case.

8. For each frequency, create a matrix with the surface trace from above, and deeper traces with the modified amplitudes given by equation 6.2.

9. Sum the matrices for the U_x component.

10. Repeat steps $4 - 8$ with the cosine and sine series advanced sufficiently to simulate the wavelet advanced by c times the time stepping time.

An initial wavelet generated by this means is shown in Figure 6.1. Figure 6.2 shows the form of the wave after propagation through 60 time steps of 0.0004 seconds. A Rayleigh wave in a uniform velocity half space, as is used here, should have no dispersion and thus preserve its wave form. The fact that the wave does not show dispersion indicates that most of its energy is in the form of a Rayleigh wave.

6.1.3 Rayleigh wave examples

The examples all begin with a 30 Hz Ricker surface wavelet in a half space and show vertical displacements at the surface as time advances. The half space velocity for

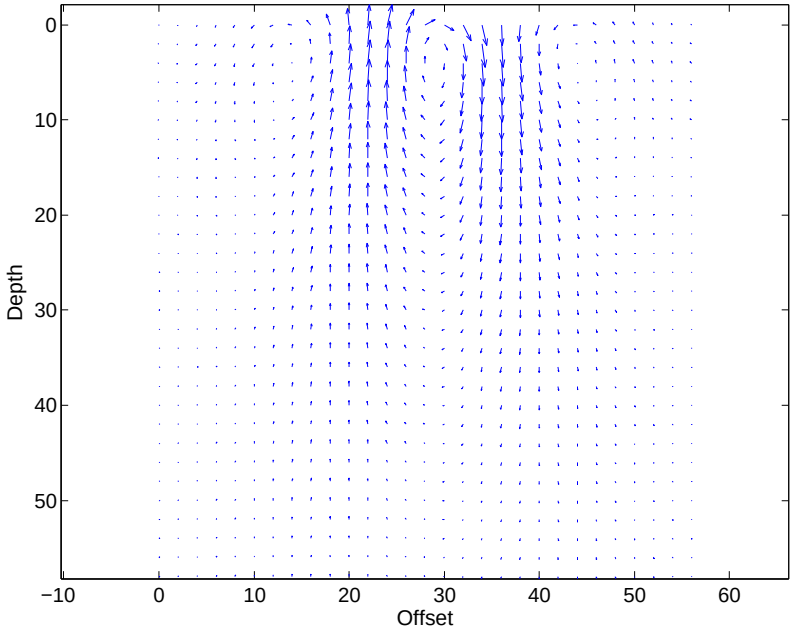

Figure 6.1: Quiver plot of an initial Rayleigh wave.

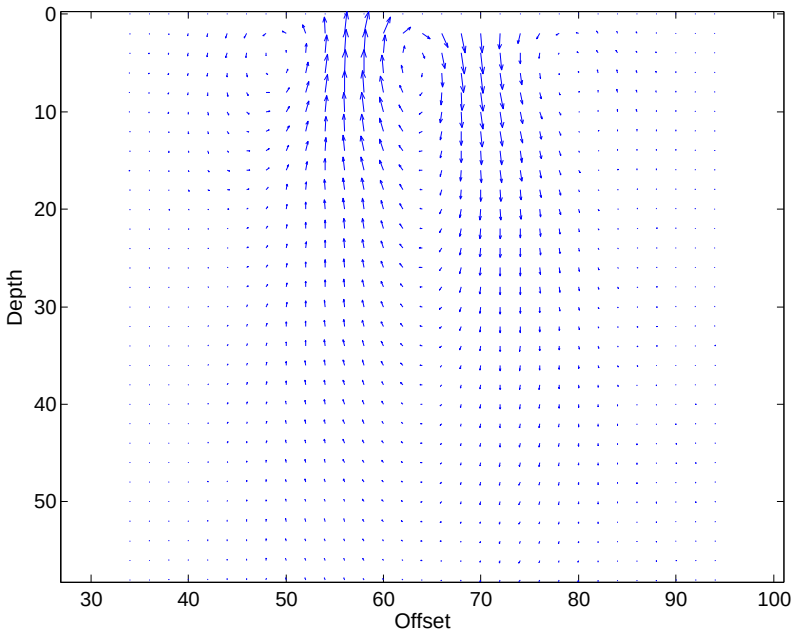

Figure 6.2: Quiver plot of a Rayleigh wave propagated through 60 steps. Notice how the wave form has been preserved.

P waves is $2857m/s$, for the S waves is $1000m/s$, and the density is $2g/cm^3$. The models modified from this half space all have the same density, and most have the S velocities multiplied by either 0.8 or 1.25. The exceptions are the models to show the relative influence of the compressional strength (as given by P wave velocity) where these velocities are multiplied by 0.8 or 1.2.

Figure 6.3 shows the wavelet propagating on the uniform half space. This is the base case and can be seen to have almost almost no change of wavelet character with time. The velocity of propagation is slightly less than the shear wave velocity, consistent with the Achenbach equation 6.1.

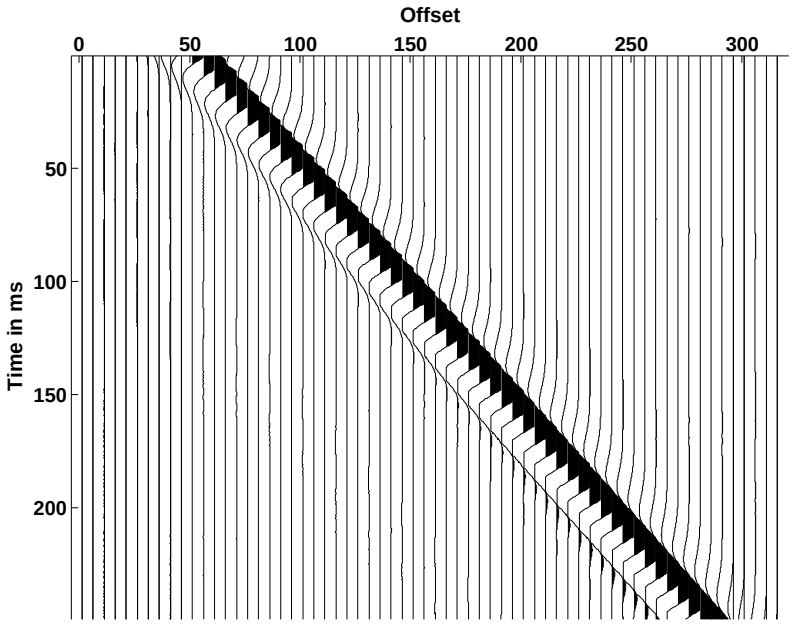

Figure 6.3: Surface vertical displacement of a Rayleigh wave on a uniform half space. The P wave velocity is $2857m/s$, the shear wave velocity $1000m/s$, and the density $2g/cm^3$. Δx is $1.25m$ and Δt is $0.3ms$. The dispersion can be seen to be minimal.

In Figure 6.4 the wave propagates into a material with lower velocity at all depths. A line marks the boundary. A small reflected wave propagates left and the

transmitted wave propagates more slowly to the right, undispersed.

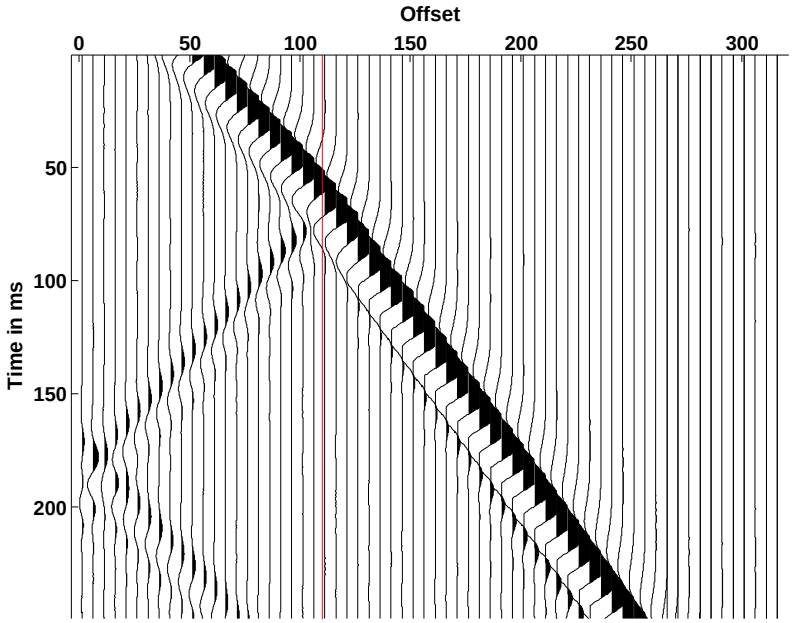

Figure 6.4: Rayleigh wave into a shear velocity zone which is 0.8 of the base case shear velocity. The zone is marked by the red line. There is an obvious reflection from the boundary, but there is still little dispersion.

The dispersive effects of layering on surface waves is shown in Figure 6.5 where the wave propagates into a low velocity layer 15 metres thick (the position marked by a box). The reflected wave and the first part of the transmitted wave are very similar to Figure 6.4, but then the low-speed portion of the wavelet receives interference from the higher-speed energy propagating below.

A thin low velocity zone with limited extent is shown in Figure 6.6. The wavelet is affected in a similar way to the wavelet in Figure 6.5, but the slight dispersion caused is then stable once it reaches the end of the zone.

A similar series of experiments with thin high velocity zones begin with Figure 6.7, where the case with great thickness is shown. The result is similar to Figure

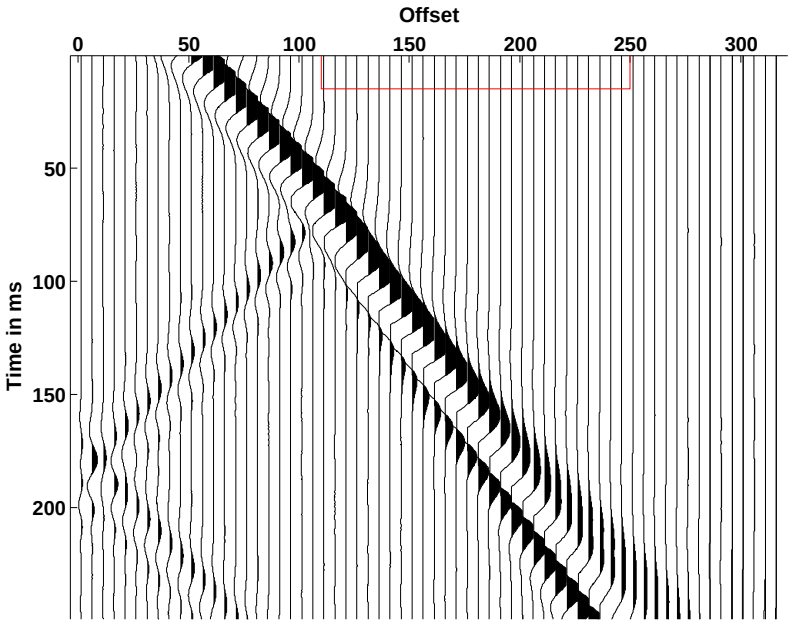

Figure 6.5: Rayleigh wave into a thin zone (15 metres) with the velocity 0.8 of the base case shear velocity. The energy of the wave is dispersed, with the deep part traveling at the base rate, and the shallow part more slowly. The reflection is quite similar to the previous case.

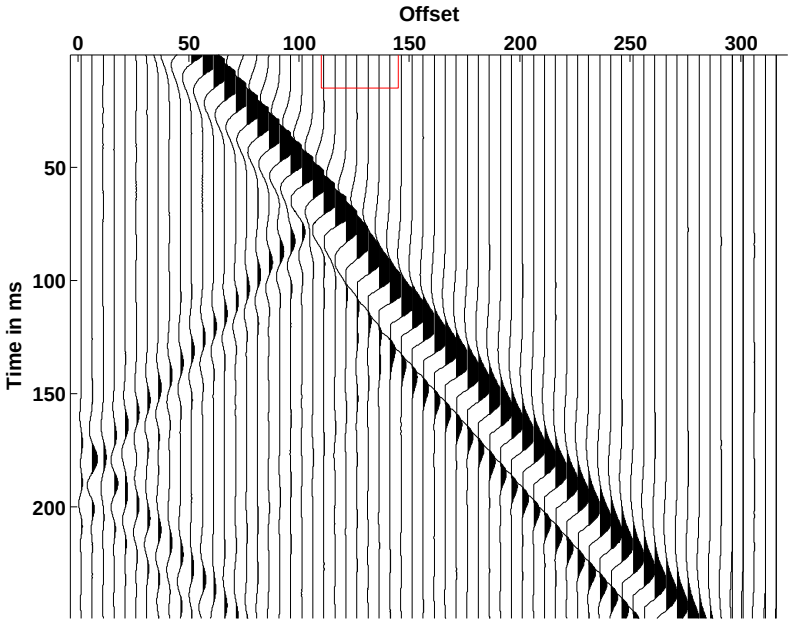

Figure 6.6: Rayleigh wave into a thin short lower velocity zone. This is similar to the previous case, but the dispersion has been quite limited.

6.4, but the reflection event has opposite polarity.

Wavelet propagation into a high velocity layered model is shown in Figure 6.8. The layer is thick enough (at 25 metres) to cause a small reflection, but causes only minor dispersion. There is a larger reflection from the end of the zone.

The wavelet propagation into the shorter zone in Figure 6.9 is similar to that in the previous Figure. Here, though, it is more clear that the reflection at the end of the zone, from high to low velocity, is significantly stronger.

Figure 6.10 shows the greater dispersion caused by a very thin low velocity layer. The low velocity zone here is 8 metres thick. Apparently a zone of this thickness splits the wavelet energy into two almost equal packages, because it appears in a cone spread from the high velocity ($1000 m/sec$) to the low velocity ($800 m/sec$).

The relative insensitivity of Rayleigh waves to compressional strength (or P wave

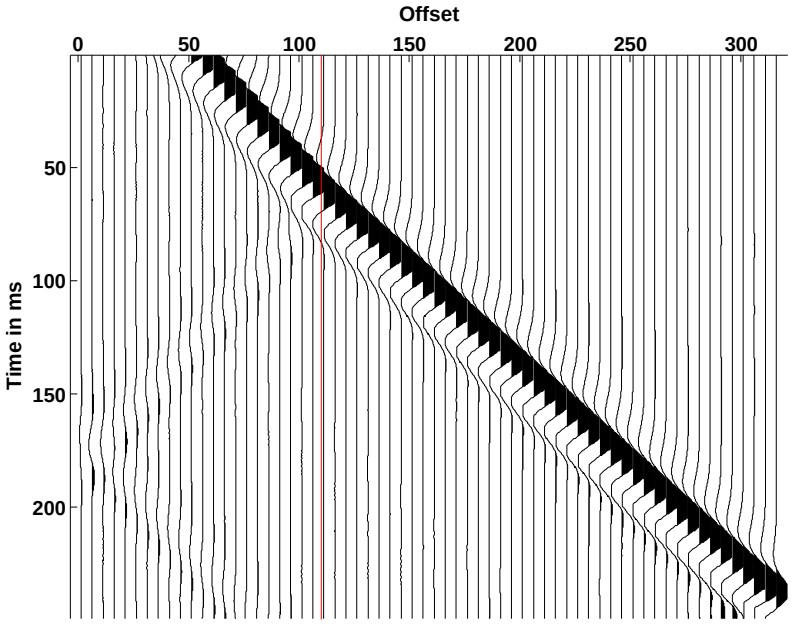

Figure 6.7: Rayleigh wave into a zone where the shear velocity is 1.25 times the base shear velocity. Similar to Figure 6.4, there is a reflection but little dispersion.

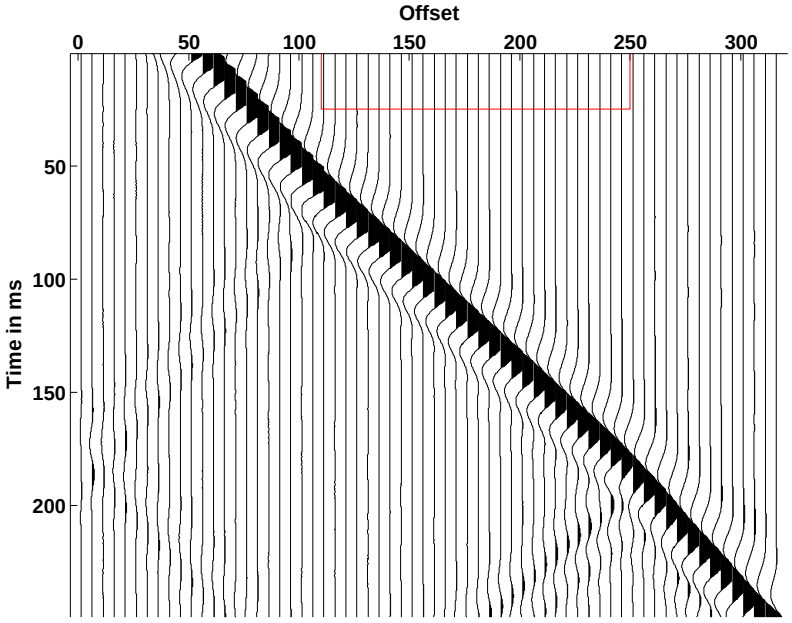

Figure 6.8: Rayleigh wave into a thin zone with the velocity 1.25 times higher. The thickness is 25 metres, but is plotted proportional to the time. There is a small reflection and not much dispersion.

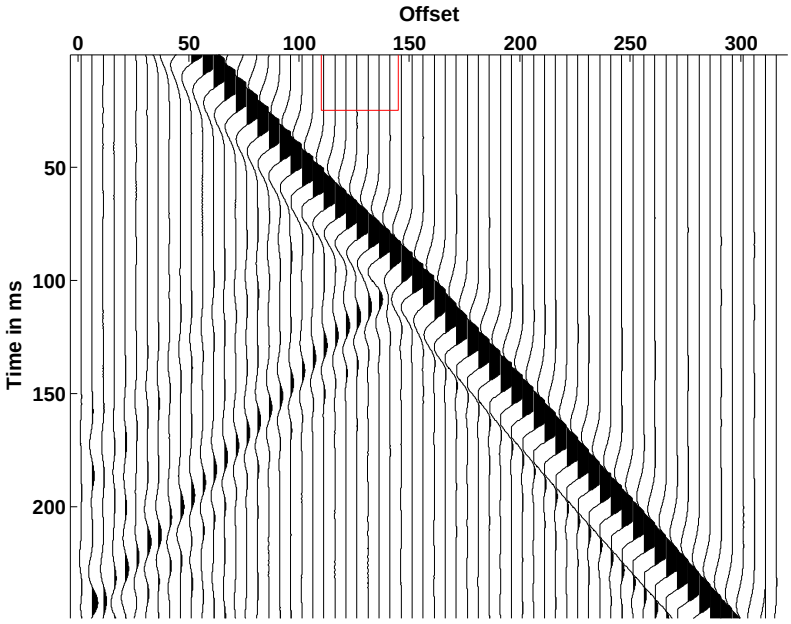

Figure 6.9: Rayleigh wave into a short thin higher velocity zone, similar to the previous case. The reflection at the end of the zone (high to low velocity) is stronger than that at the start (low to high velocity).

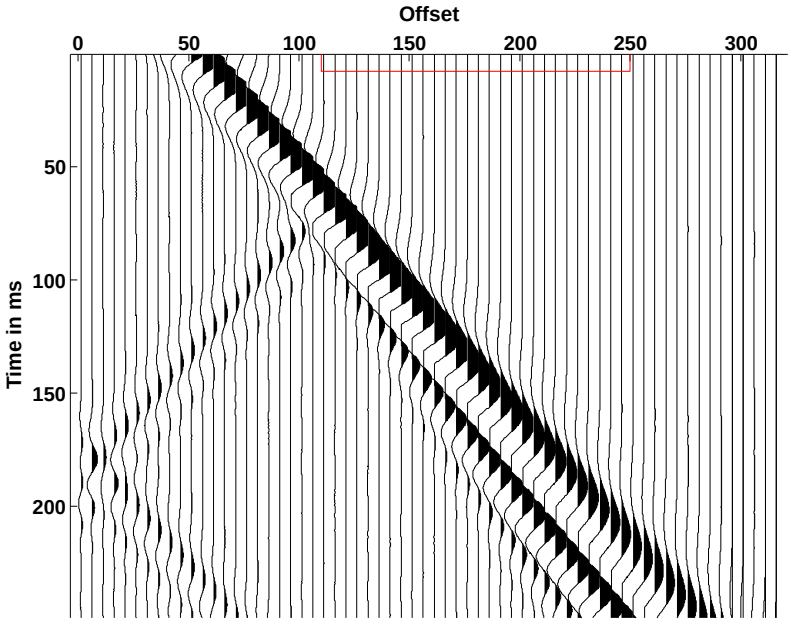

Figure 6.10: Rayleigh wave into a low velocity zone that is only 8 metres thick. The dispersion is much more obvious than in Figure 6.5.

velocity) is shown in Figure 6.11. Here the shear wave velocity is left constant, while the pressure wave velocity is reduced by 20 percent in the 8 metre zone. The minimal dispersion is obvious here, compared to the previous figure. The strong reflection at the end of the zone (from low to high velocities) is interesting.

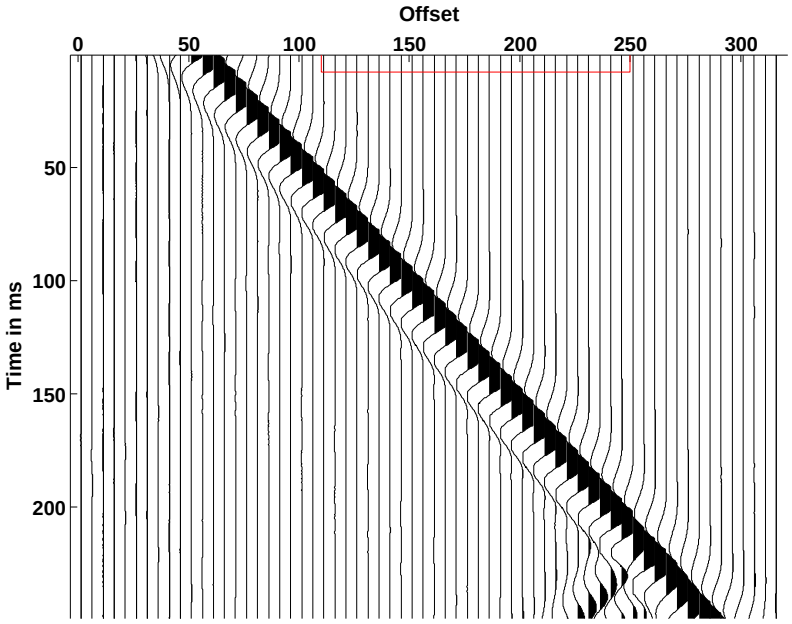

Figure 6.11: Rayleigh wave into a thin zone with only the P velocity lowered to 0.8 of the base case. Comparison with Figure 6.10 shows how the Rayleigh wave velocity has little dependence on compressional strength. A larger reflection at the low to high P wave velocity boundary is evident.

6.1.4 Conclusions

A Rayleigh wave that is compact in length can be used to reveal some significant general properties. Some simple rules may be stated, although the physics of the situation may be quite complex.

- A Rayleigh wave encountering a vertical impedance contrast tends to transmit

and reflect much as body waves do. The reflected and transmitted waveforms tend to be much like that of the incident wave, and the reflected and transmitted amplitudes are similar to those which plane body waves would have after an encounter with a similar velocity contrast.

- A Rayleigh wave encountering a shallow impedance contrast zone transmits and reflects in predictable ways. The reflected wave is lower in amplitude than a wave reflected from a vertical contrast. The transmitted energy splits into waves travelling at the background velocity and the thin layer velocity. The amplitudes and the amplitude attenuation of the two transmitted components depend on the layer thickness compared with the depth penetration of the Rayleigh wave.

6.2 The effect of some shallow conditions on seismic records

6.2.1 Introduction

This is a study of how several conditions in the near surface affect seismic recordings. The conditions studied are the depth of the energy source, and the near surface velocity structure. The effects compared are the amplitude of the first breaks, the amplitude of the ground roll, the frequency content of reflections, and the consistency of reflection wavelets. Finally, the polarity of the first breaks is compared to the polarity of the reflections, the main reason why this study was begun.

6.2.2 Method

The finite-difference modelling was done with the methods developed in this thesis, with the staggered grid, but without any correction factors for dispersion or stability. The records were all initiated with a simulated compressional source (as in Appendix G) on the symmetric edge (as in Appendix H) on the left of the model. The bottom of the model was perfectly rigid, and the reflection from it was used as the representation of a positive reflection coefficient. The right edge of the model had transparent boundary conditions (see Appendix H) and, with the sample rates used, were quite effective.

The seismic records were all recorded at the surface and displayed as standard WVA traces. Snapshots are associated with each seismic record, the time of the snapshot being near the time the P-wave energy was reflected from the bottom of the model. The snapshots are all displayed with the pressure wave/shear wave colour coding described in Appendix F.

6.2.3 Model parameters

The model parameters were realistic as metric units within the earth. The sample rates in the x and z directions were then at 1 metre, and the sample rate in time was 0.2 milliseconds. The basic velocities, used in the first models, were $1600m/s$ for pressure waves and $800m/s$ for shear waves. These were modified for later models to provide velocity steps and gradients, and these velocity profiles are shown in Figure 6.12.

All records have a 30 Hz zero-phase Ricker wavelet as a source signature. The resulting surface recordings are all from vertical geophones. The snapshots show

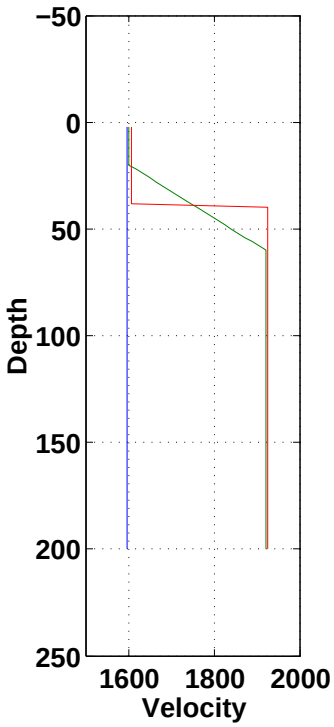

Figure 6.12: Compressional velocity profiles within models. The blue line is for the base cases at $1600 m/s$, the green line is for the velocity gradient cases, and the red line is for the velocity step cases. The shear velocities were half the compressional velocities in each case.

the form of the wavefronts within the earth, and they are identified with three main symbols: R for surface (Rayleigh) waves, P for pressure waves, and S for shear waves. The detailed codes are as follows: Pd for the direct pressure wave, Pr for the bottom reflected pressure wave (with ghost energy), Sg for the shear wave ghost off the surface, Scs for the the shear energy converted from the direct pressure wave at the surface, and Scr for the shear wave converted upon reflection from the bottom.

6.2.4 Model results

Case 1: The base model case has the energy source at 9 metres within a uniform velocity field, and the surface recording is shown in Figure 6.13. The zero-phase

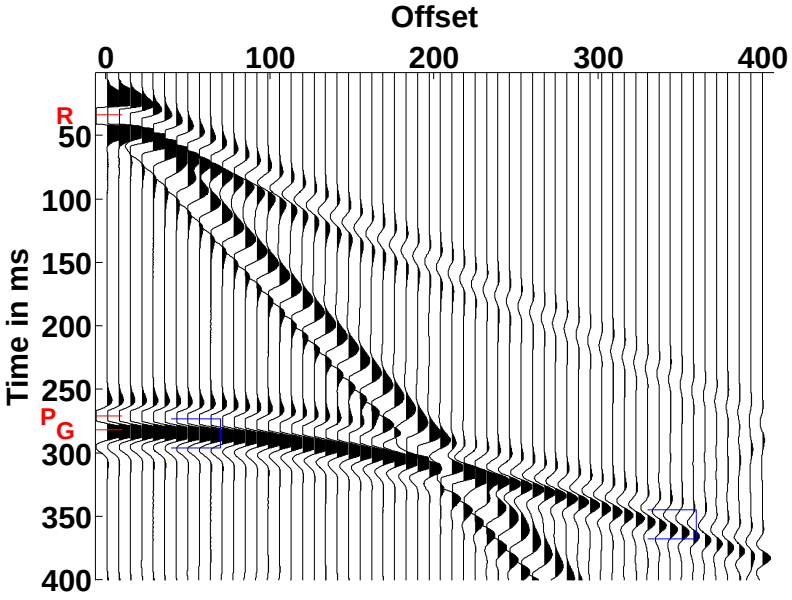

Figure 6.13: Surface record of case 1, basic model with 9m. source.

Ricker wavelet appears as a first break at zero offset (marked with an R). The reflection at 280ms can be seen as a combination of the primary wave at 275ms (marked P), and the ghost at 285ms (marked G). The two brackets have the same

width, and show that the effective length in time of the composite wavelet has not changed much from the near trace to an offset of $350m$.

A snapshot of this model at a time of 200 milliseconds is shown in Figure 6.14. The weak first breaks have reached about 270 metres offset. The compressional

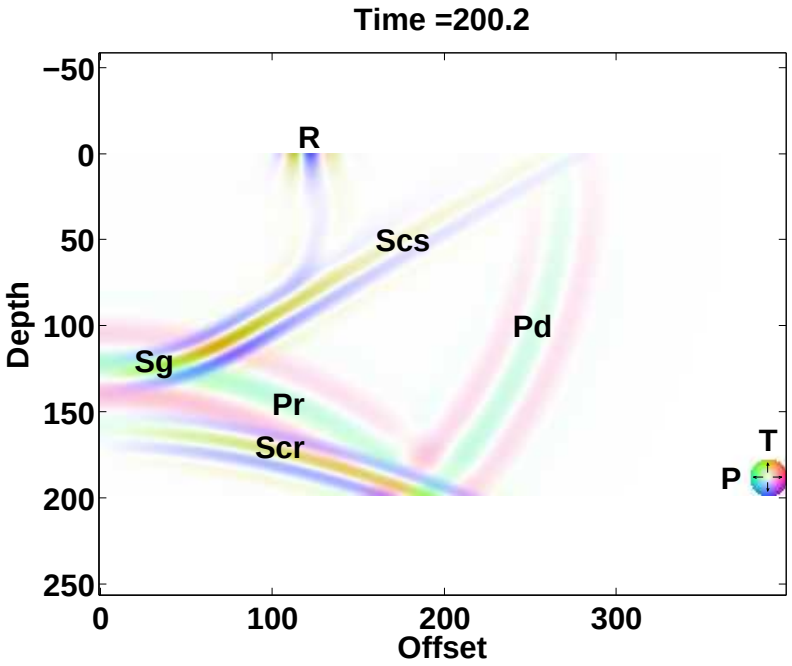

Figure 6.14: Snapshot of case 1, basic model with $9m$ source.

reflection Pr is propagating upwards.

Case 2: The second case is identical to the first except that the energy source is placed at 18 metres, and the surface recording is shown in Figure 6.15. At the left, the Ricker wavelet is again marked with an R, the primary reflection with a P, and the ghost reflection with a G. The primary then appears in less time, and the ghost at a later time. The advantage of this deeper shot is a reduced surface wave (ground roll). The disadvantage is that the greater separation of primary and ghost

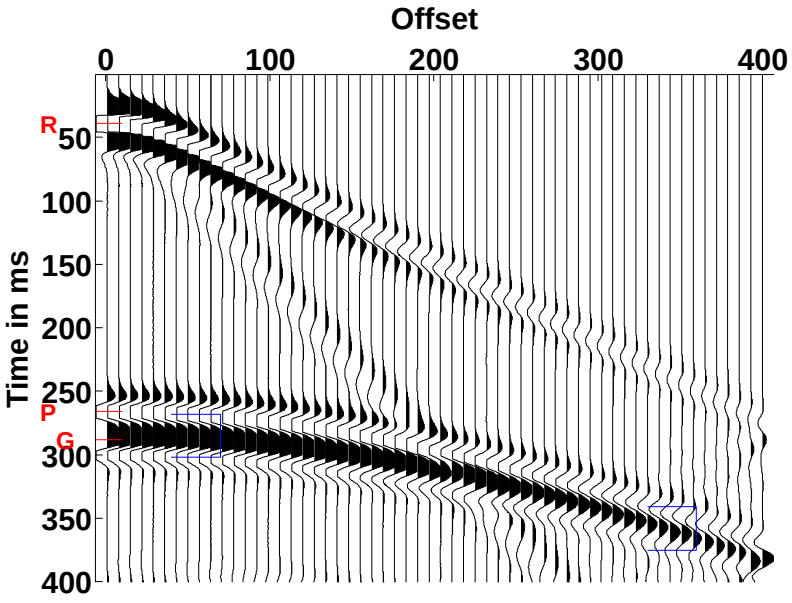

Figure 6.15: Surface record of case 2, basic model with $18m$ source.

reflections causes the composite reflection to have a lower frequency content, and this frequency content changes with offset. This can be seen from the shorter wavelength at the longer offsets for the primary/ghost wavelet (shown by the brackets). The change of frequency with offset shown here occurs along shallow reflectors, and the effect is reduced as the depth of the reflectors increase.

The effective change of frequency with offset can cause a significant degradation of statistical deconvolution results. The ghost is then not deconvolved except on near offset traces. A trace at a long offset will have an inconsistent set of frequency lowered reflections, ranging from minimum lowering at shallow times to the equivalent of zero offset lowering at deeper times. This inconsistency severely limits the effectiveness of deconvolution on these individual traces. A study of this effect with the real Blackfoot data can be seen in Hamarbitan and Margrave (2001)

Inspection of Figures 6.13 and 6.15 shows results that are consistent with the

standard polarity convention. The first break energy is plotted as a zero-phase trough, and the reflection from the positive impedance change (the bottom) is a close approximation to a zero-phase peak. The interacting mechanisms to explain this are quite complex, but an important part of the explanation is that the reflection wavelet combines a primary and a ghost.

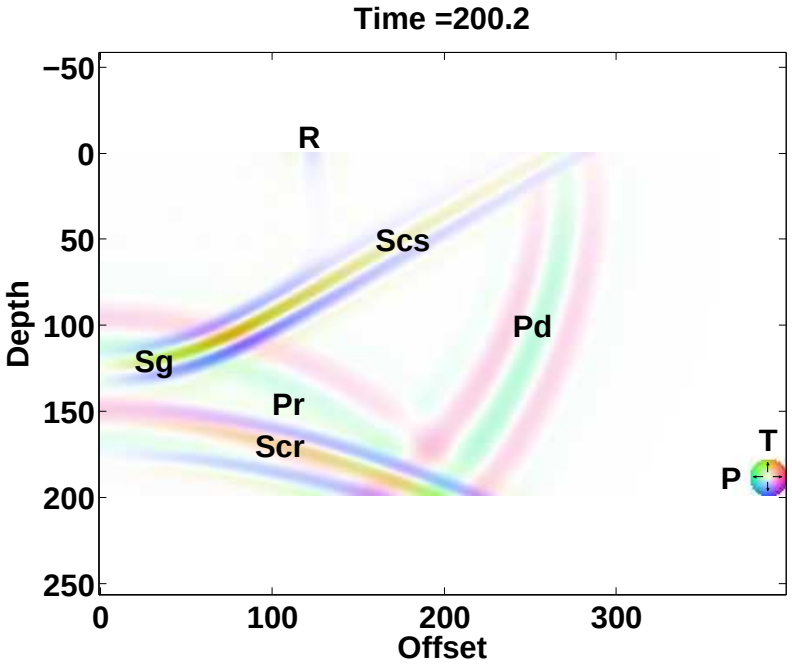

Figure 6.16: Snapshot of case 2, basic model with $18m$ source.

Case 3: This model has a source at 9 metres as in case 1, but has a velocity gradient of 1600 to $1920m/s$ over a depth range of 20 to 60 metres. This causes the raypaths and wavefronts to curve upwards and provides much more energy to the first breaks. The surface recording of this case is shown in Figure 6.17, and the snapshot is shown in Figure 6.18.

In the snapshot, the higher energy of the wavefront is shown by the higher colour

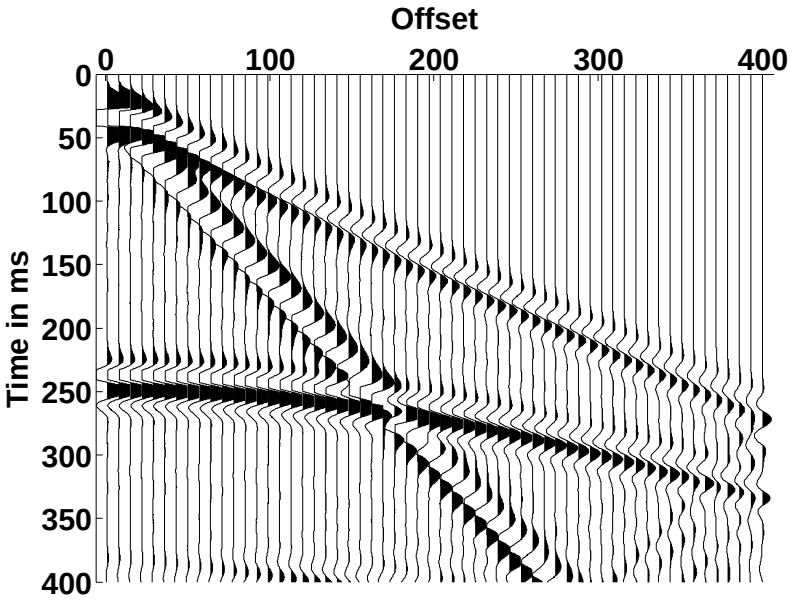

Figure 6.17: Surface record of case 3, gradient model with 9m. source.

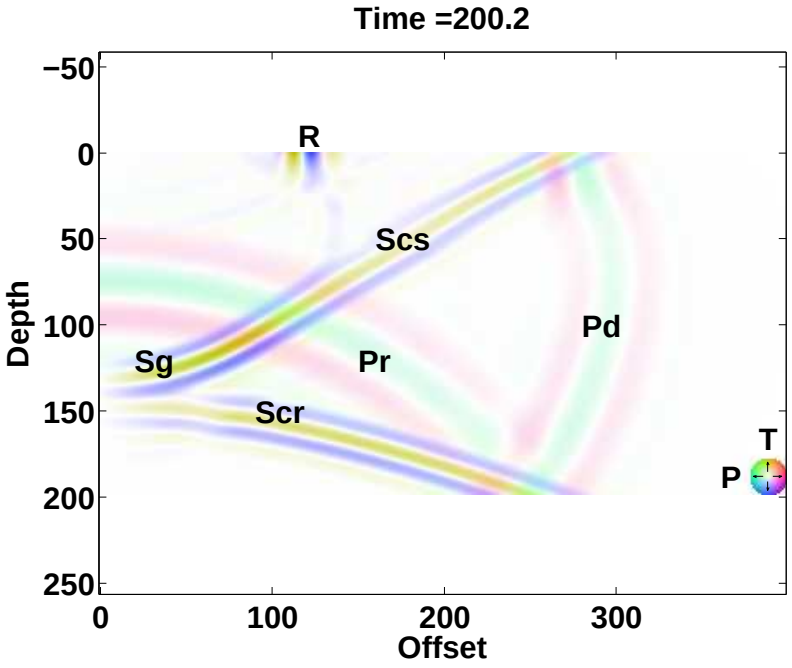

Figure 6.18: Snapshot of case 3, gradient model with 9m. source.

intensity (compared with Figure 6.14), and the greater component of energy in the vertical direction results in higher amplitude recording at the vertical geophones. The higher first break amplitudes at longer offsets is obvious in Figure 6.17. Close inspection shows a curve toward shorter times with longer offsets, also caused by the velocity gradient. Inspection also shows the first breaks starting to spread out, caused by energy arrival through more than one unique path.

Case 4: This model has the velocity gradient of case 3 and the 18 metre deep source of case 2. A surface recording is shown in Figure 6.19, and a snapshot in Figure 6.20.

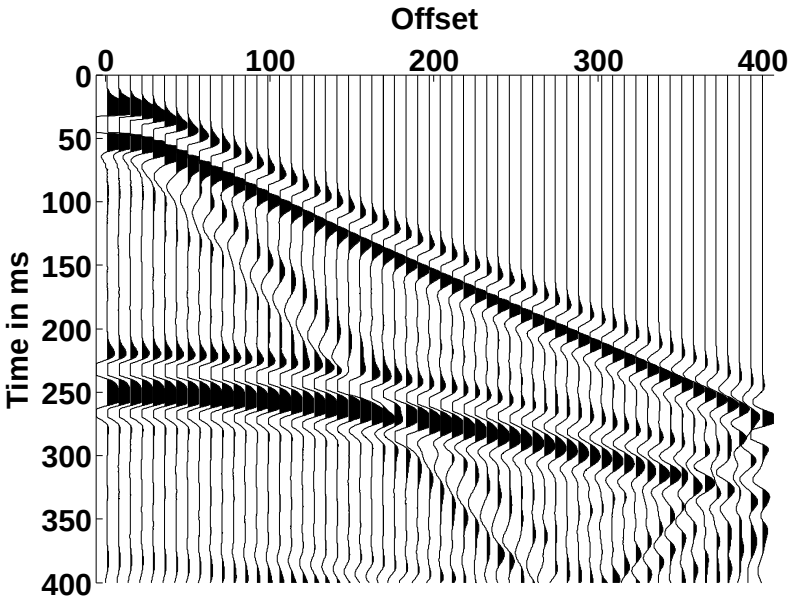

Figure 6.19: Surface record of case 4, gradient model with 18m source.

All the first break characteristics of case 3 can be seen here as well. The first breaks at longer offsets tend to be higher amplitude, more dispersed, and arrive at shorter times because of the velocity gradient.

Case 5: This model is similar to case 3 except that the velocity gradient was re-

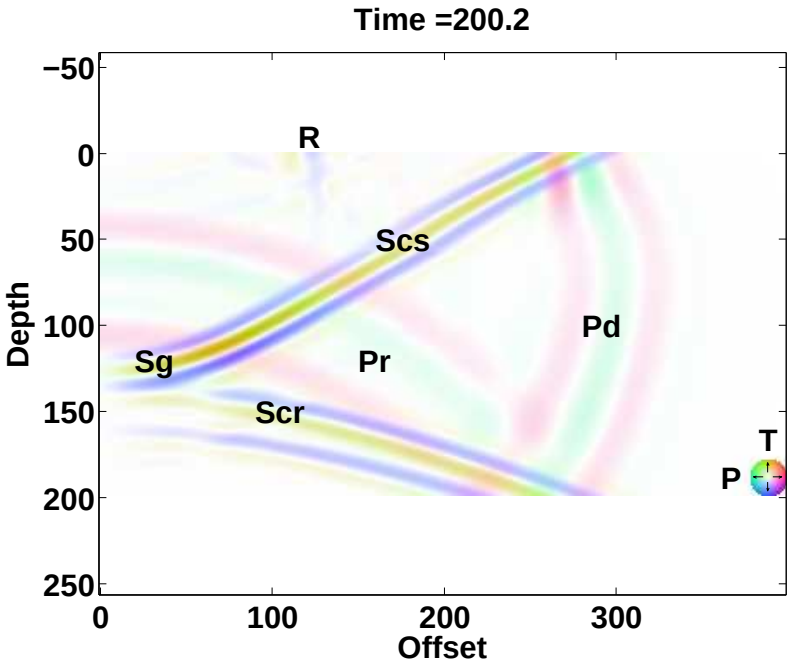

Figure 6.20: Snapshot of case 4, gradient model with $18m$ source.

placed by a velocity step, from 1600 to $1920m/s$ at 40 metres. This surface recording is shown in Figure 6.21, and the snapshot in Figure 6.22.

This case is included to show that while a smooth velocity gradient is most effective at curving energy paths toward the surface, stepped velocity increases have similar effects. This is a result of the tendency of wavefronts to heal themselves, and smooth out energy fluctuations.

Case 6: The model is the same as case 5, but with the source at 18 metres instead of 9 metres. This surface recording is shown in Figure 6.23, and the snapshot in Figure 6.24.

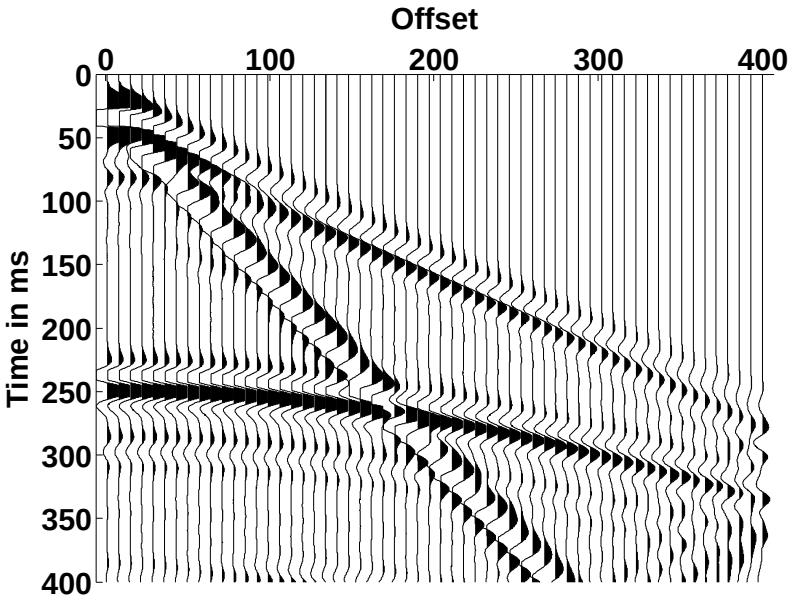

Figure 6.21: Surface record of case 5, step model with $9m$ source.

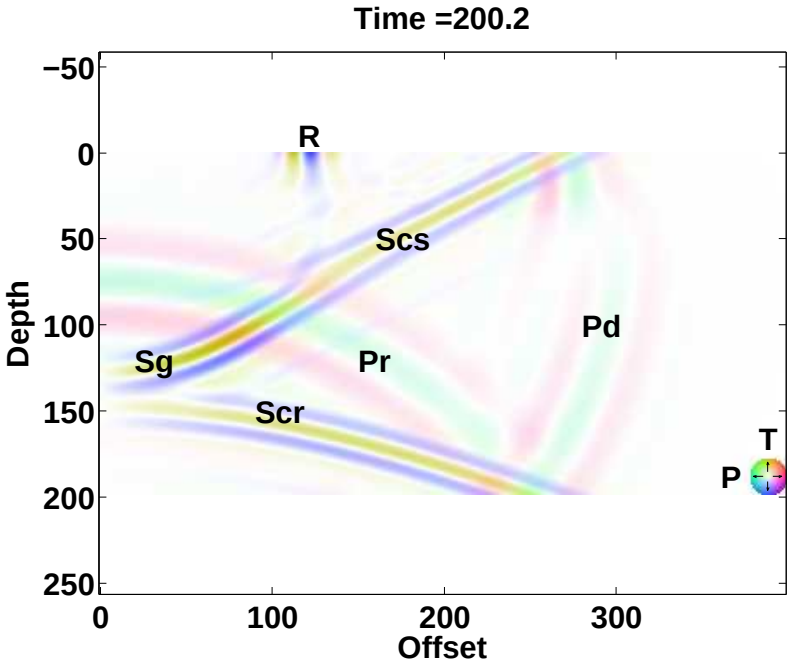

Figure 6.22: Snapshot of case 5, step model with $9m$ source.

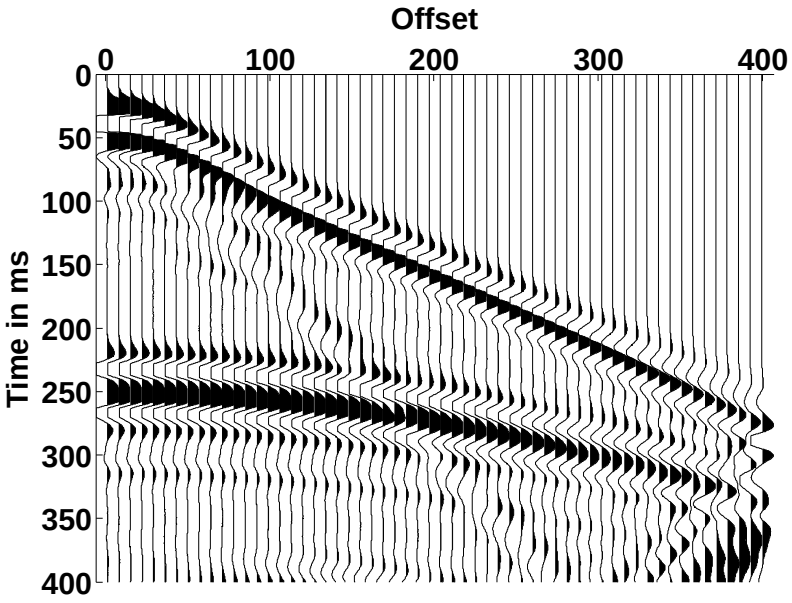

Figure 6.23: Surface record of case 6, step model with $18m$ source.

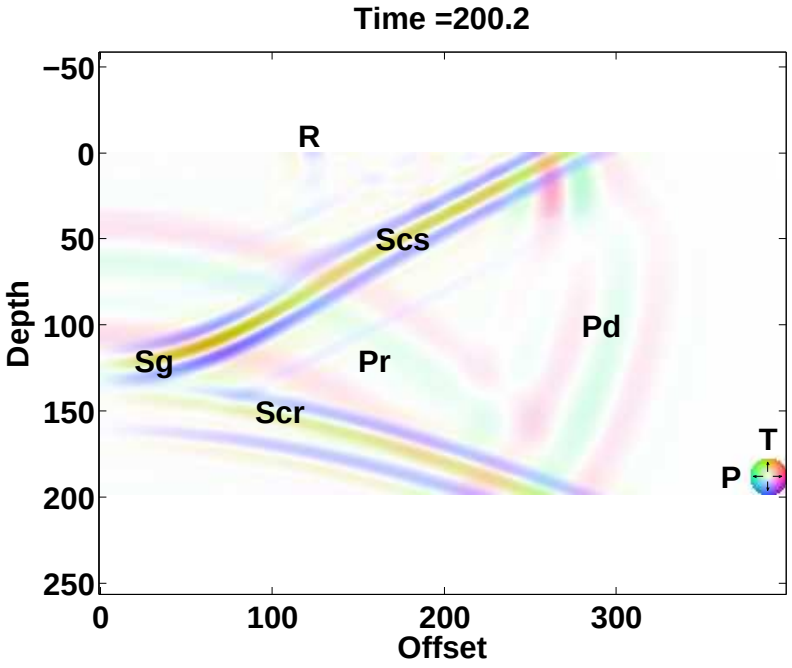

Figure 6.24: Snapshot of case 6, step model with $18m$ source.

6.2.5 Conclusions

Finite-difference modelling with an accurate free surface representation can give insight into the relationship of the conventional reflections caused by body waves, and the waves caused by boundaries, like first breaks and ground roll. In particular:

1. A seismic processing industry convention states that, to display positive reflections as peaks, the first breaks must be plotted as troughs. The particular models run here confirm that relationship, although the reasons for it are quite complex.

2. Deep sources (for example at 18 metres) cause reflected events to have a significantly broader, or lower frequency, character. This character change is reduced with shallower reflections at longer offsets, and so may not be possible to correct with deconvolution.

3. The amplitude of ground roll and first breaks can be related to the depth of shot and the near surface velocity profile. Ground roll is stronger from shallow shots. First break energy from deeper shots is persistent to longer offsets, and also arrives earlier, and has higher amplitudes at longer offsets. These same properties can be found where there is a strong near surface velocity gradient.

6.3 Models of standard AVO reflections with realistic initiation

6.3.1 Introduction

The typical types of AVO responses are based on the Geophysics paper by Rutherford and Williams (1989), who presented what they called three classes of responses from gas sands. These were called high-impedance contrast sands, near zero contrast sands, and low contrast sands. An additional class was later added by Castagna et al. (1998), of a porous sand overlain by a high velocity unit, to get what is now almost a standard set of four classes.

Work has continued on AVO responses of these classic types and others, with more generalized conditions and fewer restrictions. These papers generally assume that the superposition of plane waves at the reflecting interface is sufficient to characterize the reflected and transmitted amplitudes. This assumption is the basis for use of the Zoeppritz equation, where five plane waves (incident, reflected P and S, transmitted P and S) are expected to intersect with the same phase at all points along a reflector. It is not difficult to show, as will be shown here, that this is not the case. This is because, although the processes of reflection and transmission do create waves with predictable results in the vicinity of the reflector, away from the reflector the waves are created and then propagated from past conditions. In general the resulting waves are not plane waves, and the portions of these waves near the reflector do not take the direction in space that plane waves would take.

Details of the wavefronts for the case of AVO class 1 will be shown here, followed by the surface records from this model, and the plots of trace amplitudes. Only the

amplitude plots will be shown for the other AVO classes.

6.3.2 Model parameters

Class	AVO 1	AVO 2	AVO 3	AVO 4
α_1	2000	2000	2000	2000
β_1	879.9	879.9	879.9	1000
ρ_1	2.4	2.4	2.4	2.4
α_2	2933	2400	1964	1599
β_2	1882	1540	1260	654.3
ρ_2	2.0	2.0	2.0	2.456

Table 6.1: The AVO classes. The velocities (in m/s) and densities (in g/cm^3) for the layer above the reflecting interface (1), and below (2).

The parameters used to model each AVO class are shown in Table 6.3.2. The interface with the impedance contrasts listed in Table 6.3.2 was placed at 740 metres, and an explosive P-wave source was initiated at a depth of 19 metres. Surface displacements were measured from the source at 0, to 1900 metres. Recording was continued until at least some of the shear wave energy reached the surface.

The finite-difference models all used a spatial sample rate of 2.4 metres, and a time sample rate of .0005 seconds. Each model was initiated at the centre of a symmetric medium, of which only the right half is shown. The right boundary was absorbing, and the bottom boundary (at 1200 metres) was rigid. The initiating pulse was a 30 Hz Ricker wavelet.

6.3.3 Model results

A snapshot of the AVO class 1 wavefields at a time of 0.575 seconds is shown in Figure 6.25. The time was chosen to be near the crossover point (zero amplitude)

for the P-wave reflection. The five short straight lines on the interface are the angles of the wavefronts (supposed by a Zoeppritz program) for the offset at their centre. The centre point here is called the quintuple point.

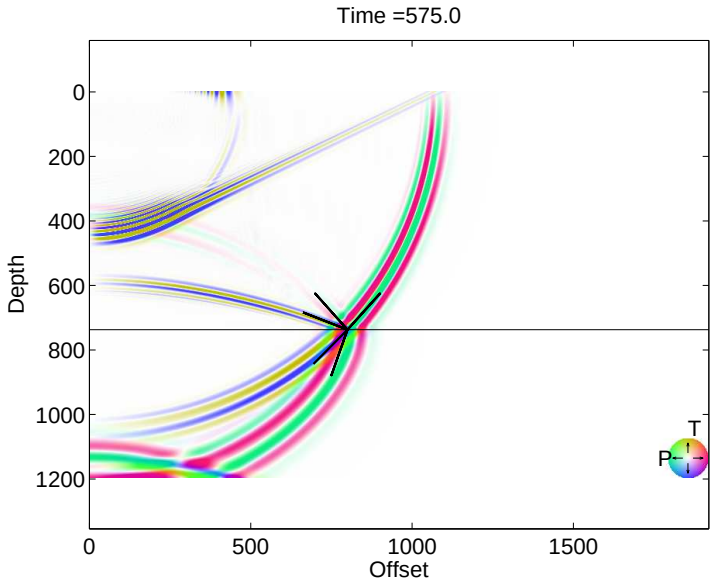

Figure 6.25: AVO 1 snapshot near time of minimum P-wave reflection. The angles which the five wavefronts are assumed to take (within a Zoeppritz program) are indicated with short black lines.

Figure 6.25 has a zoomed in version in Figure 6.26, and the relationships between the quintuple point angles and the actual wavefronts is more obvious. The theoretical angle is a reasonable match for the incident wavefront (to the NE). The reflected P wavefront (to the NW) is difficult to distinguish because the amplitude is so low, but looks like a reasonable match to the diagram. Both of the shear wavefronts (reflected and transmitted) have the proper angles, but are noticeably lagged. The transmitted P wavefront (to South and a bit West) shows the largest deviation, with a lead over the theoretical. Also, the actual direction which the waveform takes at the interface is curled around, and even facing a bit North of East.

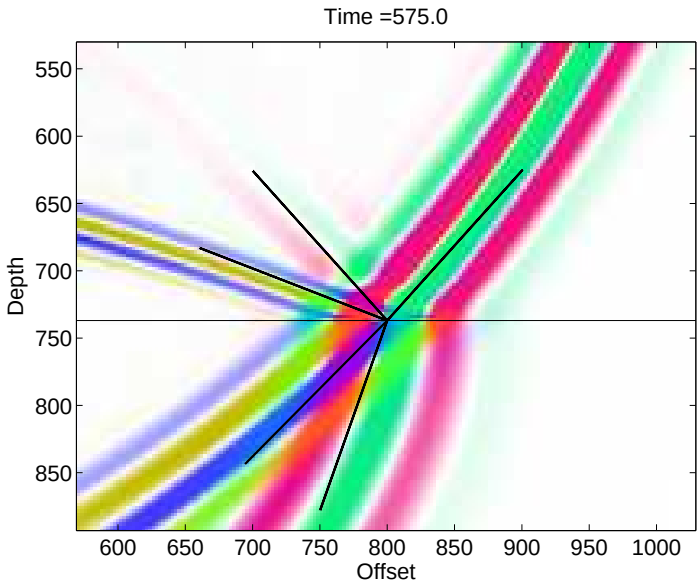

Figure 6.26: A blowup of Figure 6.25, at the point along the interface where the wave conversions from incident to transmitted and reflected is taking place. The black lines show the theoretical directions which the wavefronts should have.

The vertical displacement record at the surface of the model is shown in Figure 6.27. The reflected P wave has a zero offset time of 0.780 seconds, and it can be seen to have a polarity reversal. The converted wave has a much steeper slope. It has zero amplitude at zero offset, but could be extended to zero offset at approximately 1.230 seconds. it may be seen much more clearly in Figure 6.29.

The amplitude of the reflected P wave is plotted in Figure 6.28. The theoretical amplitudes from the Zoeppritz program are the two curves plotted in black, one the negative of the other, and showing the polarity reversal expected for AVO case 1. The amplitudes from the finite-difference program are plotted in two colours, blue for the maximum positive amplitudes, and red for the minimum negative amplitudes. The low amplitude zone is so wide that it is difficult to trace a reflection running from a peak into a trough, but the general trend certainly fits into that form. The

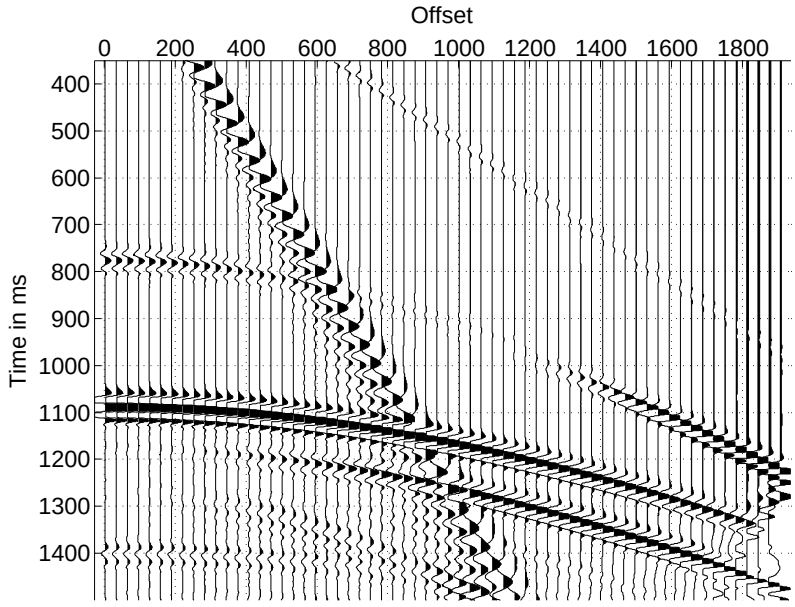

Figure 6.27: Type 1 AVO response, vertical component. The pressure wave reflection at zero offset appears at time $780ms$. Note the amplitude fadeout and then reversal.

intersecting ground roll energy creates the high amplitude events at about 650 metres.

The horizontal displacement at the surface is shown in Figure 6.29, and is the complement to Figure 6.27. The P wave has very low amplitude until longer offsets are reached, but the converted shear wave is much higher amplitude than on the vertical recording.

The amplitude of the converted shear wave is plotted in Figure 6.30. The plot in this case is the maximum vector amplitude calculated from the vertical and horizontal displacements, with the polarity of the horizontal component. This procedure usually provides a plot with less noise interference, and should match the Zoeppritz program output more closely.

The amplitude of a pressure wave reflected from an AVO class 2 interface is shown

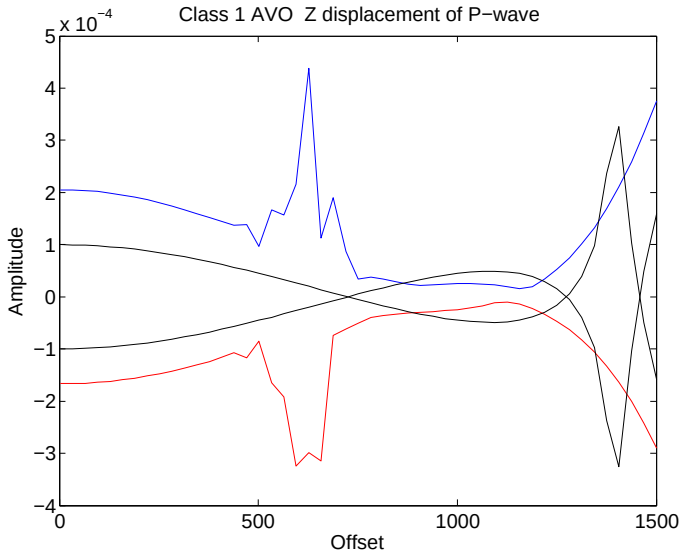

Figure 6.28: Type 1 AVO response, Z-component of P-wave. Blue is positive, red is negative. The Zoeppritz curve is repeated with opposite sign for comparisons. Ground roll energy appears at $650m$.

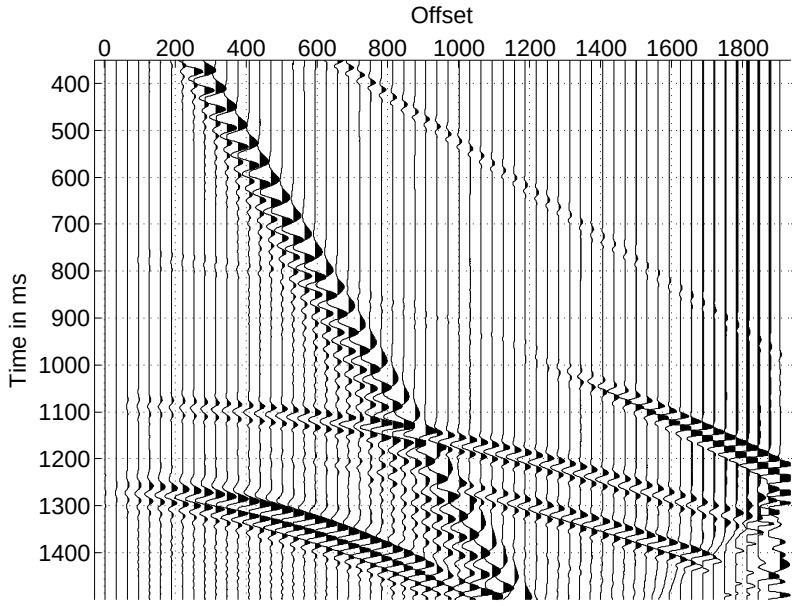

Figure 6.29: Type 1 AVO response, horizontal component. The converted shear wave reflection at zero offset projects to about $1270ms$.

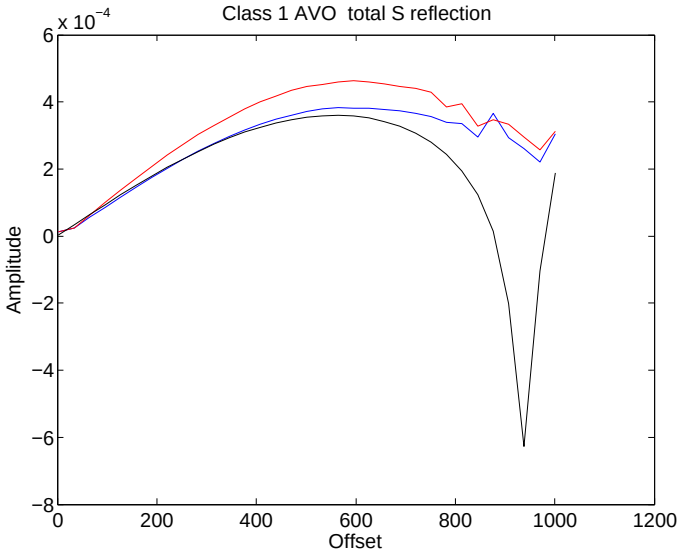

Figure 6.30: Type 1 AVO response, total S-wave. Peaks and troughs are plotted positive. The Zoeppritz curve is black.

in Figure 6.31. This curve and most of those following plot the maximum vector amplitude as with Figure 6.30.

Figures 6.32, 6.34, and 6.36 show the converted shear wave reflection amplitudes for the AVO cases of 2, 3, and 4 respectively. For cases 2 and 4, the vector form of input data were used, while for case 3, the X-displacement data were used. For this case, the Z-component data had severe interference.

Figure 6.33 and Figure 6.35 show the reflected pressure waves for AVO cases 3 and 4 respectively. Both of these used the vector form of input data.

6.3.4 Discussion of the model results

In Figure 6.26, comparison of the position and orientation of the modelling wavefronts with those assumed for Zoeppritz calculations shows one of the limitations of the Zoeppritz method. In general, if the velocities of the lower medium are sig-

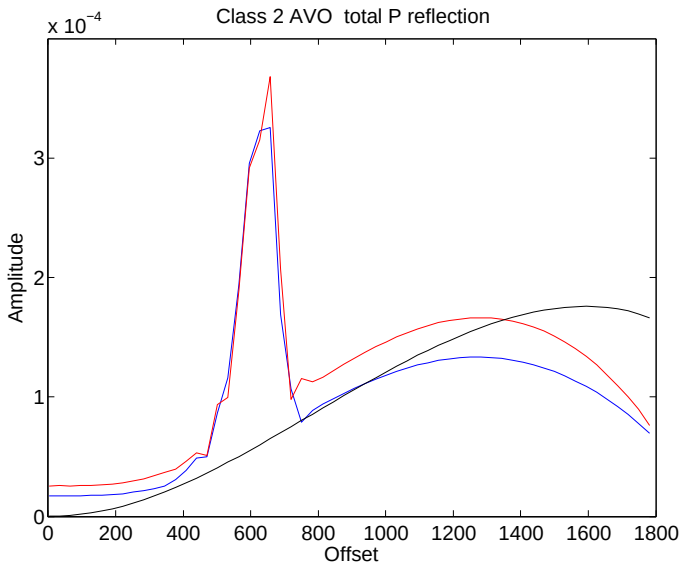

Figure 6.31: Type 2 AVO response, total P-wave. Peaks and troughs are coloured, the Zoeppritz curve is black. The high amplitude points are ground roll.

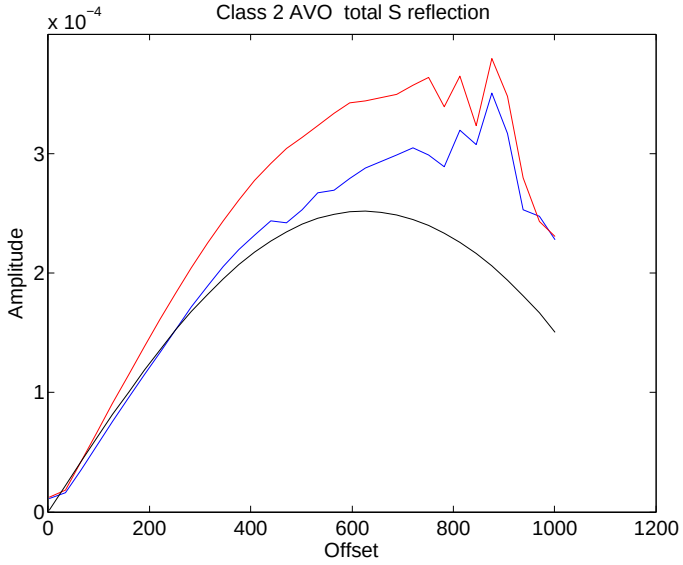

Figure 6.32: Type 2 AVO response, total S-wave, with the same colours. Ground roll starts at $1000m$.

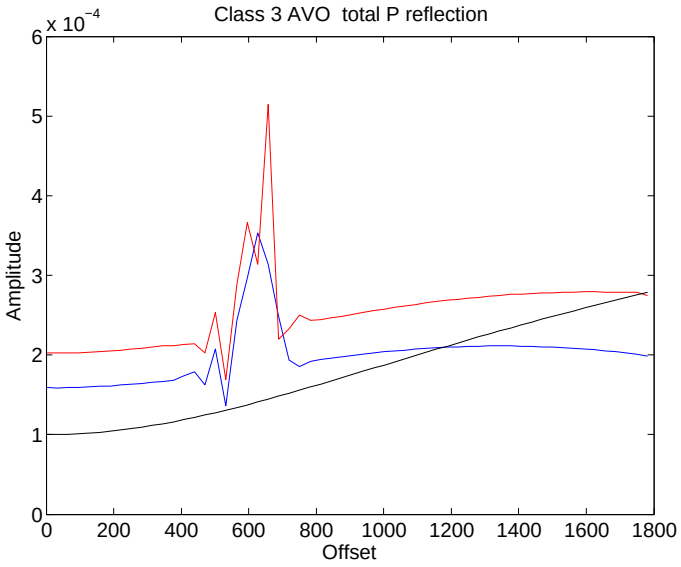

Figure 6.33: Type 3 AVO response, total P-wave. The high amplitude spikes are ground roll.

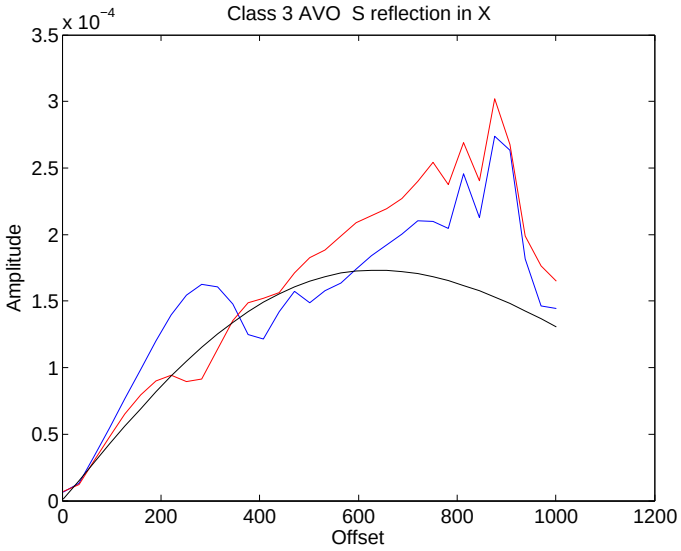

Figure 6.34: Type 3 AVO response, S-wave X component only. Another reflection interferes at $250m$.

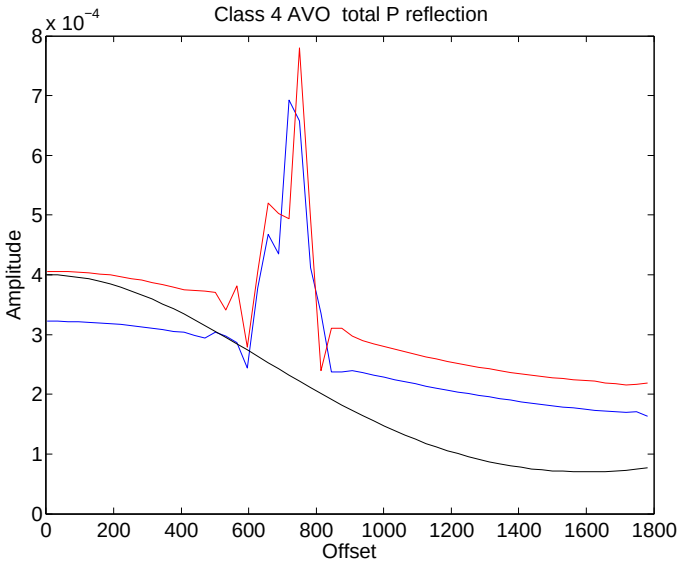

Figure 6.35: Type 4 AVO response, total P-wave. Ground roll is at $750m$.

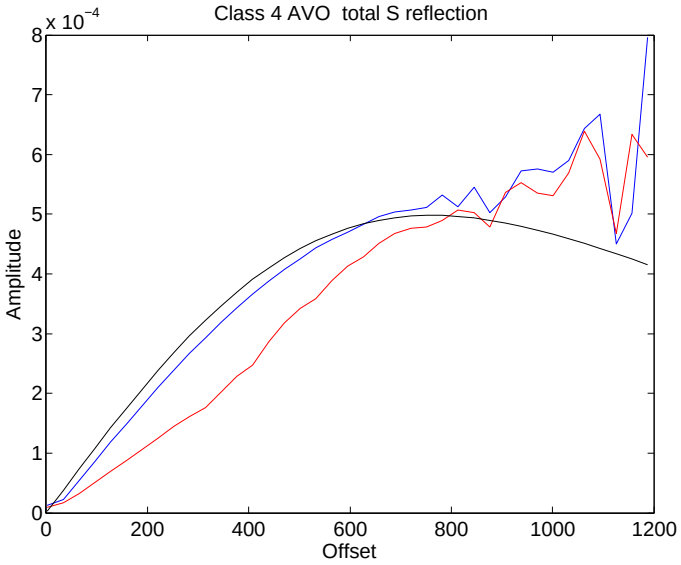

Figure 6.36: Type 4 AVO response, total S-wave. The end amplitudes are distorted by another reflector.

nificantly higher than those in the upper medium, as the lower wavefront becomes more perpendicular to the interface it will tend to outpace the quintuple point. The wavefronts will tend to heal, but take the wrong angles. Eventually the wavefront below the interface will break contact with the other waves and become a head wave. This can happen very soon after the critical point.

The finite-difference modelling and the Zoeppritz programs show similar trends in most cases. For AVO case 1, the converted wave responses are almost identical, and the pressure wave responses show similar polarity reversals, although not at quite the same places. The other AVO cases show that the trends of the modelling and Zoeppritz results are similar. In conditions where the zero offset reflectivity is zero (for case 2 and all the converted waves), the two types of curves may be matched quite closely.

There are some general observations that may be made about the amplitude plots. Sharp features (at critical angles) are smoothed through with the finite-difference versions. The high points are often shifted between the two versions, but the causes are uncertain.

6.3.5 Conclusions

Finite-difference modelling has confirmed that Zoeppritz programs may make reasonable estimates of the amplitude variations with offset of the classic gas sand interfaces. However, the results differ in the details, and especially where velocity contrasts are high, the Zoeppritz results may be misleading anywhere past the critical point.

Chapter 7

Conclusions

This thesis is a study of finite-difference modelling in one and two dimensions. It concentrates on several novel methods which can improve finite-difference results. There are also some finite-difference models included which illustrate some interesting aspects of exploration seismic interpretation.

Correction multiplier for finite-difference time stepping in one spatial dimension

This method requires the application of a multiplicative correction to each frequency of the acceleration calculated by an elementary finite-difference algorithm, a factor which is the ratio of two sinc functions squared. The equation with correction is

$$\phi(x,t+\Delta t,k) = \left[2 + (\Delta t)^2 v^2 \frac{sinc^2(\frac{kv\Delta t}{2})}{sinc^2(\frac{k\Delta x}{2})} D_x^2\right] \phi(x,t,k) - \phi(x,t-\Delta t,k), \quad (7.1)$$

which is a duplicate of equation 2.18. It compares with the most elementary finite-difference equation which may be written as

$$\phi(x,t+\Delta t,k) = \left[2 + (\Delta t)^2 v^2 D_x^2\right] \phi(x,t,k) - \phi(x,t-\Delta t,k). \quad (7.2)$$

These comments apply to the corrected equation:

- The equation is exact, and propagates a wave exactly as an analytic equation would when the wave is sampled over sufficient length. However, it applies within an infinite medium with uniform properties, and only for a monochromatic (single wavenumber) signal.

- The method may be extendeded to polychromatic (many wavenumber) signals by Fourier transforming the wave from space into wavenumbers, multiplying each wavenumber by the appropriate correction, and transforming back into space. The time-stepping is then done.

- This equation has been used before, but as far as is known, only for single frequencies/wavenumbers (Cole, 1998). For this case no transforms are required.

- A correction consisting of just the denominator of this correction factor, but for all frequencies, is equivalent to the pseudo-spectral method. This method was developed by Kreiss and Oliger (1972).

- Models using this method show improved wave propagation.

- The equation may be analyzed to show how the flaws of uncorrected wave propagation may be quantified. That is, an explicit formula for the velocity dispersion results.

- Part of the explanation for the drastic results of modelling with unstable parameters is the fact that wavenumbers are generated that can not be propagated because they are aliased in time. This explains why the unstable effects tend to be local.

- Even an inherently unstable model may be usable with this correction multiplier.

The correction multiplier replaced by the correction filter in space

The second novel method developed in this thesis is the transform of the Fourier domain correction multiplier to the relatively short spatial domain correction filter. The direct way to do this is an inverse transform of the correction multiplier, but this leads to a filter which is essentially infinite in length. Here, the filter is the optimum inverse of the forward Fourier transform, but a transform which calculates only the wavenumbers below a given 'high cut' wavenumber. These comments on the optimum correction filter apply:

- These optimum filters can have very beneficial effects even with only a few points (e.g. 5 points).
- The 'high cut' wavenumber replaces the former criterion 'minimum samples per wavelength'.
- With inherently stable parameters ($\Delta t < \frac{\Delta x}{v}$) the wavenumbers above the design top are attenuated, and don't interfere with anything in the signal band.
- With inherently unstable parameters ($\Delta t > \frac{\Delta x}{v}$) a special design procedure is required. An alternative sampling procedure, where the sample values are taken one-half a sample distance from their normal positions, is one method of achieving this.

Correction multiplier for elastic-wave finite-difference time stepping in two spatial dimensions

This third method uses the style of correction multiplier developed for one dimension, but adapts it to the differential equation pair describing elastic wave propagation in two spatial dimensions. Most of the terms for these equations require

corrections which are easily related to the corrections of the one dimensional case. The term with partial derivatives in both x and z has a correction which is not immediately obvious, but turns out to have an easily calculated form. The following points are of interest:

- The theory applies to both P and S waves of all frequencies.
- The theory applies at all angles, and so wave propagation is consistent in the grid directions, and in particular at 45 degrees from the grid directions.
- Tests show that wave propagation is often most accurate at 45 degrees to the grid, and so in these directions the corrections are minimal compared to the corrections along the grid directions.
- Five unique correction terms are required for the different terms of the equation. There are six terms between the two equations, but the two cross terms turn out to have the same correction.

The correction multipliers replaced by correction filters in space

The fourth method designs two dimensional spatial correction filters to approximate the effect of the correction multipliers. This procedure is closely related to the method used for the one dimensional filters. It requires the optimization of the inverse Fourier transform which has a cut-off high wavenumber response. Observations similar to the one spatial dimensional case may be made here also:

- The optimal filters can have very beneficial effects even though quite small spatially.

- With stable parameters, the highest wavenumbers are attenuated.
- Tests show improved wave propagation compared to the well known Levander (1988) scheme, even when limited to the same filter sizes.

The transmitting boundary by specification of precise external displacements

This method relates the displacement at a projected point across a transmitting boundary with the direction of energy flow at the boundary. This can be done by supplementing the wave equation with the eikonal equation. The displacement at each external point can then be chosen so no energy is reflected back into the model. The solutions here are limited by the accuracy of the equations (as yet uncorrected) and the model corners (where two types of boundary conditions must be satisfied).

Practical Rayleigh wave reflection and transmission properties

A Rayleigh wave that is compact in length can be used to reveal some significant general properties.

- A Rayleigh wave encountering a vertical impedance contrast tends to transmit and reflect much as body waves do, with a preservation of wave form and with similar relative amplitudes.
- A Rayleigh wave encountering a shallow impedance contrast zone transmits and reflects in predictable ways. The reflected wave is lower amplitude than a wave reflected from a vertical contrast. The transmitted energy splits into waves travelling at the background velocity and the contrast zone velocity. The amplitudes of the two transmitted components depend on the zone thickness compared with the depth of the Rayleigh wave.

The effects of shallow conditions on body waves

Finite-difference models can show how deep body waves relate to the free surface, to shallow conditions of the earth, and to source depth.

- Body wave reflection character, and especially offset dependent reflection character, can be related to the depth of shot. Deep shots can generate ghosts with strong effects in the seismic frequency range, generally making the wavelet lower frequency. However, the effect is not consistent, with shallower reflections at longer offsets being less affected.

- The amplitude of ground roll and first breaks can be related to the depth of shot and the near surface velocity profile. Ground roll is stronger from shallow shots. First break energy from deeper shots is persistent to longer offsets, and also persistent where there is a strong near surface velocity gradient.

- The polarity of body waves may be related to the apparent direction of first breaks. It is shown that if the initial deflection of the first breaks are plotted as troughs, then positive reflections will appear as peaks.

Finite-difference studies may contribute to understanding of AVO effects

The quantification of AVO effects can sometimes be made more realistic by including finite-difference studies. This has been found in a case of an AVO of type 1, where the wave fronts did not conform to the Zoeppritz assumption of the incident wave coinciding with the two transmitted and two reflected waves. The disconnect is most pronounced in the case of the transmitted P wave, where the front energy can be largely from a head wave.

Bibliography

Abramowitz, M., and Stegun, I. A., 1965, Handbook of Mathetical Functions: Dover Publications Inc., New York, first edn.

Achenbach, J. D., 1973, Wave propagation in elastic solids: North-Holland Publishing Co., New York, first edn.

Aki, K., and Richards, P. G., 1980, Quantitative Seismology: W.H. Freeman and Co., first edn.

Ames, W. F., 1992, Numerical methods for partial differential equations: Academic Press, third edn.

Castagna, J. P., Swan, H. W., and Foster, D. J., 1998, Framework for AVO gradient and intercept interpretation: Geophysics, **63**, 948–956.

Cerjan, C., Kosloff, D. D., Kosloff, R., and Reshef, M., 1985, A nonreflecting boundary condition for discrete acoustic and elastic wave-equations: Geophysics, **50**, 705–708.

Clayton, R., and Engquist, B., 1977, Absorbing boundary conditions for acoustic and elastic wave equations: Bulletin, Seismological Society of America, **67**, 1529–1540.

Cole, J. B., 1994, A nearly exact second-order finite-difference time-domain wave propagation algorithm on a coarse grid: Computers in Physics, **8**, No. 6, 730–734.

Cole, J. B., 1998, Generalized nonstandard finite differences and physical applications: Computers in Physics, **12**, No. 01, 82–86.

Dablain, M. A., 1986, The application of high-order differencing to the scalar wave equation: Geophysics, **51**, No. 01, 54–66.

Fornberg, B., 1975, On a fourier method for the integration of hyperbolic equations: Soc. Ind. Appl. Math. J Numerical Analysis, **12**, 509–528.

Gazdag, J., 1981, Modeling of the acoustic wave equation with transform methods: Geophysics, **46**, No. 06, 854–859.

Grant, F. S., and West, G. F., 1965, Interpretation Theory in Applied Geophysics: McGraw-Hill Book Company, first edn.

Hamarbitan, N. S., and Margrave, G. F., 2001, Spectral analysis of a ghost: Geophysics, **66**, No. 04, 1267–1273.

Holberg, O., 1987, Computational aspects of the choice of operator and sampling interval for numerical differentiation in large-scale simulation of wave phenomina: Geophysical Prospecting, **35**, No. 06, 629–655.

Kelly, K. R., and Marfurt, K. J., 1999, Numerical modeling of seismic wave propagation: Society of Exploration Geophysicists, Tulsa, Oklahoma, second edn.

Kelly, K. R., Ward, R. W., Treitel, S., and Alford, R. M., 1976, Synthetic seismograms: a finite-difference approach: Geophysics, **41**, 2–27.

Kosloff, D. D., and Baysal, E., 1982, Forward modeling by a Fourier method: Geophysics, **47**, 1402–1412.

Kreiss, H. O., and Oliger, J., 1972, Comparison of accurate methods for the integration of hyperbolic equations: Tellus, **24**, 199–215.

Levander, A. R., 1985, Finite difference calculations of dispersive rayleigh wave propagation: Tectonophysics, **113**, No. 1/2, 1–30.

Levander, A. R., 1988, Fourth-order finite-difference P-SV seismograms: Geophysics, **53**, No. 11, 1425–1436.

Levander, A. R., 1990, Seismic scattering near the earth's surface: Pure and Applied Geophysics, **132**, No. 1/2, 21–47.

Lindman, E. L., 1975, "Free-Space" boundary conditions for the time dependent wave equation: Journal of Computational Physics, **18**, No. 1, 66–78.

Lines, L. R., Slawinski, R., and Bording, R. P., 1999, Short Note - A recipe for stability of finite-difference wave-equation computations: Geophysics, **64**, No. 3, 967–969.

Long, L. T., and Liow, J. S., 1990, A transparent boundary for finite-difference wave simulation: Geophysics, **55**, No. 2, 201–208.

Madariaga, R., 1976, Dynamics of an expanding circular fault: Bulletin of the Seismological Society of America, **66**, No. 03, 639–666.

Mickens, R. E., 2000, Application of nonstandard finite difference schemes: World Scientific Publishing Co., Singapore, first edn.

Orszag, S. A., 1972, Comparison of pseudospectral and spectral approximation: Stud. Appl. Math., **51**, 253–259.

Press, W. H., Teukolsky, S. A., Vetterling, W. T., and Flannery, B. P., 1992, Numerical recipies in C: Cambridge University Press, first edn.

Randall, C. J., 1988, Absorbing boundary condition for the elastic wave equation: Geophysics, **53**, 611–624.

Rayleigh, L., 1885, On waves propagated along the plane surface of an elastic solid: London mathematical society proceedings, **17**, 4–11.

Reynolds, A. C., 1978, Boundary conditions for the numerical solution of wave propagation problems: Geophysics, **43**, 1099–1110.

Robertsson, J. O. A., and Holliger, K., 1997, Modeling of seismic wave propagation near the earth's surface: Physics of the Earth and Planetary Interiors, **104**, 193–211.

Rutherford, S. R., and Williams, R. H., 1989, Amplitude-versus-offset variations in gas sands: Geophysics, **54**, 680–688.

Strikwerda, J. C., 2004, Finite difference schemes and partial differential equations: Society for Industrial and Applied Mathematics, Philadelphia, second edn.

Virieux, J., 1984, SH-wave propagation in heterogeneous media: velocity-stress finite-difference method: Geophysics, **49**, No. 11, 1933–1942.

Virieux, J., 1986, P-SV wave propagation in heterogeneous media: velocity-stress finite-difference method: Geophysics, **51**, No. 04, 889–901.

Appendix A

Classic finite-difference modelling

A.1 Introduction

The laws of nature are usually best described by differential equations which, for the macroscopic world, apply to usually continuous materials, and usually have continuous solutions. Analytic results (from calculus) give elegant solutions for these cases, but for a quite limited set of problems. That leaves many problems which must have their solutions estimated by using arithmetic operations on arrays of numbers. The point of the finite-difference literature is to minimize the difficulties that occur when continuous functions (where the function points are so close together the differences are infinitesimal) are represented by arrays of samples spaced at finite intervals. Most of the effort within finite-difference studies is focused on 'schemes' which solve problems posed in the form of the differential equations of science. These schemes are then evaluated for efficiency and accuracy by theoretical means, and then with test runs. This study concentrates on these 'schemes', and how they are derived.

A.2 First derivatives

The essential difficulty of finite-difference procedures becomes obvious when a finite-difference option must be chosen to represent a first derivative. A first derivative, or slope, can only be defined as a difference in values between two points. Within

calculus the slope at a point is obtained by using the definition of limits to shrink the difference between the sample points, and the differences of the values at those points, down to infinitesimal amounts. This may be written as

$$\frac{df}{dx} = \lim_{\Delta x \downarrow 0} \frac{f(x + \Delta x) - f(x)}{\Delta x}. \tag{A.1}$$

This procedure is not allowed with finite differences, because only the samples as given are available. The most similar finite-difference equation may be given as

$$D_x f = \frac{f(x + \Delta x) - f(x)}{\Delta x}, \tag{A.2}$$

where the difference is made as small as possible, or one fixed sample length away.

This same equation may also be given as

$$D_x f_n = \frac{f_{n+1} - f_n}{\Delta x}, \tag{A.3}$$

where the input and output values are given in terms of sample numbers instead of their locations along the x axis.

Just one of the finite-difference first derivative options available is the forward difference (to the point ahead) in equation A.3. Also valid is a backward difference (to the point behind),

$$D_x f_n = \frac{f_n - f_{n-1}}{\Delta x}, \tag{A.4}$$

or a central difference (from the point ahead to the point behind),

$$D_x f_n = \frac{f_{n+1} - f_{n-1}}{2\Delta x}. \tag{A.5}$$

The central difference clearly has less bias, but depends on values that are further (in total) from the point where it will be used.

The result of using the forward and backward finite-differences are shown graphically in Figure A.1. The analytic curve which has been sampled is shown in black, and the derivative of this curve at the same point is shown in blue. It is obvious that

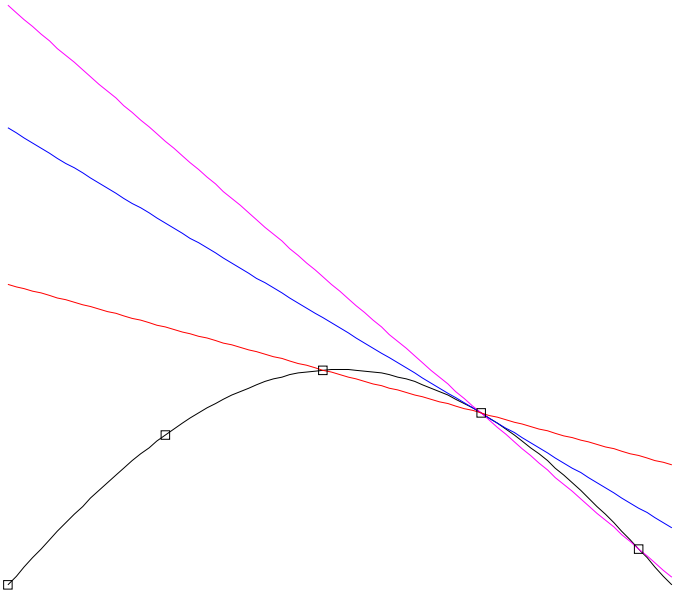

Figure A.1: The backward finite-difference slope is shown in red, and the forward finite-difference in magenta. These may be compared with the true analytic derivative plotted in blue.

the finite-differences shown are biased toward the slopes in the direction from which they were calculated.

The central-difference calculation of equation A.5 is much closer to the analytic result, as shown in Figure A.2.

A.3 Second derivative

A second derivative does not have a similar range of options, because the difference of differences falls naturally at the positions of the original samples. The second

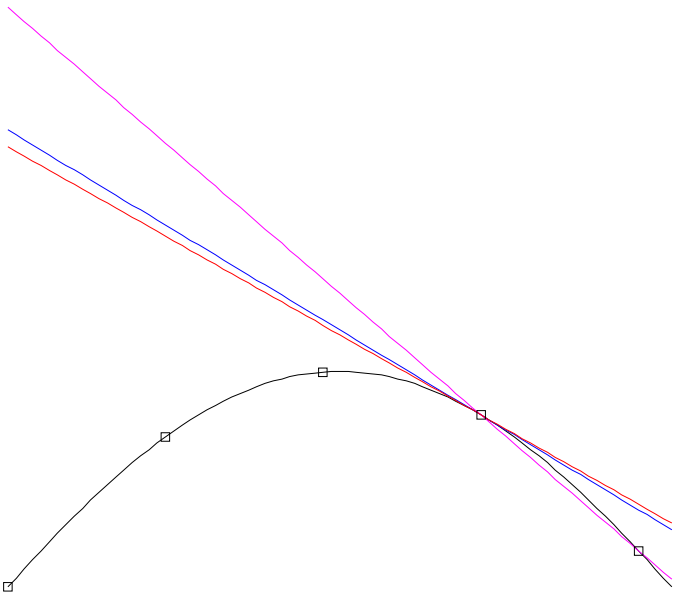

Figure A.2: The central finite-difference slope is shown in red, but is shifted to go through the point at which it applies. For comparison, the forward finite-difference in magenta is also shown. The central finite-difference is obviously much closer to the true analytic derivative plotted in blue.

derivative may be given by

$$D_x^2 f_n = \frac{f_{n+1} - 2f_n + f_{n-1}}{(\Delta x)^2}. \tag{A.6}$$

A.4 Elementary schemes

The most simple finite-difference 'scheme' then has a selected type of estimate for each term of the differential equation, which makes it into a difference equation. The desired output is usually the function throughout space projected to an advanced time (a time-stepped result). In many cases (the explicit cases), the difference equation may be manipulated to solve for an advanced time term. In some cases the advanced time terms may be implicit, which means appear in ways that are impossible to solve for directly. Special techniques may then be required for the solution.

In either case, the functions must be successively stepped through further increments in time to get a full picture through space and time.

The final requirement is to test the scheme. The most important test is for stability. Here amplitudes at a range of frequencies are examined, to make sure that these amplitudes never become infinite. In linear stability analysis this amounts to the exponential growth of at least some frequencies, which soon swamp all other features of the model.

Another test is for consistency, to make sure that a decrease in the step size of all variables leads to reduced errors.

Further tests usually entail comparisons with certain known solutions, usually analytical solutions, to see if the results are close enough to what is expected.

An example of this methodology is given in Aki and Richards (1980) where the

wave equation is represented by the simultaneous equation pair

$$\frac{\partial \dot{u}}{\partial t} = \frac{1}{\rho(x)} \frac{\partial \tau}{\partial x}, \tag{A.7}$$

$$\frac{\partial \tau}{\partial t} = E(x) \frac{\partial \dot{u}}{\partial x}, \tag{A.8}$$

where $E(x) = \lambda(x) + 2\mu(x)$ for P-waves, or $E(x) = \mu(x)$ for S-waves, particle velocity $\dot{u} = \partial u / \partial t$, and stress $\tau = E(x) \partial u / \partial x$. For an initial attempt, this is translated to a scheme with forward finite differences for t-derivatives, and central differences for x-derivatives. Although this appears to be a very natural choice for an explicit scheme, it turns out to be unstable. A scheme with central differences for both t and x is then tried and found to be stable. The details of this scheme are laid out as

$$\frac{\dot{u}_n^{j+1} - \dot{u}_n^{j-1}}{2\Delta t} = \frac{1}{\rho_n} \frac{\tau_{n+1}^j - \tau_{n-1}^j}{2\Delta x}, \tag{A.9}$$

$$\frac{\tau_n^{j+1} - \tau_n^{j-1}}{2\Delta t} = E_n \frac{\dot{u}_{n+1}^j - \dot{u}_{n-1}^j}{2\Delta x}. \tag{A.10}$$

Here the time sample variations are annotated as superscripts instead of subscripts. This explicit scheme may be solved for the advanced time terms $\dot{u}^{j+1}$ or τ^{j+1} as functions of past states and the material parameters.

A.5 Smoothing

Several additional operations may be utilized to supplement the basic finite-difference choices. One which may be incorporated is smoothing in the space domain, a technique introduced by Lax. An example of its use is given in Press et al. (1992), where the one way wave-equation

$$\frac{\partial u}{\partial t} = -v \frac{\partial u}{\partial x} \tag{A.11}$$

is represented by a forward finite-difference in time, and a central finite-difference in space. This equation is

$$\frac{u_n^{j+1} - u_n^j}{\Delta t} = -v\left(\frac{u_{n+1}^j - u_{n-1}^j}{2\Delta x}\right). \tag{A.12}$$

This may be solved for the advanced time term u_n^{j+1}, but as with the Aki and Richards example, it is shown to be unstable. A smoother applied to the u_n^j term on the time side (a gapped running average) gives a result called the Lax-Friedrichs scheme

$$\frac{u_n^{j+1} - 1/2(u_{n+1}^j + u_{n-1}^j)}{\Delta t} = -v\left(\frac{u_{n+1}^j - u_{n-1}^j}{2\Delta x}\right), \tag{A.13}$$

and with appropriate sample rates is shown to be stable (Strikwerda, 2004).

A.6 High accuracy derivatives

A second technique used is to improve the accuracy of the differentiation, usually of the spatial co-ordinates. This is done by using a range of samples that extend further than normal from the estimation point. For example, an estimated second derivative may make use of 5 samples rather than the minimal number of 3. Strikwerda (2004) shows how the 'difference calculus' may be used to derive an appropriate weighting for these samples.

Dablain (1986) also shows how spatial derivatives may be calculated to a higher order by incorporating samples further from the estimation position. He uses a more direct technique, and so the principle may be a little easier to see.

Dablain starts with the formulation of the Taylor series given as

$$f(x + \Delta x) = f(x) + f'(x)\Delta x + f''(x)\frac{(\Delta x)^2}{2!} + f'''(x)\frac{(\Delta x)^3}{3!} + \dots \quad . \tag{A.14}$$

If this is added to a similar expansion for $-\Delta x$

$$f(x-\Delta x) = f(x) - f'(x)\Delta x + f''(x)\frac{(\Delta x)^2}{2!} - f'''(x)\frac{(\Delta x)^3}{3!} + \dots \tag{A.15}$$

the result is

$$f(x+\Delta x) + f(x-\Delta x) = 2f(x) + 2f''(x)\frac{(\Delta x)^2}{2!} + 2f''''(x)\frac{(\Delta x)^4}{4!} + \dots \quad . \tag{A.16}$$

This may be rearranged so that

$$f''(x) = \frac{f(x+\Delta x) - 2f(x) + f(x-\Delta x)}{(\Delta x)^2} - 2f''''(x)\frac{(\Delta x)^2}{4!} + \dots \quad . \tag{A.17}$$

Comparing this with equation A.6 shows that the usual expression for the second derivative is really the first term of an infinite series, and is accurate to second order (fourth order derivatives are required for higher accuracy).

The next stage of accuracy requires that larger Δx's of the Taylor series be utilized, and so doubling the difference used in equation A.16 gives

$$f(x+2\Delta x) + f(x-2\Delta x) = 2f(x) + 2f''(x)\frac{(2\Delta x)^2}{2!} + 2f''''(x)\frac{(2\Delta x)^4}{4!} + \dots . \tag{A.18}$$

Equation A.18 may then be divided by 16 and subtracted from equation A.16 to eliminate the f'''' term. This equation is then solved for the f'' term, as for equation A.17, but the result will be accurate to fourth order. In terms of sample numbers, the equation becomes

$$D_x^2 f_n = \frac{-f_{n+2} + 16f_{n+1} - 30f_n + 16f_{n-1} - f_{n-2}}{12(\Delta x)^2}. \tag{A.19}$$

A.7 High accuracy time-stepping

The final finite-difference extension shown here demonstrates how the time stepping side of the equation may be enhanced. This can be done if the problem equation

itself can be differentiated to give time derivatives of the unknown function in terms of spatial derivatives. An example of this is given in Strikwerda (2004), where the one way equation with a source function term,

$$\frac{\partial u}{\partial t} = -a\frac{\partial u}{\partial x} + f, \tag{A.20}$$

is differentiated in time to get coefficients for a Taylor series expanded in time. The steps to derive the second derivative with respect to t term are as follows:

$$\frac{\partial^2 u}{\partial t^2} = -a\frac{\partial^2 u}{\partial t \partial x} + \frac{\partial f}{\partial t}, \tag{A.21}$$

$$\frac{\partial^2 u}{\partial t^2} = -a\frac{\partial}{\partial x}\Big(\frac{\partial u}{\partial t}\Big) + \frac{\partial f}{\partial t}, \tag{A.22}$$

$$\frac{\partial^2 u}{\partial t^2} = a^2\frac{\partial^2 u}{\partial x^2} - a\frac{\partial f}{\partial x} + \frac{\partial f}{\partial t}. \tag{A.23}$$

The Taylor series in time may be written as

$$u(t+\Delta t, x) = u(t,x) + \Delta t\frac{\partial u(t,x)}{\partial t} + \frac{(\Delta t)^2}{2!}\frac{\partial^2 u(t,x)}{\partial t^2} + \dots \quad . \tag{A.24}$$

Then equation A.23, and the original equation A.20 are used to get

$$u(t+\Delta t, x) = u + \Delta t\Big[-a\frac{\partial u}{\partial x} + f\Big] + \frac{(\Delta t)^2}{2!}\Big[a^2\frac{\partial^2 u}{\partial x^2} - a\frac{\partial f}{\partial x} + \frac{\partial f}{\partial t}\Big] + \dots \quad , \tag{A.25}$$

or

$$u(t+\Delta t, x) = u - a\Delta t\frac{\partial u}{\partial x} + \Delta t f + a^2\frac{(\Delta t)^2}{2!}\frac{\partial^2 u}{\partial x^2} - a\frac{(\Delta t)^2}{2!}\frac{\partial f}{\partial x} + \frac{(\Delta t)^2}{2!}\frac{\partial f}{\partial t} + \dots \quad . \tag{A.26}$$

The third and sixth terms above may be combined, and with $\lambda = \Delta t/\Delta x$, the finite-difference equation is

$$u_n^{j+1} = u_n^j - \frac{a\lambda}{2}(u_{n+1}^j - u_{n-1}^j) + \frac{(a\lambda)^2}{2}(u_{n+1}^j - 2u_n^j + u_{n-1}^j) - \frac{a\Delta t\lambda}{4}(f_{n+1}^j - f_{n-1}^j) + \frac{\Delta t}{2}(f_n^{j+1} + f_n^j). \tag{A.27}$$

This result is the Lax-Wendorf scheme, which is often much better than the equivalent Lax-Friedrichs scheme. Dablain (1986) uses the same technique to obtain a two-dimensional fourth order accurate time step from fourth order spatial derivatives in x and z.

Appendix B

Non-standard finite-difference modelling

The basic theory of non-standard finite-difference (NSFD) modelling was set up by Mickens, with some of his papers from the early nineties. An important reference is the book (Mickens, 2000) which he edited, and where he provided the first chapter.

B.1 Exact finite-difference schemes

Mickens shows that an ordinary differential equation with an analytical solution may be matched exactly by a difference equation with a sampled solution. This equation is what he calls an exact finite-difference solution. This polynomial, with difference and other terms, comes from the determinant of a matrix which includes a minimal set of samples from all the independent analytic solutions of the differential equation.

Use of the analytic solution as a guide for the finite-difference solution is nothing new. Standard finite-difference (SFD) texts always plot their solutions against analytical solutions as a final quality check. Mickens' 'exact schemes', however, use the analytic solutions directly. As it turns out, these schemes have close parallels, but significant deviations from the SFD equations.

An incomplete set of Mickens' SFD and exact solutions is shown in Table B.1. All within this set make use of forward differences for first derivatives.

For all these examples, the two solutions have the same number of terms in roughly the same forms. The deviations tend to be of three types:

Eq	Differential equation	Finite-difference equation	Exact FD equation
1	$\frac{du}{dt} = -\lambda u$	$\frac{u_{k+1}-u_k}{h} = -\lambda u_k$	$\frac{u_{k+1}-u_k}{\left(\frac{1-e^{-\lambda h}}{\lambda}\right)} = -\lambda u_k$
2	$\frac{du}{dt} = -u^2$	$\frac{u_{k+1}-u_k}{h} = -u_k^2$	$\frac{u_{k+1}-u_k}{h} = -u_{k+1}u_k$
3	$\frac{du}{dt} = -u^3$	$\frac{u_{k+1}-u_k}{h} = -u_k^3$	$\frac{u_{k+1}-u_k}{h} = -\left(\frac{2u_{k+1}}{u_{k+1}+u_k}\right)u_{k+1}u_k^2$
4	$\frac{du}{dt} = \lambda_1 u - \lambda_2 u^2$	$\frac{u_{k+1}-u_k}{h} = \lambda_1 u_k - \lambda_2 u_k^2$	$\frac{u_{k+1}-u_k}{\left(\frac{e^{\lambda_1 h}-1}{\lambda}\right)} = \lambda_1 u_k - \lambda_2 u_{k+1}u_k$
5	$\frac{d^2u}{dt^2} = \lambda\frac{du}{dt}$	$\frac{u_{k+1}-2u_k+u_{k-1}}{h^2} = \lambda\frac{u_k-u_{k-1}}{h}$	$\frac{u_{k+1}-2u_k+u_{k-1}}{\left(\frac{e^{\lambda h}-1}{\lambda}\right)h} = \lambda\frac{u_k-u_{k-1}}{h}$
6	$\frac{d^2u}{dt^2} + \omega^2 u = 0$	$\frac{u_{k+1}-2u_k+u_{k-1}}{h^2} + \omega^2 u_k = 0$	$\frac{u_{k+1}-2u_k+u_{k-1}}{\left(\frac{4}{\omega^2}\right)\sin^2\left(\frac{\omega h}{2}\right)} + \omega^2 u_k = 0$
7	$\frac{du}{dt} = w$	$\frac{u_{k+1}-u_k}{h} = w_k$	$\frac{u_{k+1}-\cos(\omega h)u_k}{\left(\frac{\sin(\omega h)}{\omega}\right)} = w_k$
	$\frac{dw}{dt} = -\omega^2 u$	$\frac{w_{k+1}-w_k}{h} = -\omega^2 u_k$	$\frac{w_{k+1}-\cos(\omega h)w_k}{\left(\frac{\sin(\omega h)}{\omega}\right)} = -\omega^2 u_k$

Table B.1: Exact finite-difference schemes for ODEs, compared with standard finite-difference schemes. For the two equations of case 7, note the difference between the variable w and the frequency ω.

- The denominators of the derivative terms are usually not h ($h = \Delta t$), but instead some function of h, depending on the original equation. This is the case for all of these examples except for the second and third. The function is close to h (to the order of h^2). In other words, the smaller h is set, the less the modified function is required.

- Sometimes one of the terms in the numerator of a derivative is multiplied by a function. This is shown in the seventh example. The modification is close to 1 (to the order of h^2).

- Nonlinear terms are represented by non-local expressions, or non-local difference expressions. This may be seen in examples 2, 3, and 4, where x^2 and x^3 do not appear as x_k^2 and x_k^3 , but as more complex expressions.

B.2 Non-standard finite-difference schemes

The rationale of the NSFD method, then, is to improve general finite-difference schemes by including some of the 'exact' forms. Exact results would not be expected from the new schemes, but higher efficiency and better accuracy would be. As with standard schemes, testing would determine whether the new forms were better. This testing has been encouraging for many cases.

Mickens encapsulates his experiences with NSFD schemes into 6 rules which he has found to be useful. He then goes on to show examples of ordinary and partial differential-equations where NSFD based schemes have given superior results, and gives the rationale for his choice of particular schemes.

He usually modifies the denominators of the derivative terms according to the expected form of the solution. For harmonic type equations, denominators of the type in example 6 are used; and for exponential type equations, denominators of the type in example 1 are used.

Mickens discovered that important benefits can be found with the use of appropriate 'non-local' terms. The obvious symmetry of example 2 shows how the correct choice of the non-derivative expression makes the usual adjustment of the derivative expression unnecessary. However, example 3 shows that the expression may become quite complex.

A successful example of a NSFD equation is one set up for a combustion model

$$\frac{du}{dt} = u^2(1-u). \tag{B.1}$$

The SFD equation would be

$$\frac{u_{k+1}-u_k}{h} = u_k^2 - u_k^3, \tag{B.2}$$

whereas Mickens' NSFD equation is

$$\frac{u_{k+1}-u_k}{\left(1-e^{-h}\right)} = 2(u_k)^2 - u_{k+1}u_k - u_{k+1}(u_k)^2. \tag{B.3}$$

To the right of the equal sign, the net of the first two terms makes up a square with amplitude 1, and the last term is a cube with amplitude 1, just as the SFD scheme has. The exact formulation for these terms is designed to give a finite-difference solution with the same zeros as the analytic solution. In particular, when u reaches 1, the slope is exactly zero. Note that this is an explicit scheme, because it is easily solved for u_{k+1}.

A second example of a NSFD scheme is a solution for a linear advection-diffusion equation (normalized). This partial differential equation is

$$\frac{\partial u}{\partial t} + \frac{\partial u}{\partial x} = b\frac{\partial^2 u}{\partial x^2}, \tag{B.4}$$

and the scheme is

$$\frac{u_m^{j+1} - u_m^j}{\Delta t} + \frac{u_m^j - u_{m-1}^j}{\Delta x} = b\Big[\frac{u_{m+1}^j - 2u_m^j + u_{m-1}^j}{b(e^{\Delta x/b} - 1)\Delta x}\Big]. \tag{B.5}$$

This was constructed quite simply, because

$$\frac{\partial u}{\partial t} + \frac{\partial u}{\partial x} = 0 \tag{B.6}$$

has an already exact solution

$$\frac{u_m^{j+1} - u_m^j}{\Delta t} + \frac{u_m^j - u_{m-1}^j}{\Delta x} = 0, \tag{B.7}$$

and

$$\frac{\partial u}{\partial x} = b\frac{\partial^2 u}{\partial x^2}, \tag{B.8}$$

has an exact solution

$$\frac{u_m - u_{m-1}}{\Delta x} = b\Big[\frac{u_{m+1} - 2u_m + u_{m-1}}{b(e^{\Delta x/b} - 1)\Delta x}\Big], \tag{B.9}$$

and the two solutions were just combined.

B.3 Non-standard finite-difference wave equations

The lead in using NSFD schemes for the wave equation has been taken by Cole. Chapter 3 in Mickens' book was written by Cole, and shows how he has used NSFD techniques to model the wave equation in one, two, and three dimensions.

The starting point for wave equation NSFD modelling is the one-dimensional one, where it is shown that for a given wavenumber and frequency, the sample rate Δt may be replaced by $sin(\omega \Delta t/2)$, and the sample rate Δx by $sin(k\Delta x/2)$. This conforms with Mickens' first observation of his exact scheme changes. Cole shows how a truncated single frequency wave train propagated through a narrow high velocity barrier appears much closer to expectations with the NSFD algorithm compared to the SFD algorithm.

Cole continues to two dimensions by combining the normal Laplacian with another oriented at 45 degrees. The combination begins with a variable weighting, but is then optimized. The accuracy of this combination he calculates to be of order 8, as compared to order 2 for the SFD scheme. In a similar fashion he extends the method to the full three dimensions.

At the end of the chapter, Cole shows how the SFD Yee algorithm for Maxwell's equations may be improved by using a NSFD version. The discussion here is for an harmonic (single frequency) case, but apparently works very well for the range of frequencies that are required to make up a signal with a finite length in time. He also claims that NSFD techniques may be used to improve the propagation of broad band signals as well.

Appendix C

Definitions used in finite-difference modelling

C.1 Time-stepping

Finite-difference techniques are the natural way to use the sampled data required for digital computers to simulate the infinitesimal differences used in classical analysis. Differences and differences of differences, then, are used to simulate first and second derivatives within a differential equation. The questions of how finely spaced the sampling must be, and how the differences must be related to the original sampling, determine the accuracy which results from the finite-difference approximations.

The term "time stepping" or "time marching" indicates that the differential equation will be used to show the form the function takes as time progresses. For the finite-difference method, the function will be determined at a succession of time points called steps. The original function defined in "n" space with initial conditions, will then be used to create an "n+1" dimensional function, with time as the extra variable.

In the practical terms of the wave-equation, it will show how waves travel through a medium in time.

C.2 Errors - instability and dispersion

The problems that result from finite-difference modelling are mostly either instability or dispersion. In some terms they may be considered to result from opposite causes, and the best approximations result from a selection of parameters which steer between the two hazards.

Instability is a disastrous type of error which eventually overwhelms the useful results from the model. It is characterized by an exponential growth of amplitudes, usually at the highest frequencies. The error may take some time to become evident if the amplitudes of the problem frequencies begin at very low levels.

Dispersion is a more subtle error characterized by a spreading out of energy packets. It may be quantified as a difference in the propagation velocities of high and low frequency signals, or components of signals. Dispersion occurs naturally in real materials, usually with low frequencies lagging the high frequencies. Unfortunately, "numerical dispersion" or "grid dispersion" causes a lag of high frequencies from low frequencies.

C.3 Order of accuracy

In the finite-difference world, a solution scheme is usually attributed with an 'order of accuracy'. This accuracy can be associated with a particular sampling interval required in the solution. As an example, the finite-difference solution of the wave-equation requires sampling in space and time, and so a particular solution might be characterized as 'fourth order in space' and 'second order in time'.

To determine an order of accuracy of a finite-difference equation, or part of an

equation, it must be expressed in terms of an infinite Taylor series in powers of the sample rate. If the spatial sample rate is Δx, for example, the Taylor series must be expressed with terms of $(\Delta x)^n$. The order of accuracy is then the power of the last term before those terms of the series which must be truncated. Examples are given in section A.6, where equation A.17 shows why the standard finite-difference operator for the second derivative is second order, and gives the fourth order operator for the second derivative in equation A.19, and how it is derived.

It may be seen with this example that higher order accuracy is obtained by considering a greater length of curve.

C.4 Explicit vs. implicit

Finite-difference schemes may be sorted into those with explicit or implicit solutions. An explicit scheme is the most simple to calculate because the advanced or stepped variable appears only once, and its value can be found by an algebraic manipulation of the other terms in the equation . The time-stepped wave equation as it is treated in this thesis is explicit, and the type of equation developed is shown in Figure 2.18. The advanced time step is denoted by the time $t + \Delta t$.

An implicit scheme has the advanced variable appearing in the scheme more that once, and usually can not be solved for with algebra. It appears to require the answer in order to compute the answer.

The advanced variables in an implicit scheme may be found as a solution to a set of n simultaneous equations where, for the case of one spatial dimension, n is the number of samples in the line. Specifications of the boundary conditions must also

be included as part of the simultaneous equations.

Solutions for these simultaneous equations are not as difficult as they first appear, because the relevant matrix is very sparse and has the same terms appearing along the main diagonals. An implicit scheme with the displacement at advanced time appearing in three terms will be 'tri-diagonal', and have repeating coefficients along the main diagonal and the two adjacent diagonals. A simple example of this type of scheme is given in Strikwerda (2004) equation 1.6.1, and the solution technique is given in section 3.5.

Appendix D

Non-staggered grid corrections

Finite-difference displacement modelling in two dimensions was originally done with the two components of the displacement defined at the same points, for example in Kelly et al. (1976). Figure D.1 shows the layout of this system for the z component acceleration (Contrast with Figure 3.2 for the staggered grid). The acceleration contributions from the z displacements (offset in either the x or z directions) are the same as with the staggered grid.

However, with this non-staggered grid, the contributions from the x displacements are a full grid spacing away in both the x and z directions, in contrast to the staggered grid system where they are only one-half a spacing away.

Derivation of the non-staggered grid corrections requires changes to some of the formulae in section 3.3. In particular, the cross-term $D_{xz}U_x$ operation on the exponential mono-chromatic plane wave, using the points shown in Figure D.1 results in equation D.1. Here ε is defined by equation 3.16.

$$D_{xz}U_x = \frac{sin\theta}{(2\Delta x 2\Delta z)} \left(e^{i\varepsilon(z+\Delta z,x+\Delta x,t)} - e^{i\varepsilon(z+\Delta z,x-\Delta x,t)} - e^{i\varepsilon(z-\Delta z,x+\Delta x,t)} + e^{i\varepsilon(z-\Delta z,x-\Delta x,t)}\right). \quad \text{(D.1)}$$

This equation may be compared with equation 3.28.

The same sequence of steps following equation 3.28 may be used to arrive at the

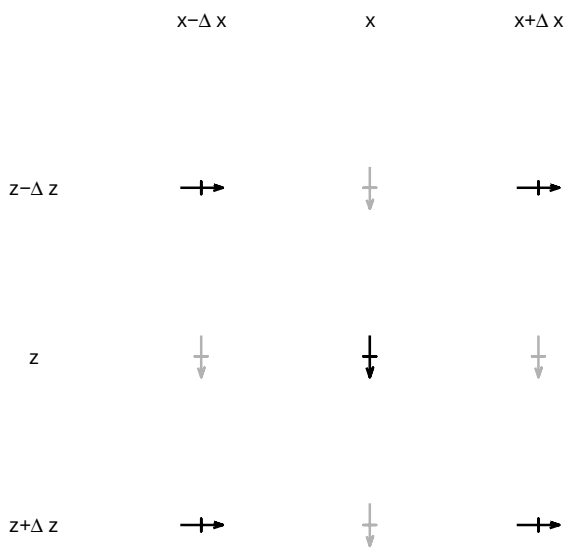

Figure D.1: The non-staggered grid. The arrows show all the relative positions and components of the displacements which will determine the second-order z acceleration at the centre. The four contributing x displacements are dark coloured, and surround the output point a full grid spacing away in both directions.

equivalent of equation 3.33, and in this way equation D.2 may be reached.

$$D_{xz}U_z = sinc\,(k_x\Delta x)\,sinc\,(k_z\Delta z)\,\frac{\partial^2 U_x}{\partial x \partial z}. \tag{D.2}$$

Again, it may be assumed that the relevant wavenumbers are contained within ±Nyquist. Then the relevant values of k are contained within $[-\pi\Delta x^{-1}, \pi\Delta x^{-1}]$, and it follows that the sinc function arguments fall within $[-\pi, \pi]$ radians. Figure 2.2 shows that the sinc functions go right to zero in this range. This means that away from the principle axes directions, higher wavenumbers may be severely attenuated by the non-staggered grid model, and the Nyquist wavenumbers reduced close to zero.

The severe attenuation, and thus dispersion, in the off-axes directions, explains why the staggered grid models became so popular.

Appendix E

Finite-difference modelling formulae

There are a number of formulae that should be considered at the beginning of a finite-difference modelling project. They apply to finite-difference modelling in general, although the choice of an algorithm may require fine tuning of some parameters.

The first determining factor is usually the frequency range of the seismic wavelet that will be propagated. The maximum frequency required here must be translated into the maximum wavenumber required, because numerical dispersion increases strongly with increasing wavenumber. The translation formula is

$$W_{max} = \frac{f_{max}}{V_{min}}, \tag{E.1}$$

where W is a wavenumber, f is a frequency, and V is a velocity.

An example of a wavelet spectrum is given in Figure E.1. The wavelet is a 30 Hz. Ricker, and the peak energy appears at 30 Hz in the Figure. The highest frequency in the wavelet is where the smooth wavelet disappears into the numerical noise at about 100 Hz.

The wavenumber spectrum translates directly from the frequency spectrum with the same formula as equation E.1. The translation depends on the velocity of the material in which the wavelet propagates, and the highest wavenumber in the spatial frequency depends on the lowest velocity in the model.

As an example, if only a pressure wave propagating at 2000 m/sec. is being modelled, the wavenumber spectrum in space is shown in Figure E.2. If a shear

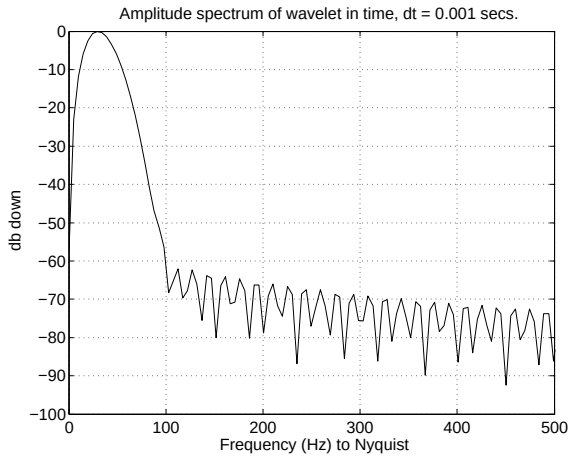

Figure E.1: Frequency spectrum of a zero-phase Ricker wavelet in time. The highest wavelet frequency is at about 100 Hz.

wave propagating at 1000 m/sec. is also being modelled, its wavenumber spectrum in space is shown in Figure E.3. It may be seen that the spatial sampling is sufficient for the pressure wave (at .05 cycles/m.), but not for the shear wave.

The second step is to determine the maximum fraction of the Nyquist wavenumber that may be modelled with acceptable dispersion. It may be necessary to translate the figure *grid points per wavelength* to a fraction of Nyquist wavenumber. The formula is

$$fraction = 2/n, \tag{E.2}$$

where $fraction$ is the maximum allowable fraction of the Nyquist wavenumber, and n is the number of *grid points required per wavelength*. The number *grid points required per wavelength* has been suggested as 10 in Virieux (1984) for uncorrected modelling, and 5 for Levander modelling (Levander, 1988). These translate into $fraction$s of 0.2 and 0.4. With correction filters of size 5 by 5, a $fraction$ of 0.5 is usually quite practical, and sometimes 0.75 works well.

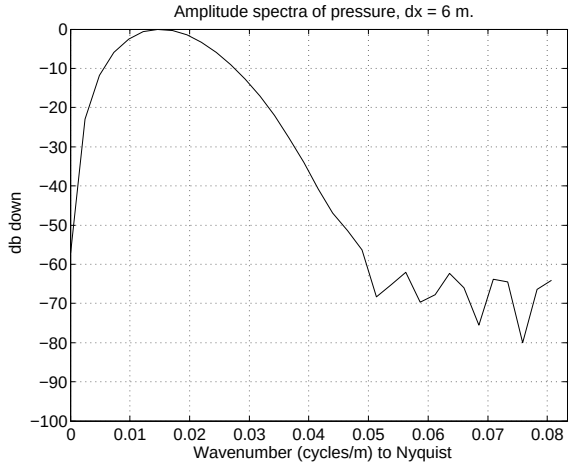

Figure E.2: Wavenumber spectrum of a pressure wavelet (2000 m/sec.) in space. The highest wavenumber is at about .05 cycles/m.

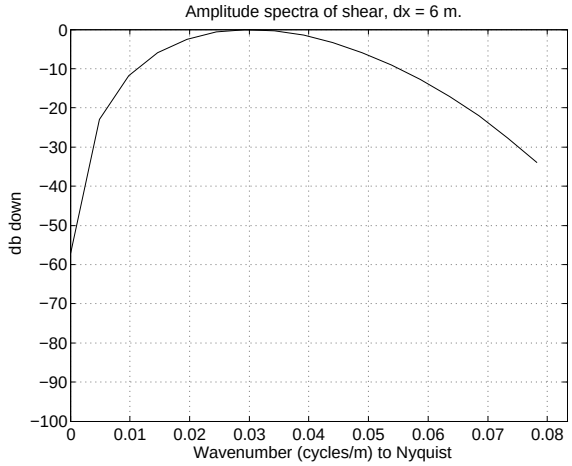

Figure E.3: Wavenumber spectrum of an shear wavelet (1000 m/sec.) in space. The highest wavenumber is above Nyquist when the sample rate is 6 m.

Choice of these minimum parameters may depend on the details of the model. A thin layer of the lowest velocity material may cause minimal dispersion because of the few steps required to cross it.

The spatial sample rate may then be determined from

$$\Delta x = \frac{2 * fraction}{W_{max}}, \tag{E.3}$$

where Δx is the spatial sample rate.

The final step is to choose a time sample rate to provide stability. For general second-order finite-difference models, and for the correction filter modified models, the time sample rate may be chosen to meet the criterion specified in equation 3.73. For Levander style models the time sample rate must be made slightly smaller again, and the formula is

$$\Delta t < \frac{\Delta x}{v}\sqrt{\frac{3}{8}}, \tag{E.4}$$

as described in Lines et al. (1999). This means that Levander models must use a sample rate that is approximately 15% smaller than other models, and the slightly lower efficiency and higher dispersion act against some of the Levander advantages.

Appendix F

Colour display of wavefields

Most of the wavefields in this thesis have been displayed in colour, with the colour code shown in the bottom right corner. There are two types of coding. The first code shows displacement direction, with the highest amplitude displacement having the most intense colour. The second code shows the amount of stored potential energy, with one colour pair showing compressional energy, and another colour pair showing shear energy.

The displacement coding used in shown in Figure F.1. The red, green, blue proportions were chosen mainly for ease of implementation, and all three colours are present at most angles. An example of this type of display is Figure 4.31.

A more discriminating system might have colours combined in pairs rather than triplets. This has not yet been attempted.

The potential energy colour coding system distinguishes pressure and shear energy by calculating the divergence and curl of the displacement field. If U is a plane pressure wave with wave form F propagating at an angle θ (as in Figure 3.1) its displacements are given by

$$U_z = cos\theta F((zcos\theta + xsin\theta)k - \omega t), \tag{F.1}$$

$$U_x = sin\theta F((zcos\theta + xsin\theta)k - \omega t). \tag{F.2}$$

By contrast, if U is a plane shear wave with wave form G propagating at an angle

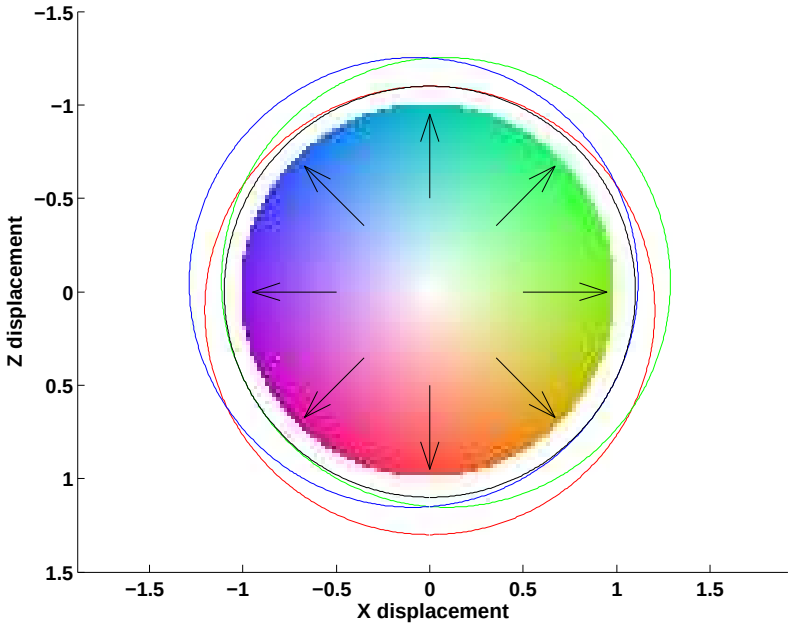

Figure F.1: The coding details of displays coded by displacement. The inner ring shows how colour relates to displacement direction. The outer three coloured curves in polar coordinates show the level of red, green and blue combined for each direction. The black circular ring shows level zero.

θ (as in Figure 3.3) its displacements are given by

$$U_z = sin\theta G((zcos\theta + xsin\theta)k - \omega t), \tag{F.3}$$

$$U_x = -cos\theta G((zcos\theta + xsin\theta)k - \omega t). \tag{F.4}$$

Then the divergence and curl of the pressure wave are

$$\nabla \cdot U = \frac{\partial U_x}{\partial x} + \frac{\partial U_z}{\partial z} = F', \tag{F.5}$$

$$\nabla \times U = \frac{\partial U_x}{\partial z} - \frac{\partial U_z}{\partial x} = 0. \tag{F.6}$$

The curl in this two dimensional case is taken to be a scalar, consisting of the y component of the curl. The x and z components are zero because the y displacement is zero, and the displacement variations with y are zero.

By contrast, the divergence and curl of the shear wave are

$$\nabla \cdot U = \frac{\partial U_x}{\partial x} + \frac{\partial U_z}{\partial z} = 0, \tag{F.7}$$

$$\nabla \times U = \frac{\partial U_x}{\partial z} - \frac{\partial U_z}{\partial x} = G'. \tag{F.8}$$

Again, the curl has only one component, and may be considered a scalar.

These results indicate that a plot of the divergence of the displacement field will show a gradient only where the displacements are caused by pressures. Similarly, a plot of the curl will show gradients only where the displacements are caused by shears. The two plots may be combined into one colour coded display if the two scalar values are treated as displacements. They may then be plotted with the displacement colour code described above.

The key for the pressure/twist plot is shown in Figure F.2. The colours are the same as the Displacement plot in Figure F.1, except for a 45 degree rotation. With

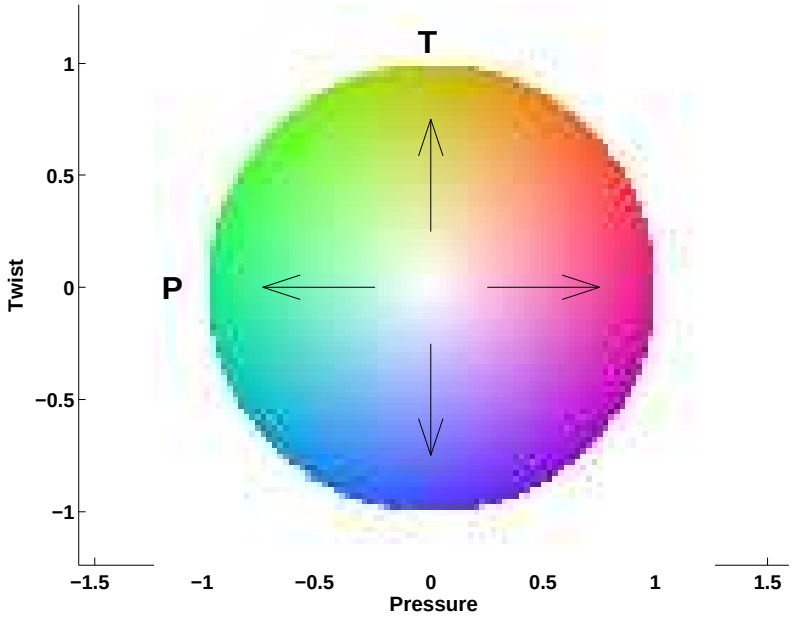

Figure F.2: The coding details of the interpreted pressure/twist plot.

this orientation pressure variations display as red and green, and shear variations display as blue and yellow. Areas with combinations of pressure and shear energy will display intermediate colours. An example of this type of display is Figure 4.33, corresponding to Figure 4.31.

Appendix G

Initializing wavefields

There are two two ways in which sonic energy was introduced into the model environment. The first way, called the *time source*, was by adding to the existing model displacements within a very small area, but over an extended time period. The second way, called the *space source*, was by specification of all the displacements within the model at two times: time 0 and time $0 + \Delta t$.

The advantages of the time source is that it can simulate quite accurately an explosive energy source, and it may be used near any boundary. The disadvantages are that it takes additional time for the energy to be introduced, it applies a derivative to the wavelet form, and sometimes high frequency artifacts may be created. It is very useful for simulating an explosive source near the surface. Figure G.1 shows how a simulated dynamite source may be introduced into a staggered grid model. The displacements used were not impulsive, but took the smoothly varying positive and negative values of a band limited pulse.

An example of a wavelet used for a time source is the zero-phase Ricker wavelet displayed as the top curve in Figure G.2. The centre curve is a perfect derivative of this wavelet, and the bottom curve is an actual propagating wavelet as recorded within the model. It may be seen that the resulting wavelet is very close to the derivative of the input wavelet. This may be expected because in Figure G.1, the two opposing sources are both allowed to propagate in both directions, and this is very close to differentiating the wavelet.

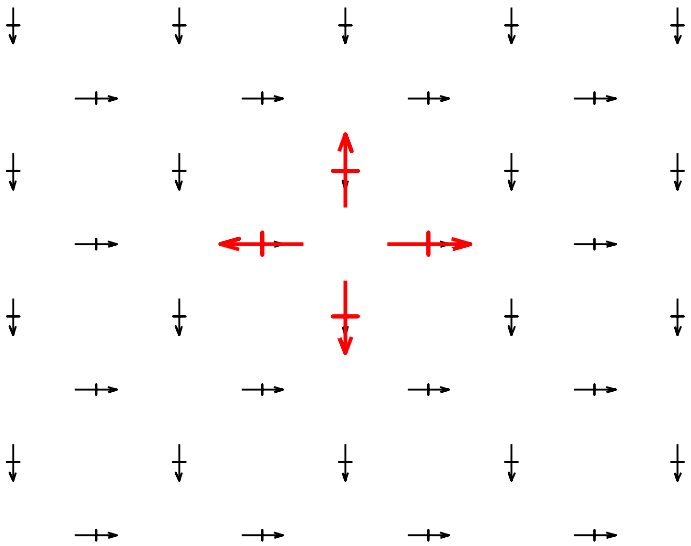

Figure G.1: The simulated dynamite source, with displacements directed uniformly about a centre.

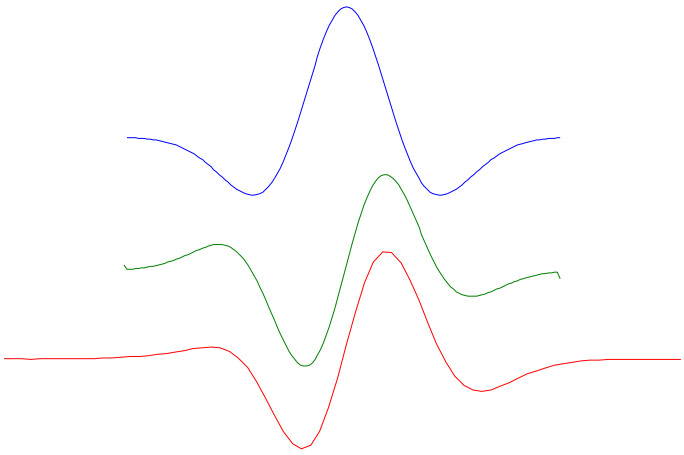

Figure G.2: The top curve is a typical time source wavelet. The centre curve is the derivative of this wavelet, and the bottom curve is an actual resulting wavelet as recorded in the model.

The advantages of the space source introduction are the close control of the wavelet form, and the time saved. The disadvantages are the elaborate preparations required to construct the time pair, and the requirement for a sizable constant velocity zone within the model where the wavelet can be introduced. It is very useful for testing, and for generating Rayleigh waves.

A space source time zero wavelet ring may be constructed by specifying, at each displacement location within the wavelet range, the displacements appropriate for the component, the distance from the centre, and the distance from the wavelet end. The values must also be scaled to represent the dropoff associated with a cylindrical wave. The $0 + \Delta t$ ring may be constructed using the same principles, but advanced in an outward direction by the distance $v\Delta t$.

An example of a space source is shown in Figure 3.11, which shows a combination of a pressure ring and a shear ring in a colour displacement plot. Figure 3.10 shows the same combination of rings but with a vector plot. The final wavefront displacements which were initiated in this way are shown in Figure 3.12, among others.

Appendix H

Common boundary conditions for edges

Specification of boundary conditions for finite difference modelling consists of choosing displacement values for points beyond the limits of the region being modelled. One additional point in each of the displacement directions is required for the most basic modelling, because the finite difference operators involve at least one displacement in each offset direction from the output point of the calculation. So output points on the boundary then require input points from beyond the boundary. These external points cannot themselves be calculated by the same means as the internal points, and so special methods must be used.

The easiest specification for external points is to make their displacements zero. Zero displacement mean the external medium is perfectly rigid, and it reflects all impinging energy directly back into the model. This may be a good choice for some applications.

Another form of boundary condition, called here a transmitting boundary, is mentioned in chapter 5. These boundaries are required where the model must be continuous with an unbounded region of featureless space.

This appendix is concerned with two types of boundaries which are sometimes useful: the symmetric boundary and the free surface boundary. The symmetric boundary does not represent a physical boundary, but may sometimes be used to cut the modelling effort in half. The free surface boundary represents the real surface of the earth, and it must be properly represented for many seismic applications.

The symmetric boundary is useful where the medium to be modelled is symmetric, and the energy source is also symmetric. A model of plane layers is an example of symmetry in the medium, and a compression (explosive) source is an example of symmetry in the source. A symmetric boundary requires that the correct displacements be assigned to the external columns shown on the left of Figure H.1.

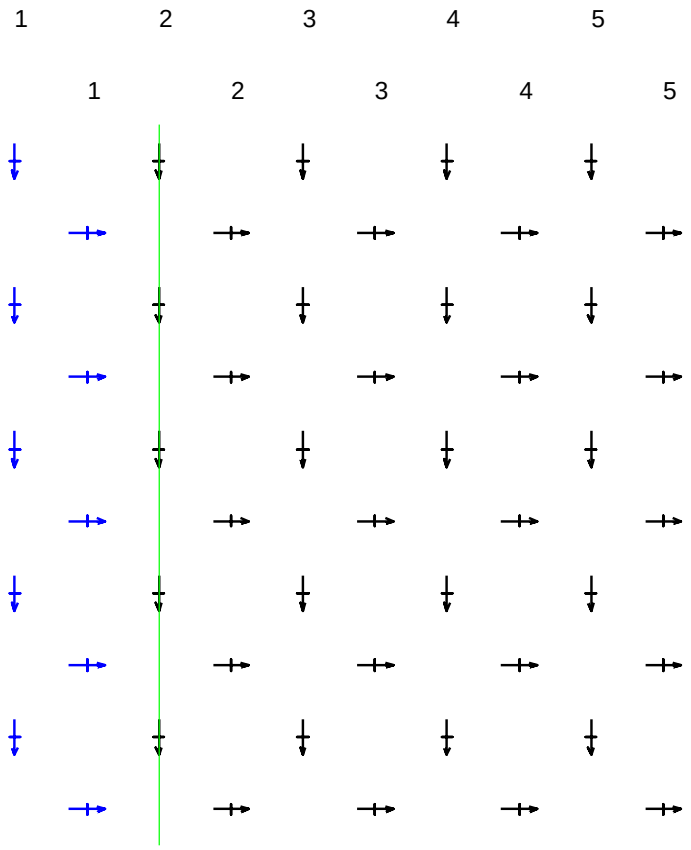

Figure H.1: The staggered grid set up with a symmetric boundary on the left side. The symmetric source is normally positioned at the green line.

The black arrows represent the internal portion of the model, and the blue arrows on the left represent the external displacements which must be determined. Before

each time step, the horizontal displacement in column 2 must be duplicated with the opposite sign in column 1. Also the vertical displacement in column 3 must be duplicated with the same sign in column 1. These steps may be seen to be symmetric about the vertical displacement in column 2, and this is where the pressure source must be centered. If the finite-difference operators require more points, the symmetry may be extended to further points across the boundary.

The free-surface boundary is defined in Figure H.2 as the the line between the internal black arrows, and the external blue arrows at the top. Rather than try to

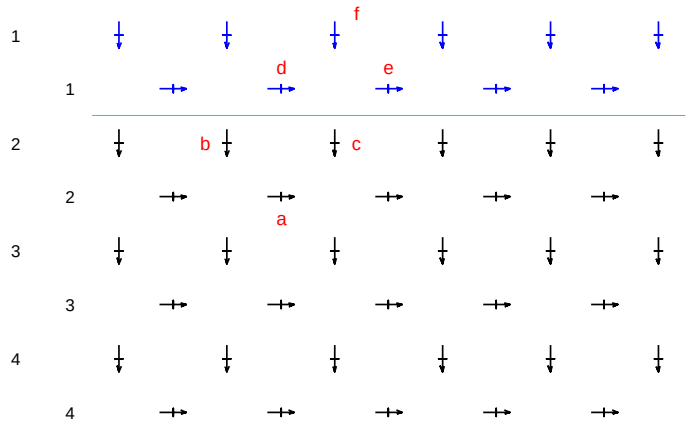

Figure H.2: The blue boundary positions which must have displacements calculated to represent a free surface, positioned at the green line.

represent the external displacements as caused by very low velocities and densities, these displacements are designed to provide the zero stress conditions which give the same results. The stress equations, which must be made equal to zero by the appropriate choice of external displacements, are

$$\sigma_{xz} = \mu\left(\frac{\partial U_z}{\partial x} + \frac{\partial U_x}{\partial z}\right) = 0, \tag{H.1}$$

$$\sigma_{zz} = (\lambda + 2\mu)\frac{\partial U_z}{\partial z} + \lambda\frac{\partial U_x}{\partial x} = 0. \tag{H.2}$$

These equations may be found in Levander (1988), where they are used in the split step modelling method.

The practical use of equation H.1 is illustrated with the *abcd* block in Figure H.2. It requires that d must be made equal to $a + c - b$. This means that the *abcd* block may be twisted, but not distorted.

Similarly, equation H.2 applies to the *cdef* block. It requires that f must be made equal to $c + (e - d)\lambda/(\lambda + 2\mu)$. If the medium was a fluid ($\mu = 0$) it would mean maintenance of a constant area. In an elastic medium the imposed external z displacement at f is somewhat reduced compared to the displacement at c.

Appendix I

Zero-phase filters from a Fourier transform

The most general way to design a zero phase filter is to start with a Fourier transform equation which has its space domain origin in the centre. The cosine (real) terms of the matrix will then be symmetric about the centre, and the sine (imaginary) terms will be anti-symmetric. The real terms of the output spectrum will be the desired amplitude spectrum, and the imaginary terms may be specified as zero, so phases cannot be shifted, and the amplitude spectrum is not affected. Figure I.1 shows a Fourier transform equation, and the symmetry of the transform matrix may be seen. An advantage to this type of design is that it may be used to design a non-symmetric filter to compensate for an internal boundary.

A more efficient way to design a zero phase filter is to assume initially that it will be symmetric. The origin of the Fourier components in the matrix may be assumed to be at the left edge, and the centre of the filter at the top of the vector. The full forward Fourier analysis may then be duplicated by doubling the amplitude of all the filter coefficients except for the centre (top) coefficient. This applies to the transform shown in Figure 2.22. The optimal inverse matrix equation may be set up by doubling all the terms of the Fourier series except for those on the axis (leftmost). The zero phase filter may then be constructed by reversing the order of the output time sequence (from the second to the end), and attaching it to the front of this same output filter. This procedure would apply to the operation shown in Figure 2.24.

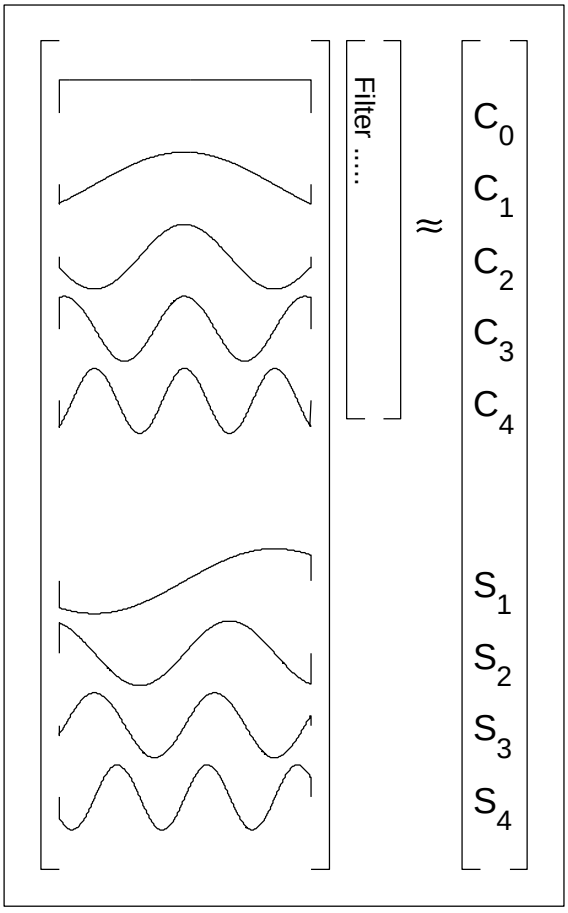

Figure I.1: The general matrix equation for the design of a zero phase filter. The Fourier components are centered, and both cosine and sine terms are included. The sine terms (S's) may be set to zero.

A similar procedure may be set up for the design of optimal two-dimensional filters.

Appendix J

Correction filters for unstable conditions

Most of the analysis done in this thesis assumes that the sampling parameters have been chosen for stability before corrections are made. Correction filters may be designed to compensate for inherently unstable parameters, and this is discussed to a limited extent in this section. This type of correction filter might prove useful in a model with a limited extent of high velocity material, and where high accuracy is required in other areas. The discussion here will be limited to the one-dimensional case.

In the one-dimensional case, $\Delta t < \Delta x/v$ ensures that a model is stable but dispersive. The correction filter reduces this dispersion. In section 2.6 the correction filter design procedure is shown, and example filters are shown in Figures 2.26 and 2.27. Note that for wavenumbers above the design top, the correction is conservative, and insufficient to prevent dispersion. This means that wavenumbers here remain attenuated, and fade out of the model as required for stability.

Two examples show how this design procedure works where the parameters are inherently unstable. The first example is where Δt is exactly twice what it should be ($\Delta t = 2\Delta x/v$). This case has a perfect solution, and is discussed in section 2.4. Figures 2.19 and 2.20 from that section show the corrections required in the wavenumber and spatial domains. The filter as derived by the optimising program is shown in Figure J.1. This derived filter is the same as the ideal, except for terms on the order of 10^{-15}, shown for terms 1 and 5 in the Figure.

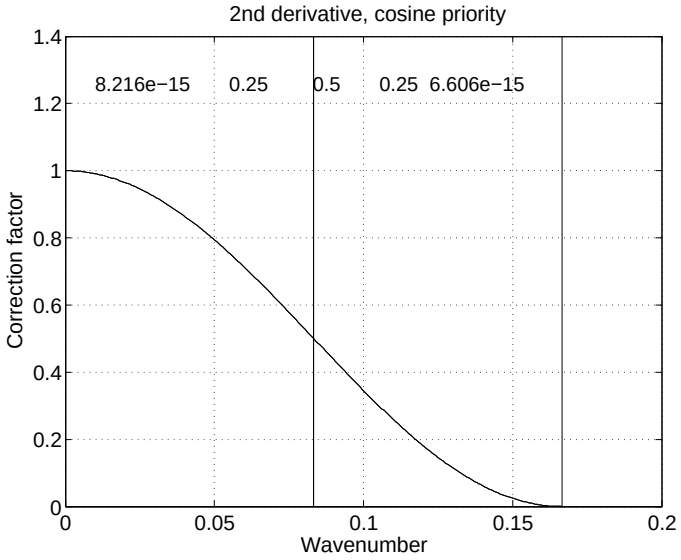

Figure J.1: The optimizing response of the program where the exact response is known, unstable case. The spatial coefficients appear are expected to be $.25, .5, .25$ as the centre values in the Figure show. The first and last terms of the filter are very close to zero. The parameters are: $v = 1500$ m/sec, $\Delta x = 3$m, and $\Delta t = .004$ secs.

The second example is one which has no exact solution. A first attempt to design a correction using the princples from section 2.6 gives the result shown in Figure J.2. Here the stabilizing effort would appear to be less onerous because the time sample rate is smaller than the first example, and therefore closer to stability. Instead, the black design curve does not suppress the high wavenumber energy sufficiently. This is most notable at the Nyquist frequency, where the amplitudes should be suppressed to almost 0.2, but are left at more than 0.4. Note that k_{max}, as specified in equation 2.24, is plotted as the vertical red line, and that all wavenumbers to the right of this line should be reduced to below the black line levels. This shows how the conservative result of the techniques used for stable cases does not work well for the inherently unstable cases.

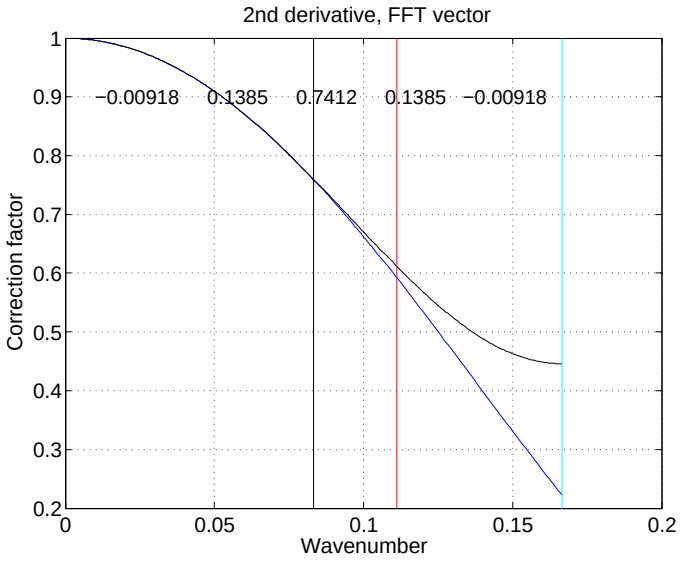

Figure J.2: The black curve shows the optimizing response of the program for a general unstable case. The program here has designed a filter which does not attenuate higher wavenumbers sufficiently. For stability, all wavenumbers to the right of the red (k_{max}) line must have their amplitudes below the levels of the blue curve. The parameters are: $v = 1500$ m/sec, $\Delta x = 3$m, and $\Delta t = .003$ secs.

At this point a non-standard co-ordinate origin is introduced, which sheds some light on several aspects of optimal correction filter design. The origin of spatial co-ordinates used to this point may be considered to be the FFT standard. Here the origin coincides with the position of one of the data points. An equally logical location for an origin is exactly half way between sampled data points. These choices are shown on the diagram in Figure J.3. The most critical features which the choice

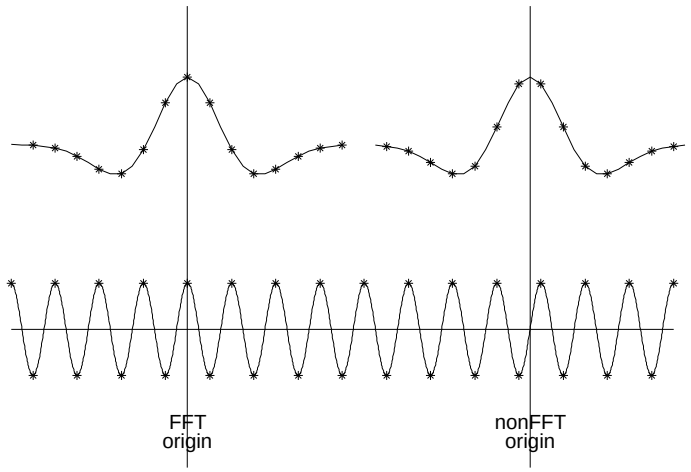

Figure J.3: A display of how the choice of origin with respect to the sample positions affects some critical forms. A standard FFT origin is on the left, and a non FFT origin on the right. It affects the assignment of the Nyquist frequency as a cosine or sine, and the type of symmetry for zero-phase wavelets.

of origin affects are the assignment of the Nyquist frequency as a sine or cosine, and the type of symmetry of a zero-phase wavelet.

The standard FFT origin assigns zero to the center of a sample position. All the cosine (real) terms are one here at the origin, and in particular the Nyquist frequency (with extremes on every sample) fits the cosine definition. The cosine terms of the Fourier transform with the FFT convention number two more than the sine terms. This is because the DC and Nyquist terms both have amplitudes of one

at the origin, consistent with the values of $cos(0)$ and $cos(Nyquist)$ there (see the cosine terms in table J.1). The sine terms of these same frequencies are uniformly zero, and therefore two fewer terms are required (see the sine terms in table J.1).

Cycles/length	DC	1	2	3	4	.....	n/2-3	n/2-2	n/2-1	n/2
Cosines	x	x	x	x	x		x	x	x	x
Sines		x	x	x	x		x	x	x	

Table J.1: The required frequencies for a standard FFT transform of length n.

Cycles/length	DC	1	2	3	4	.....	n/2-3	n/2-2	n/2-1	n/2
Cosines	x	x	x	x	x		x	x	x	
Sines		x	x	x	x		x	x	x	x

Table J.2: The required frequencies for a non-standard (shifted origin) FFT transform. Note the Nyquist frequency ($n/2$) is a sine.

Also, The following observations may be made about the zero-phase (symmetric) filters within this convention.

1. Their output position (at the center) coincides with the input sample positions.

2. They are the ideal correction filters for second derivative operations, where the output points also coincide with the input sample positions.

3. The filters may be used to either reduce high frequencies (by averaging) or enhance high frequencies (with a decon effect).

4. They have an odd number of filter coefficients.

5. They make natural correction filters for inherently stable models.

The non FFT origin assigns zero to a position half way between the sample positions. The Nyquist frequency here is a sine term because its extremes are shifted

one half sample spaces from the origin. There are an equal number of cosine and sine terms in this system, because the significant Nyquist term is a sine instead of a cosine (see table J.2).

The following observations may be made about the zero-phase filters within this convention.

1. Their output position is half way between the input sample positions.

2. They are the ideal correction filters for first derivative operations, where they compensate for the intermediate output position of these operations.

3. The filters are most naturally used to reduce high frequencies (they have a natural averaging effect).

4. They have an even number of filter coefficients.

5. They make natural correction filters for inherently unstable models, with their averaging tendency at the highest frequencies.

There are two arguments to show why the non FFT origin convention is effective for unstable correction filters. The first is the implicit averaging action of the near samples, mentioned above. The second is a more elaborate argument based on whether the Nyquist frequency is a cosine or sine term. With either discrete Fourier transform, all the sine terms must be minimized to ensure symmetry about the zero axis. With the standard FFT convention, the Nyquist and other high frequency cosine terms must be explicitly zeroed, separately from the sine terms. With the non FFT convention, most of the corresponding frequencies near Nyquist are already zeroed along with the zeroing of the other sine terms.

An example of a non FFT design for an unstable case is shown in Figure J.4. The 7 point correction filter designed here has a moderately good fit throughout the

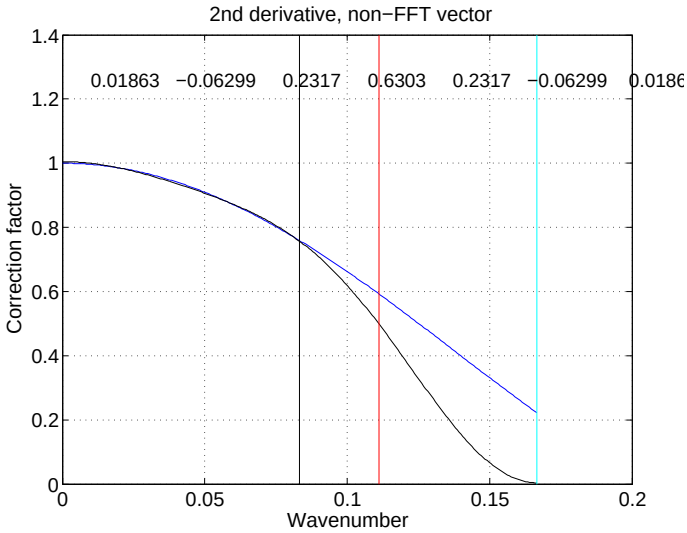

Figure J.4: The black curve shows the 7 point non FFT optimizing response of the program for a general unstable case. Construction is by autocorrelation of a pure non FFT design. It may be seen that this design style results in an effective stabilizing filter for the wavenumbers beyond k_{max}, marked by the red line. This figure may be compared with Figure J.2, where the parameters are the same.

design zone, and adequately suppresses the noise wavenumbers beyond k_{max}. This filter is actually an autocorrelation of a filter designed by non FFT principles. The desired response of the original filter was specified as the square root of the ultimate design. This filter was then truncated and autocorrelated, which resulted in the necessary amplitude response and the odd number of coefficients.

The filter designed here was tested for stabilization of a real wave. The wave was first propagated with no corrections, and the familiar instability artifacts may be seen in Figure J.5.

The correction filter as designed and displayed in Figure J.4 was then applied,

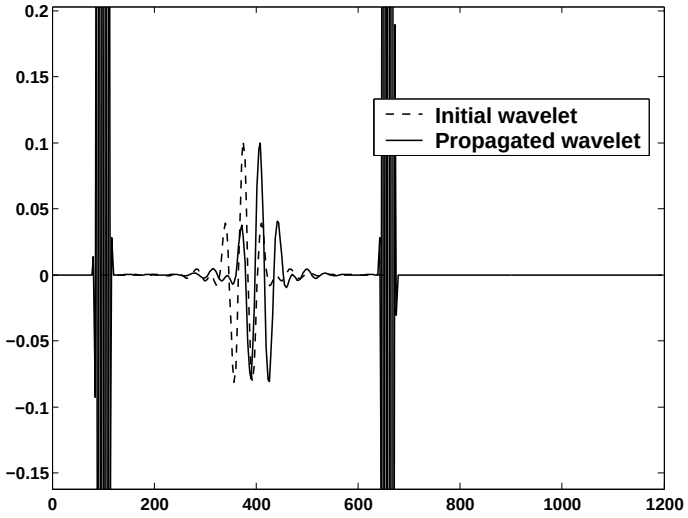

Figure J.5: Wave propagation for a general unstable case, uncorrected for 6 steps. The unstable zones appear at the ends of the defined wavelet, as in Figure 2.17

and the model was propagated for 100 steps and displayed in Figure J.6. The result is stable, although there is some distortion of the wavelet.

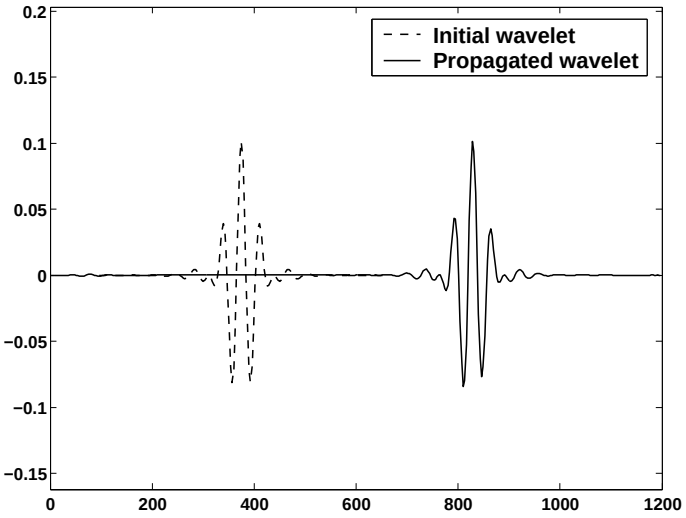

Figure J.6: Wave propagation for a general unstable case, corrected with the filter given in Figure J.4. The parameters are: $v = 1500$ m/sec, $\Delta x = 3$m, and $\Delta t = .003$ secs., and the wave is propagated for 100 steps.

Appendix K

Formulae derivations for uncorrected time stepping

In chapter 2 a formula was derived which gave an implicit definition of a wavenumber dependent velocity. This is the velocity with which an uncorrected time-stepping algorithm would propagate a wave component of that wavenumber. An explicit definition of this velocity is derived here, although there is minimal insight to be had from it, and it is not likely to be useful to many modellers.

The implicit formula is 2.21, repeated here for reference,

$$v(k) = v\frac{sinc(\frac{k\Delta x}{2})}{sinc(\frac{kv(k)\Delta t}{2})}. \tag{K.1}$$

The sinc functions may be expanded to obtain

$$v(k) = v\frac{sin(k\frac{\Delta x}{2})}{k\frac{\Delta x}{2}}\frac{kv(k)\frac{\Delta t}{2}}{sin(kv(k)\frac{\Delta t}{2})}, \tag{K.2}$$

or

$$sin\Big(kv(k)\frac{\Delta t}{2}\Big) = v\frac{\Delta t}{\Delta x}sin\Big(k\frac{\Delta x}{2}\Big). \tag{K.3}$$

Then

$$kv(k)\frac{\Delta t}{2} = \arcsin\left(v\frac{\Delta t}{\Delta x}sin\Big(k\frac{\Delta x}{2}\Big)\right), \tag{K.4}$$

and

$$v(k) = \frac{2}{k\Delta t}\arcsin\left(v\frac{\Delta t}{\Delta x}sin\Big(k\frac{\Delta x}{2}\Big)\right). \tag{K.5}$$

A second equation which appears when the uncorrected time-stepping algorithm is used, is the approximate velocity with which a wavelet appears to travel. This is known as the group velocity, and is given by the formula $v_g = d\omega/dk$. If the phase velocity is given by the implicit equation 2.21, or K.1, the group velocity may be derived from it. First assume that the wave frequency is dependent on k, given by the formula

$$\omega(k) = kv(k), \tag{K.6}$$

then $v(k)$ is defined by the formula

$$v(k) = v\frac{sinc(\frac{k\Delta x}{2})}{sinc(\frac{\omega(k)\Delta t}{2})}, \tag{K.7}$$

which has $\omega(k)$ in the place of $kv(k)$. Then

$$\omega(k)sinc\Big(\frac{\omega(k)\Delta t}{2}\Big) = kvsinc\Big(\frac{k\Delta x}{2}\Big), \tag{K.8}$$

and

$$\omega(k)\sin\Big(\frac{\omega(k)\Delta t}{2}\Big)\frac{2}{\omega(k)\Delta t} = kv\sin\Big(\frac{k\Delta x}{2}\Big)\frac{2}{k\Delta x}, \tag{K.9}$$

and

$$\sin\Big(\frac{\omega(k)\Delta t}{2}\Big)\frac{1}{\Delta t} = v\sin\Big(\frac{k\Delta x}{2}\Big)\frac{1}{\Delta x}. \tag{K.10}$$

Then, after taking the derivative,

$$\cos\Big(\frac{\omega(k)\Delta t}{2}\Big)\frac{\Delta t}{2\Delta t}d\omega(k) = v\cos\Big(\frac{k\Delta x}{2}\Big)\frac{\Delta x}{2\Delta x}dk, \tag{K.11}$$

and

$$v_g = \frac{d\omega(k)}{dk} = v\frac{cos(k\frac{\Delta x}{2})}{cos(\omega(k)\frac{\Delta t}{2})}. \tag{K.12}$$

This is the formula used in Figures 2.8 and 2.10.